DEVELOPMENT OF MICROELECTRONICS SOLDER JOINT INSPECTION SYSTEM: MODAL ANALYSIS, FINITE ELEMENT MODELING, AND ULTRASOUND SIGNAL PROCESSING

A Dissertation
Presented to
The Academic Faculty

By

Lizheng Zhang

In Partial Fulfillment
Of the Requirements for the Degree
Doctor of Philosophy in the
School of Mechanical Engineering

Georgia Institute of Technology
August 2006

DEVELOPMENT OF MICROELECTRONICS SOLDER JOINT INSPECTION SYSTEM: MODAL ANALYSIS, FINITE ELEMENT MODELING, AND ULTRASOUND SIGNAL PROCESSING

Approved by:

Dr. I. Charles Ume, Advisor
School of Mechanical Engineering
Georgia Institute of Technology

Dr. Suresh Sitaraman
School of Mechanical Engineering
Georgia Institute of Technology

Dr. Wayne Book
School of Mechanical Engineering
Georgia Institute of Technology

Dr. Kwok-Leung Tsui
School of Industrial and Systems Engineering
Georgia Institute of Technology

Dr. Jennifer E. Michaels
School of Electrical and Computer Engineering
Georgia Institute of Technology

Dr. Deepak Goyal
Assembly Materials Technology Labs
Intel Corporation

Date Approved: May 15, 2006

ACKNOWLEDGEMENTS

I am deeply grateful for the many people who have helped me with this work.

I would like to especially thank my advisor, Dr. I. Charles Ume, for his numerous guidance and support through the years.

I would like to thank my thesis reading committee: Drs. Wayne Book, Deepak Goyal, Jennifer Michaels, Suresh Sitaraman, and Kwok-Leung Tsui, for their expertise and valuable suggestions.

I would like to acknowledge the financial and technical supporters of this research: Nationals Science Foundation, Siemens AG, Visteon Corporation and Department of Energy.

Some of the experimental work would not be possible without the access to the Packaging Research Center lab facilities. I would like to thank Mr. Dean Sutter for his support during the thermal cycling experiments.

I would also like to thank my colleagues for their assistance and friendships along the way: Mr. Turner Howard, Dr. Dathan Erdahl, Dr. Reinhard Powell, Dr. Bao Mi, Dr. Akio Kita, Dr. Hai Ding, Mr. Wei Tan, Mr. Jin Yang and Mr. Matt Rogge.

TABLE OF CONTENTS

LIST OF TABLES

LIST OF FIGURES

SUMMARY

The attachment of electronic components to printed wiring boards has been accomplished primarily by solder joining technologies over the past few decades. Recently, new surface mount technology (SMT) designs based on ball and column grid arrays located underneath the component are gaining more popularity. This technology maximizes the input/output-to-component size ratio without excessive use of board acreage. Other soldered interconnection technologies focus on direct chip attachment (DCA), for example, flip-chip on board (FCOB) assemblies in which solder bumps located on the chip are directly mounted to the board. These various types of solder joining technologies provide for durable, long-lasting, and inexpensive methods of mass or isolated interconnect production.

Inspection of solder joints has been a crucial process in the electronics manufacturing industry to reduce manufacturing cost, improve yield, and ensure product quality and reliability. Traditionally, solder joint inspection has been performed manually and/or indirectly via electrical testing. Both methods are either subject to human error or are very inefficient. Currently available solder joint inspection technologies fall into one of the four categories: 1) visual or optical inspection, 2) X-ray inspection, 3) thermal inspection, and 4) acoustic inspection. While many of these techniques and systems are suited for specific inspection tasks, they do not necessarily encompass all the capabilities needed for evaluating the quality of the overall assembly. The present inspection techniques have a long way to go to meet industry requirements and the advent of hidden solder joints as a popular interconnection technology has brought new challenges. New

inspection techniques are urgently needed to fill in the gap between available inspection capabilities and industry requirement of low-cost, fast-speed, and highly reliable inspection systems.

The laser ultrasound inspection system under development aims to provide a solution that can overcome some of the limitations of current inspection techniques. Specifically, the fully developed system will be an automated system developed to meet the requirement of electronic manufacturing industry and is capable of inspecting hidden solder joints with a multitude of defect types, including but not limited to: missing solder bumps, misaligned IC chips, open solder joints, solder joint cracks, and the other defect types that are difficult or impossible to evaluate using present techniques. This research project is based on laser ultrasound and interferometric techniques. A pulsed laser generates ultrasound on the chip's surface and the whole chip is excited into structural vibration. An interferometer is used to measure the vibration displacement of the chip's surface at several points, and solder joints with different qualities cause different vibration responses. By analyzing the surface vibration responses, defects in solder joints may be detected and/or classified.

Previous work in this area has indicated the potential of the system to find defects in hidden solder joints of a flip chip assembly. However, there are still issues that need to be addressed before the system is ready to be used in an industrial environment. This dissertation focuses on addressing some of these existing issues in order to improve inspection efficiency. The research work consists of the following: 1) the inspection system was integrated and automated, and the system's throughput and repeatability were improved. Measurement system analyses including stability study and gage repeatability

and reproducibility study were performed to characterize the measurement capability of the system. 2) New signal processing algorithms were developed new to ensure fast and accurate interpretation of vibration signals. These include time domain correlation coefficient analysis method, Auto-Comparison method and frequency domain spectral estimation algorithms. 3) A finite element modal model was developed to explain and predict a flip chip package assembly's modal behavior and vibration response under laser pulse excitation, and was experimentally validated. This includes: a) finite element modal analysis was performed to obtain mode frequencies and mode shapes of a given package structure and b) specific changes in mode frequency, mode shape and vibration response in a defective package model were simulated and identified. 4) Experiments on experiments on different package formats and defect types were conducted to extend the system's application scope. This includes flip chip packages with open solder joints, flip chip packages with solder joint fatigue cracks and wafer-level CSP packages with missing bumps. Apart from these artificially created defects, a batch of flip chip assemblies with actual production defect(s) of unknown types were evaluated as well.

This dissertation work has led to a laser ultrasound solder joint inspection system prototype with faster speed, better precision, and improved sensitivity to defects that are prevalent and hard to detect. Finite element modeling has given a better understanding of the laser ultrasound induced vibration in electronic packages and how it can be exploited for solder joint defect detection. The signal processing algorithms enabled the fast and accurate interpretation of the vibration data and established the relationship between vibration response and solder joint defects. Finally, the study of solder joint cracks demonstrated the system's unique defect inspection capability.

CHAPTER 1

INTRODUCTION

The attachment of electronic components to printed wiring boards (PWBs) has been accomplished primarily by solder joining technologies over the past few decades. Electronic assembly designs have incorporated various types of technology configurations to form mechanical, electrical, and thermal interconnections. These configurations have developed from through-hole technologies that incorporate, single-sided, double-sided, and plated-through-hole (PTH) architectures, to surface mount technology (SMT) design, which includes standard, fine- and ultrafine-pitch devices for leaded and leadless component mounting. Recently, new SMT designs based on ball and column grid arrays, located under the component, have received wide interest. This technology maximizes the input/output-to-component size ratio without excessive use of board acreage. Other soldered interconnection technologies focus on direct chip attachment, for example, flip-chip applications. With this type of interconnection, solder bumps located on the chip are directly mounted to the board. These various types of solder joining technologies provide for durable, long-lasting, and inexpensive methods of mass or isolated interconnect production.

Depending on the operational environment, electronic assemblies may be in use for months or years and may experience extensive power and thermal cycling, vibration and other mechanical degradation mechanisms, and exposure to hostile environments. The failure of the soldered interconnections is not only directly dependent on the environmental conditions experienced, but is also inherently associated with the prior

manufacturing, rework, and repair history (Martin, P., 1999). This history includes joint design and geometry, fabrication techniques and parameters, thermal history, solder type and chemistry, and conductive circuitry and lead material type and condition. Inspection of solder joints has been a crucial process in the electronics manufacturing industry to reduce manufacturing cost, improve yield, and ensure product quality and reliability.

Traditionally, solder joint inspection has been performed manually and/or indirectly via electrical testing. Manual inspection is subject to human error and is very inefficient. Electrical testing consists of two primary methods: functional and in-circuit testing. Functional testing is characterized by electrically stimulating the entire assembly through an edge connector. The subsequent response is a pass/fail performance evaluation of the whole assembly, or at best, one area on the assembly. It normally can not trace the defect(s) down to a specific component. In contrast to functional testing, in-circuit testing tests the performance of each component and not the entire assembly by probing on different combinations of pre-designed test pads on the surface of the PWB. The series of probes are mounted in a bed-of-nails fixture and can establish contact with one or two sides of the assembly. The test fixtures have to be customized for each product design and are costly to design and manufacture. Developing such fixtures for fine- and ultrafine-pitch components may be prohibitive. The test pad also takes up a lot of board acreage which negates the purpose of miniaturization. Electrical testing is incapable of detecting intermittent defects since it is not inspecting the solder joint from a structural viewpoint. Some defective solder joints may pass the electrical testing but cause failures in the field.

Many techniques have been developed to inspect the solder joints structurally. Most of them fall into one of the four categories: 1) visual or optical inspection, 2) X-ray inspection, 3) thermal inspection, and 4) acoustic inspection. Among these techniques, some are well established and have been commercially available for practical use while others are still in early research stage. While many of these techniques and systems are suited for specific inspection tasks, they do not necessarily encompass all the capabilities needed for evaluating the quality of the overall assembly. The present inspection techniques have a long way to go to meet industry requirements and the advent of hidden solder joints as a popular interconnection technology has brought a new challenge. New inspection techniques are urgently needed to fill the gap between available inspection capabilities and industry requirements of low-cost, fast-speed, and highly reliable inspection systems.

Survey of Solder Joint Non-Destructive Inspection Methods

The following sections are a brief survey of the four major categories of inspection techniques. Both commercially available inspection systems and inspection methods still in the research stage are reviewed.

Visual Inspection

Visual inspection is the most widely used non-destructive technique for the examination of solder joints. Dedicated PCB visual inspection systems are already commonly used in manufacturing environments. Both 2-D systems and 3-D systems are available. For this method, inspection is limited to external surfaces or exposed internal surfaces of a solder joint.

A standard 2-dimensional inspections system includes an illumination source to light up the object, a camera to record the reflected light from the object, and an image processor that produces a recognizable image. Subsequently, the image can either be compared with a previously recorded good image to find the difference, or be interpreted using image processing and pattern recognition techniques.

Tiered illumination sources of two different colors as shown in Figure 1-1 has been used to generate color contours on the solder joint for detection and classification of defects including no solder, insufficient or excess solder, poor wetting of components leads or solder pad, and faults due to improper insertion of component leads (Capson, D.W. et al, 1988).

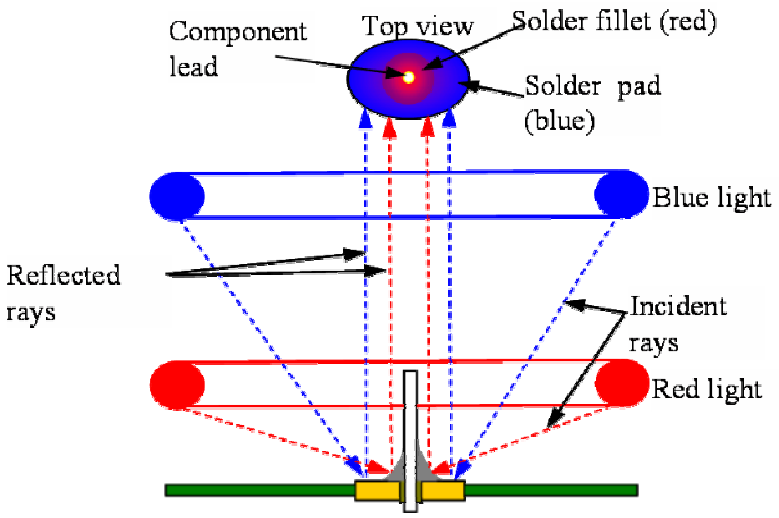

Figure 1-1: Color ring generation for a good solder joint

Another approach used a structure light to inspect the quality of wave soldered joints. This method projects a narrow intense beam of light onto several successive

positions along a solder joint. The light stripes were deformed upon intersection with the solder joint and this information was used to infer three dimensional structures. The solder joint was then identified as belonging to one of the five classes based on this information (Nakagawa, Y. et al, 1985). The method is computationally fast. It is also immune to the high gloss of the solder joints and insensitive to ambient lighting conditions. Its overall speed is limited by the required mechanical positioning of the solder joints beneath the light beam.

Three-dimensional machine vision using laser triangulation has also been used in solder joint inspection. Laser triangulation shines a laser beam onto the sample's surface, and the reflected beam is collected by photodetectors (Khazan, A.D., 1994). The reflected beam will move relative to the sample's height as the beam scans across the sample's surface. Figure 1-2 show a typical configuration of laser triangulation. Using geometric triangulation, the system can calculate the contour of the solder joint from the displacement of the reflected beam. Many commercial Automated Optical Inspection (AOI) systems have incorporated laser triangulation to realize 3-D inspection.

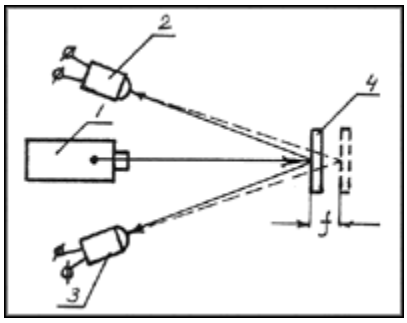

Figure 1-2: Laser triangulation measuring system, f = displacement, 1 = laser light source, 2 and 3 = light sensors, 4 = surface

Interference holography has also been considered for solder joint inspection. Interference holography is an extension of holography. Two holograms of the object are superimposed and recorded on the same film. The object is stressed mechanically or thermally during the second exposure of the object so that the hologram differs slightly around the stressed areas. During reconstruction, the two holograms will interfere and the interference fringes disclose the lines of stress. Discontinuities in the fringes indicate the defects (Jing, H. et al, 1986).

As hidden solder joints deny the access of light beams, visual inspection becomes almost infeasible. Industrial endoscopy has been tried to inspect solder joints in area array packages but can only provide information for the peripheral columns.

X-Ray Inspection

Commercial X-ray solder joint inspection systems are gaining more and more attention. There are two methods of X-ray inspection, radiography and laminography. X-rays are produced by bombarding a target (usually Tungsten) with electrons. X-ray emission is caused by the sudden deceleration of the electrons as they collide with the target. X-rays have a wavelength of about 100 angstroms. This short wavelength allows them to penetrate most materials. A typical system will have an X-ray source to produce a focused spot of radiation, an X-ray conversion screen to collect the penetrated radiation, and a video camera to convert the photons on the screen to a digital form.

The application of X-ray radiography to solder joint inspection is a natural development as it has the required resolution and can see through the whole solder joint, not just its surface. Most commercially available 2-D X-ray inspection systems use radiography. One problem with radiography is that any point in the image is affected by

all material boundaries between the X-ray source and detector. Therefore, it is very difficult to interpret the images of multilayered or double-sided boards. Another disadvantage is that it is difficult to detect cracks. The cracks must be properly positioned with the joint relative to the radiation to promote sufficient contrast (Martin, P., 1999).

X-ray laminography circumvents this problem by focusing the X-ray beam on one plane at a time and slicing the board horizontally. This is achieved by continuously rotating the source and detector about the point under observation. As the system moves, the rest of the PCB becomes out of focus and blurred into a constant gray level, but the point under examination is relatively stationary and stays in focus. This spot can then be scanned across the PCB and also its depth in the PCB can be altered giving a 3-D scan of the board. Figure 1-3 shows the principle of X-ray laminography. This inspection technique is extremely effective and will detect almost all solder joint defects. However, the equipment and operation cost of this kind of system is prohibitive.

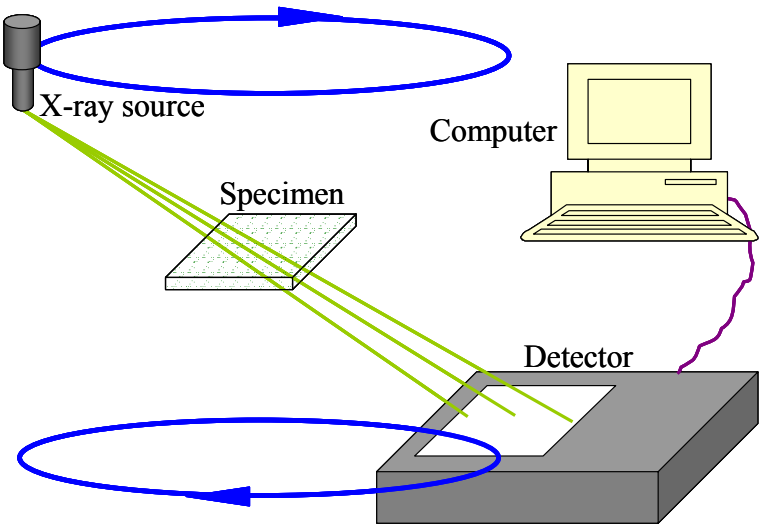

Figure 1-3: Laminography with orbiting X-ray and detector

Thermal Inspection

Thermal inspection operates on the premise that differing materials exhibit unique thermal properties and, as a result, absorb and release heat energy differently. Likewise, a material of a given volume that is strongly attached to its substrate will demonstrate an accelerated cooling rate over a similar amount of the same material that has not been firmly bonded to its respective substrate. Therefore, the heat capacity of a defective solder joint will differ from that of a good joint. Measurement of heat capacity can be done in two ways: thermal imaging and thermal profile inspection.

In a thermal imaging inspection, the entire PCB assembly is exposed to an IR heat source, then, the thermal energy released during cooling is monitored using an IR camera. The recorded video image represents the thermal energy as variations in grayscale data. The images are compared to previously stored images to assess variations, which then can be related to specific defects. Another approach is to power up the whole assembly and wait until the components reach operational temperature, then, a thermograph is generated with an IR camera. Again, the thermograph is compared to a previously obtained thermograph to analyze defects (Pearson, K.V., 1986).

The thermal profile inspection technology is different from thermal imaging in that it takes values for the solder joint's temperature over time instead of an instantaneous thermal map of the whole assembly. The temperature of a solder joint will rise then cool down when exposed to a short laser pulse. The thermal signature of the joint will contain information on the joint's structure (Traub, A. C., 1988). The typical operation starts with positioning of the solder joint under the confocal lens. A continuous-wave Nd-YAG laser then emits a pulse of laser energy at about 12W. The pulse duration ranges from 20 msec

to 100 msec. The solder joint's temperature is monitored by a photo-detector sensitive to IR radiation. The thermal signatures are then compared with ideal signatures from previously stored data, and any differences in thermal mass or surface absorption can be related to specific defects. This type of system is very sensitive to surface effects, but defects inside the solder joint are hard to find.

Acoustic Inspection

Sound waves are essentially mechanical vibrations of the medium in which they travel (Seto, W. W., 1971). Ultrasonic waves are sound waves whose frequency are above 20 kHz and are used for non-destructive evaluation in many areas. When an ultrasonic wave travels through a medium, its attenuation and propagation speed are dependent on the medium's structure. Similar to light waves, refraction and reflection can also occur for ultrasonic waves. Ultrasonic waves are able to penetrate optically opaque surfaces, and the depth of penetration decreases with increasing frequency.

Scanning acoustic microscopy (SAM) uses an ultrasound point source to scan across the sample surface. The source of ultrasound is usually generated by a piezoelectric transducer and then focused using a sapphire lens. The ultrasound will propagate towards the sample surface and part of the energy will be reflected each time it encounters a boundary between two materials or a structural defect. The same transducer then records the reflected pulses and converts it to electrical signals. The processor then constructs an image of the sample from the delays between each received pulse. Moving the sample towards and away from the transducer will cause the path lengths of the defects' waves and the expected waves to change at different rates. The resulting destructive/constructive interference at the sensor will give contrast to the image. The

SAM system's resolution is a function of ultrasound frequency. Higher frequencies can give clearer images but the penetration depth into the sample is lower so subsurface defects may be missed. A big drawback with SAM is its speed. Construction of a detailed image requires that the sample be scanned with a high frequency pulse, which makes it unacceptable for on-line applications.

An extension of SAM is Scanning Laser Acoustic Microscopy (SLAM). SLAM differs from SAM in that the ultrasound is detected after passing through the PCB and the disturbances produced by the ultrasound on a polished surface are measured, instead of the reflected waves. SLAM uses a transducer near the PCB to produce ultrasound that travels through the board, being attenuated by material boundaries or defects on the way. The emerging ultrasound on the other side continues traveling and strikes a thin polished surface that is positioned near the PCB. The deformations on the surface are proportional to the intensity of the waves. These waves are attenuated according to the structure of the PCB at that point. Laser light is used to scan the surface and its reflections monitored. From this scan, an image of the attenuated ultrasound can be made showing the PCB's structure. The use of a laser to scan instead of the transducer greatly decreases the time required to form the image. However, SLAM can only be used with ceramic PCBs because multilayer materials like FR4 have so many boundaries that the ultrasound becomes scattered on its way through the board. This is a very serious drawback as most PCBs are made from FR4.

The major drawback with SAM and SLAM is the requirement of a coupling medium. Without the medium (usually deionized water), the incident ultrasonic waves would be mostly reflected back at the surface. Also, the acoustic attenuation of air is very

large so most of the energy would be lost. Besides the possible interaction between the PCB and the water, there is a problem with air bubbles trapped in the assembly giving spurious results.

Another group of acoustic inspection techniques involves photothermoelastic vibration. Photothermal vibration uses laser energy to induce vibrations in the solder joint. Properly bonded solder joints have smaller vibration amplitude whereas a lead with a poor joint will be free to vibrate and the amplitude will be greater. All these techniques use a laser to create thermal stresses/strains in the joint at some frequency and then an interferometer to measure the joints' response.

Kazuhiro et. al. (1988) proposed a solder joint inspection system that uses the method outlined above. The authors modulated a laser diode and directed the resultant beam onto the knee of a gull-wing lead. The laser diode was modulated at a frequency of 30 Hz and created thermal waves of the same frequency in the joint's lead. The probing beam was generated by a Helium-Neon laser. It was directed at a point nearer the end of the lead. The beam reflected off the joint was then monitored by a photodetector. As the lead vibrates, the speckle pattern at the photodetector changes so the lead's movement can be monitored from the photodetector's output.

Jean-Pierre Monchalin (1986a) reported on a test system that brings together the idea of laser generation and detection of ultrasound. This system with modifications could in principle be used for the verification of solder joints. The ultrasound is produced by a Q-switched Nd-YAG laser. The beam is directed onto the sample via a convex telephoto lens. This provides the thermoacoustic waves which have the same frequency as the modulated laser. The second laser, a low power He-Ne single mode laser operating

at about 0.5 mW, provides the measuring beam. Part of this beam is taken and fed through the confocal Fabry-Perot as a reference to make sure the mirrors do not drift too far during operation. Most of the energy is however directed to the surface along the same path as the Nd-YAG laser. Because the beams are parallel, the distance between the system and the sample can vary without the need for realignment of mirrors and lenses. Scattered light from the sample's surface is then collected by the same lens and transmitted back to the Fabry-Perot device. The steering of these three beams through the system without their interference is achieved by keeping them polarized at different angles. To do this, quarter wave rotators are used. This allows two beams to share a path at the same time or when needed, to take separate paths through the use of polarizing beam splitters. As described earlier, the velocity of the surface will be indicated by the output of the Fabry-Perot. For maximum sensitivity, the laser frequency must be set on one of the interferometer's response peaks. A photodiode will monitor the output and relay its electrical signal to a scope. Although the experimental results are good, and show that the system can detect surface vibrations, a lot of work is needed to bring the system to the production floor.

A variation on the use of the velocity interferometer was found by Hewlett-Packard (Kelly C. A., 1989). The researchers have developed a solder joint inspection system that finds the joint's resonant frequency. From this the researchers can tell whether surface mount joints are bonded to the pad or not. Properly soldered joints will have some resonant frequency which is dependent on the type of lead, device package and substrate. Hewlett-Packard used finite element models to find the resonant frequencies of solder joints in packages such as SOIC, Fine Pitch PQFP, etc. The

vibrations were induced by directing an air jet at the joint. The jet is a source of white noise which will set up vibrations in the joint at its resonant frequency. The vibrations in the joint are measured using an interferometer. The interferometer used by Hewlett-Packard works on a different principle to the Fabry-Perot. It takes a laser beam and, using a beam-splitter, splits it into two. One of these beams is frequency shifted to have an extra 80 MHz. This is the reference beam. It goes directly to a PIN detector. The other beam is reflected off the joint's surface and then to the PIN detector. The frequency difference can then be read as a function of the output. The results show that the joints do in fact have peaks of vibration amplitude at certain frequencies. There may be more than one peak through the frequency sweep or the peak may not near where it is expected. These results will give information about the joint's structure. To date, only soldered and non-soldered joints can be discriminated, but work is still ongoing.

In summary, although there are many inspection techniques available for solder joint inspection, each targets on certain defect types, none of them suits the needs of all classes of electronics manufacturing. The electronics manufacturing industry is not satisfied with present inspection techniques mostly because of their reliability, i.e., falsely accepted or rejected joints can cause unnecessary rework or allow a faulty assembly to pass inspection. For hidden solder joints which are becoming more and more popular, only a few present techniques have some limited capacity to inspect them. For these reasons, research into new techniques continues.

Laser Ultrasound Inspection System (LUIS)

The laser ultrasound inspection system under development at Dr. Ume's research lab aims to provide a solution that can overcome some of the limitations of current inspection techniques. Specifically, the fully developed system will be an automated system that is capable of inspecting hidden solder joints with multiple defect types, including but not limited to: missing solder bumps, misaligned IC chips, open solder joints, solder joint cracks, and the other defect types that are difficult or impossible to evaluate using present techniques, to meet the requirement of electronic manufacturing industry. This approach offers an innovative technology with the development of a novel automated in-line inspection system for a wide variety of electronic assemblies, including flip chip or direct chip attachment (DCA), ball grid array (BGA), chip scale packaging (CSP) or wafer-level CSP, stacked packages and die, chip capacitors and resistors, optoelectronics and MEMS components.

The global market for electronic assembly exceeds $20 billion per year. The existing alternatives for post-assembly inspection, primarily in-circuit test (ICT) and automated X-ray inspection (AXI), have equipment sales on the order of $500 million per year, representing a significant cost element in the production process even before adding labor and overhead to the cost-per-inspection. In addition to cost savings, Laser Ultrasound Inspection System (LUIS) offers the potential for rapid optimization of test programs resulting in significant decrease in new product introduction (NPI) and ramp-up cycle times (e.g. elimination of custom in-circuit test fixtures). Widespread adoption of the technology could result in product redesign to eliminate substrate test points, with significant reduction in product size and cost. Finally, LUIS can be an enabling

technology for convergent packaging technologies combining the traditionally separate activities of integrated circuit packaging and printed circuit assembly.

This research project is based on laser ultrasound and interferometric techniques (Monchalin, J. P., 1989). Figure 1-4 shows the operating principle of the laser ultrasound inspection system. A pulsed laser generates ultrasound on the chip's surface and the whole chip is excited into structural vibration. An interferometer is used to measure the vibration displacement of the chip's surface at several points, and solder joints with different qualities cause different vibration responses (Lau, J. et al, 1989). By analyzing the surface vibration responses, defects in solder joints may be detected and/or classified.

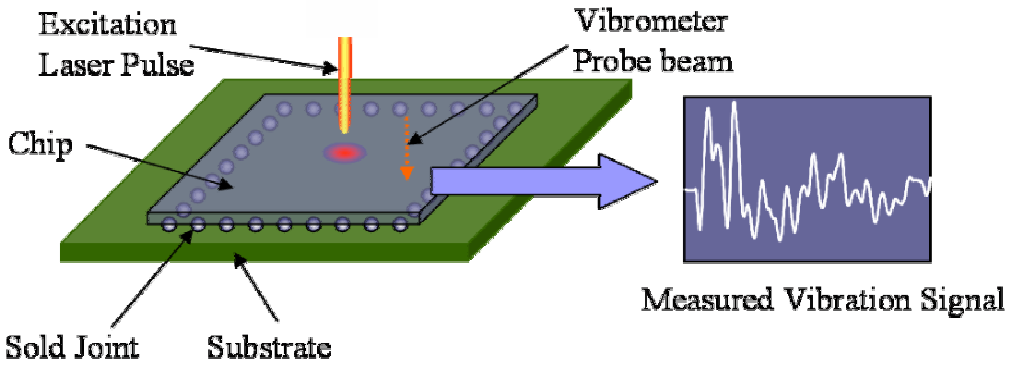

Figure 1-4: Operating principle of the laser ultrasound inspection system

Previous work in this area has shown the potential of the system to find defects in hidden solder joints of a flip chip assembly. However, there are still issues that need to be addressed before the system is feasible for industrial use. This dissertation work focused on addressing some of these existing issues to improve inspection efficiency. The approaches are to: 1) develop a finite element model to explain and predict a package assembly's modal behavior and vibration response under laser pulse excitation, 2)

develop new signal processing algorithms to ensure accurate and fast interpretation of vibration signals, 3) optimize system performance by defining optimum testing parameters through design of experiments (DOE), measurement system analysis (MSA), and gage repeatability and reproducibility (GR&R) studies, and 4) study different package formats and defect types to extend the system's application scope.

In the following chapter, the background information necessary to understand how this laser-induced vibration technique is used to identify solder joint defects is presented. In particular, the laser ultrasound generation and detection, measurement system analysis, signal processing and experimental and finite element modal analysis are discussed. Chapter 3 focuses on the integration and automation of the inspection system, as well as the measurement capability study that characterize the system's stability and repeatability. Chapter 4 presents the different signal analysis methods in both time domain and frequency domain that are developed to provide accurate interpretation of the measurement data and to establish the relationship to solder joint defects. Chapter 5 covers the finite element modal analysis of flip chip assemblies and experimental validation. A finite element modal model is constructed and used to simulate different solder joint defects. Chapter 6 presents the inspection of solder joint fatigue cracks using the system. Solder joint cracks are artificially induced with temperature cycling and the vibration responses are studied using the developed time-domain and frequency-domain signal processing methods. Chapter 7 concludes the contribution and impact of this research work, and recommendations for future work in this area occupy Chapter 8.

CHAPTER 2

LITERATURE AND BACKGROUND

Development of the LUIS system entails multidisciplinary expertise including microelectronics packaging, laser optics, laser ultrasound generation and detection, mechatronics, vibration analysis, digital signal processing, finite element analysis, statistical process control and design of experiments, etc. The integration of these various technologies will lead to the successful development of an inspection system that meets the overall research goal.

Flip Chip and Advanced Electronic Packaging Technologies

Flip chip microelectronic assembly is the direct electrical connection of face-down (i.e., "flipped", see Figure 2-1) electronic components onto substrates, circuit boards, or carriers, by means of conductive bumps on the chip bond pads. In contrast, wire bonding, the older technology which flip chip is replacing, uses face-up chips with a wire connection to each pad. Flip chip is also called Direct Chip Attach (DCA), a more descriptive term, since the chip is directly attached to the substrate, board, or carrier by the conductive bumps. There are three stages in manufacturing flip chip assemblies: bumping the die or wafer, attaching the bumped die to the board or substrate, and, in most cases, filling the remaining space under the die with an electrically non-conductive material i.e. underfill. Underfill is needed to counteract the stresses induced by coefficients of thermal expansion (CTE) mismatch between the die (~2.5ppm/°C) and the

organic circuit board (~18ppm/°C). The underfill also resists moisture absorption and provides physical protection for the chip's active face.

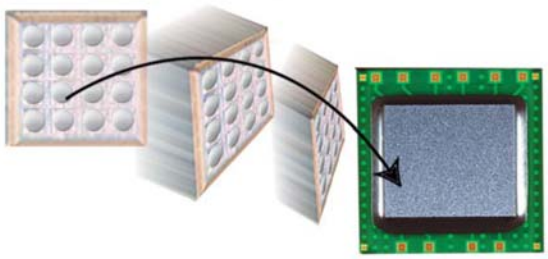

Figure 2-1: Flip chip on board assembly

IBM introduced flip chip interconnection in the early sixties for their mainframe computers, and has continued to use flip chip since then. Delco Electronics developed flip chip technology for automotive applications in the seventies. Current worldwide flip chip consumption is over 3,000,000 units per year, with a projected annual growth rate of nearly 50% per year. More recently, applications have employed flip chips mounted on a variety of substrates, including glass, ceramic, and flexible materials. Flip chip technology is also a building block for many emerging electronic packages including but not limited to: ball grid arrays (BGAs), chip scale packages (CSP), stacked dies and stacked packages, and even MEMS devices. Many of these packages are constructed upon flip chip technology. For example, Figure 2-2 shows cross-sections of two types of BGA packages. One of them uses the older wire-bonding technology, while the other uses flip chip interconnection internally, also known as Flip Chip BGA

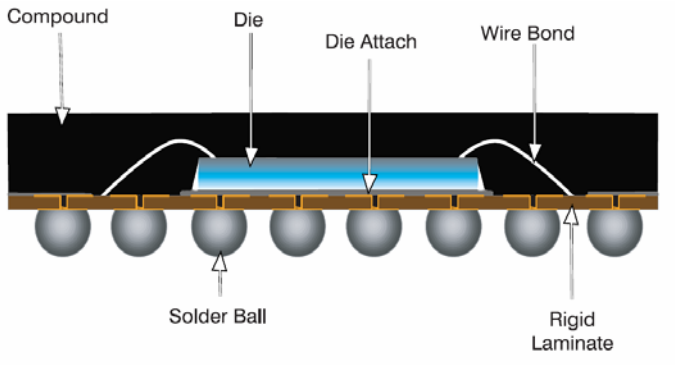

(a)

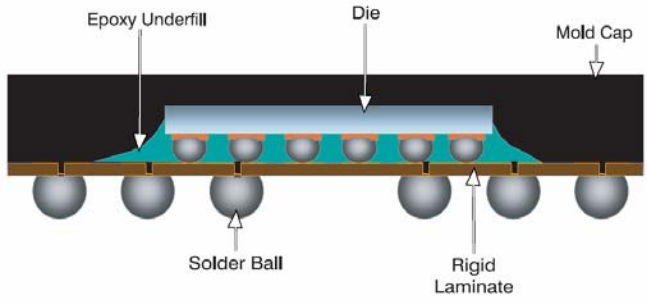

(b)

Figure 2-2: Cross sections of a) wire bond BGA, and b) flip chip BGA

The boom in flip chip packaging results both from flip chip's advantages in size, performance, flexibility, reliability, and cost over other packaging methods and from the widening availability of flip chip materials, equipment, and services. However, there are also drawbacks. Flip chip solder joints are hidden from direct access and difficult to inspect with many existing inspection systems, and underfilling requires additional process steps - after which rework becomes impossible. On the other hand, many recently developed advanced electronic packages also use solder bumps to realize the interconnection with the substrate. These solder joint connections are mostly in the area array format and hidden in between the substrate and the device as well. Similarly, they

are difficult or impossible to inspect with commercially available inspection equipments. Therefore, it is critical to have a reliable, fast, low cost and non-destructive means to inspect these hidden solder joints on-line or off-line so that package reliability is guaranteed. The proposed laser ultrasound inspection system could serve as an enabling technology to ensure the microelectronic world moves swiftly and effortlessly into the future.

Solder Joint Reliability Challenges in Electronics Manufacturing Industry

Profound changes in packaging technology driven by Moore's Law, a doubling of transistor density every 18-24 months, have led to decreasing die size, increasing transistor count (from five thousands to 42 millions), and increasing power density (W/cm^2) by 30 times (Blish, R. et al, 2003). These trends have driven packaging interconnect density more than six-fold in the last five years (Goyal, 2000). There has been an explosion of package technologies to satisfy the needs of the communications and emerging market segments. End products include personal digital assistants (PDAs), memory devices, optical devices, and micro-electromechanical systems (MEMS). This rapid development of applications has led to a large array of packages such as chip scale packages (CSP), system-on-a-chip (SoC), system-in-a-package (SiP), and stacked chip scale packages (SCSP) to serve this divergent marketplace (Dias, et al, 2004). Most of these packages have required first level interconnect technology to transition from peripheral wire bonding to area array bumping. At the same time, scaling demands are driving bump size and pitch to the limits of current technologies. As bump size decreases, the bump becomes less compliant because of the geometry, making it more susceptible to

thermal and mechanical driven failure modes such as fracture. Consequently, solder joint reliability has become one of the key challenges facing the electronics manufacturing industry. Meanwhile, the move to "lead (Pb) free" packaging adds new risks to solder joint interconnection. Higher processing and mounting temperatures increase thermal stresses. Ball and bump metallurgy changes will bring new reliability concerns as well.

Traditional methods such as X-ray and acoustic microscopy may yield only limited data when inspecting solder joints in advanced packages such as stacked dies and stacked packages. X-ray tomography holds some promise for deconvolving the several image layers to see the individual planes. Without this capability, the many overlapping layers would be impossible to resolve. Acoustic microscopy is problematic because the technique has limited penetration depth at the required resolution and because there are problems penetrating multiple interfaces. The currently available solder joint inspection techniques need a revolutionary change to meet these challenges.

Laser Ultrasound Generation and Detection

In order to obtain ultrasound of sufficient amplitude to be readily detected, most work in optical generation has been carried out into the use of high-power pulse lasers. Conventional ultrasonic generation by a pulsed laser usually lies between two extreme regimes. The two main regimes are [Scruby et al (1990), Davies et al (1993)]: a) the 'thermoelastic' regime (damage free but relatively inefficient source for normal incidence waves), and b) the 'ablation' regime (intense longitudinal waves generated at the expense of surface damage). These regimes provide different sources of ultrasound, with differing characteristics (Figure 2-3).

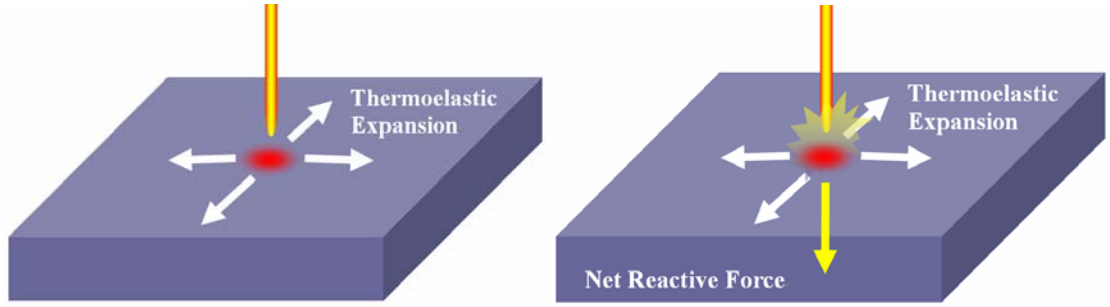

(a) (b)

Figure 2-3: Ultrasound generation in a) thermoelastic regime, and b) ablation regime

When the beam of a laser is directed onto a solid sample, the electromagnetic radiation interacts with electrons in the material close to the surface. Some of this incident radiation is absorbed by the sample thereby heating its surface whilst the remaining energy is reflected. Thermal conductivity distributes this heat through the sample causing temperature gradients which generate the stress and strain fields of the elastic waves by thermal expansion. The main temperature changes take place only within a few microns of the surface. This ultrasonic source can be approximated as a center of expansion with the principal stress components parallel to the surface as shown in Figure 2-3(a) and no perpendicular components. The amplitudes of the ultrasonic waves increase linearly with the applied power density.

Focusing the laser beam can cause such an increase of the power density at the surface that it will start vaporizing, and material to the depth of several micrometers will be vaporized, forming plasma. This removal of material produces a reactive stress predominantly normal to the surface as shown in Figure 2-3(b). In this regime, the generation of compression and surface waves is enhanced with increasing power density, but shear waves will reach a maximum near the onset of plasma and then decrease.

Since the proposed LUIS system has to be totally non-contact and non-destructive, ultrasound generation under this research will primarily be controlled to fall into the thermoelastic regime. Laser energy density will be controlled by adjusting the laser pulse power level and the projected spot size, to ensure no ablation occurs. However, it is possible that in some cases ultrasound signals generated in the thermoelastic regime are too weak to demonstrate an adequate signal to noise ratio (SNR). Several approaches can potentially address this problem without damaging the specimen under test. Yang, J. and Ume, C. (1994) used an array of fibers to spread the energy out to a larger area on the specimen, preventing the surface ablation while generating ultrasound strong enough for detection. Surface modifications such as evaporating liquid coatings and constraining layers can also lead to an enhancement of thermoelastic generation efficiency by the introduction of a normal force (Hutchins, 1988). Dixon et al. (1996) demonstrated that plasma can be used to generate ultrasound without the laser directly impinging on the sample surface. The plasma is generated by focusing a Transversely Excited Atmospheric (TEA) CO_2 laser onto a 'dummy' target. The plasma expands away from the dummy target and impacts on an experimental sample such that it generates ultrasound at the sample surface.

There are many ways to detect ultrasonic waves. Since the proposed research requires a non-contact method, optical detection methods are the best candidates. Coupling the advantages of both laser ultrasound generation and optical detection can lead to a powerful non-contact and non-destructive inspection system. The many optical detection techniques for ultrasound can be classified into non-interferometric and interferometric techniques. The former includes knife-edge technique, surface-grating

technique, technique based on reflectivity and technique based on a light filter. All these techniques give a filtering bandwidth that is fixed and determined by the medium (Monchalin, J. P., 1986b). Unlike the non-interferometric techniques, the interferometric techniques enable easy selection of the most suitable bandwidth. These techniques can be classified into three types: 1) optical heterodyning, 2) differential interferometry, and 3) velocity or time-delay interferometry. As far as sensitivity is concerned, these techniques have about the same theoretical sensitivity. The choice of a particular technique for a given application is therefore not a matter of sensitivity, but rather its light collection efficiency, immunity to vibration, and the sample surface conditions.

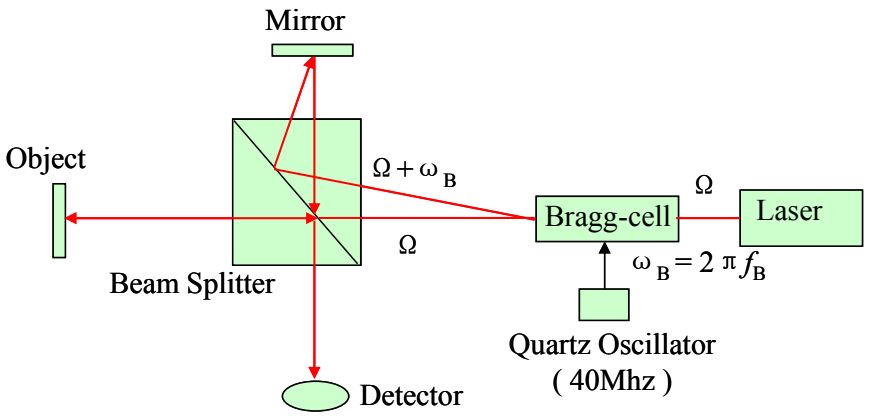

Figure 2-4: Heterodyne interferometer diagram

In this research, a heterodyne Michelson optic fiber interferometer will be used for ultrasound detection. The heterodyne interferometer is a two-beam interferometer with a reference arm and an object arm reflected from the object. The two beams to be mixed are of slightly different optical frequencies. Typically, this is obtained by passing a laser beam through an acousto-optical modulator (Bragg cell) as shown in Figure 2-4.

The frequency shifted beam (of frequency $\Omega + \omega B$) will be refracted at a different angle and serve as the reference arm. The unaltered beam (of frequency Ω) will be the object beam. Both beams pass through a beam-splitter and are collected by the optical detector. The heterodyne interferometer has a broad detection bandwidth and a good immunity to ambient vibrations. The optic fiber interferometer also adds flexibility in configuring the system.

Modal Analysis and Finite Element Modeling

Given a mechanical structure, there are certain frequencies at which the structure will undergo vibration of large amplitude by sustained time varying forces of matching frequencies. These are said to be the resonant, natural, or free vibration frequencies of that structure. It is also known that associated with each natural frequency there is a distinct characteristic or mode shape which the structure acquires as it vibrates. Experimental modal analysis, a method widely used in the study of structural dynamics, has always provided a major contribution to our efforts to understand and control the many vibration phenomena encountered in practice. A successful modal analysis entails a thorough integration of three components: a) the theoretical basis of vibration, b) accurate measurement of vibration, and c) realistic and detailed data analysis.

In this research, a broadband laser pulse is used for dynamic excitation of the chip before its vibration signature is analyzed. The short duration of laser pulse can be considered as an impulse excitation source so that the frequency response function (FRF) of the structure can be readily approximated from the Fast Fourier Transform (FFT) of the measured response. Since we are only interested in the out-of-plane vibration on the

chip's surface, and because the chip's length and width are much larger than its thickness, it can be simply modeled as a rectangular plate with pin supports.

While there are analytical solutions to this model (Timoshenko et al, 1959, Gorman, 1982, and Blevins, 1995), the development of high-speed computers has popularized the use of the Finite Element (FE) Method. In this approach, numerical methods have been used to obtain solutions which satisfy, as closely as possible, the plate governing differential equation and the prescribed boundary conditions. The FE method can be used to solve vibration problems with irregular system configurations and complicated boundary conditions. In our case, the distribution of solder balls is not always symmetric and the boundary condition is complicated. Therefore, the finite element method will be better suited for this problem.

The primary virtue of finite element analysis is the relative ease with which it can describe the small scale features and overall irregularities that make mathematical analysis so difficult. In the present context a finite element analysis of the vibration of a flip chip has several uses. One is to explain results obtained from experimental modal analysis. For example, generalization of the techniques would require knowing why some modes are more sensitive to the presence of defective solder bumps. Such knowledge is needed to anticipate the spatial resolution with which the chip's displacement is scanned. Similarly the availability of such models enables one to interrogate them prior to an actual test in order to ascertain where the laser pulse should be applied. This would enable one to be reasonably certain that the modes that are most sensitive to defects are strongly excited, and therefore give high signal-to-noise ratios, which enhance the accuracy of the modal identification. A different use of finite element analysis is to

enable one to consider a wide variety of situations. Doing this experimentally requires fabrication of many good and defective chips in order to assess the significance of the number and spatial position of bad solder bumps. In addition to the difficulty and expense of such fabrication, the vibration measurements entail a significant effort. The alternative is to calibrate a few finite element models relative to the corresponding actual system, thereby verifying that one has captured the essential physical feature. Other defective configurations can then be generated by suitable modifications of the solder bump representation. Vibrational analysis of each finite element model leads to a set of displacement-time histories. This data can be processed by the same modal analysis algorithms as those used for the actual responses. The net effect is to assure that the damage metrics that are derived correctly capture all possible defective configurations.

Measurement System Analysis

Measurement is a process of evaluating an unknown quantity and expressing it as a numerical quantity. It is therefore subject to all the laws of variation and statistical process control (SPC). Oftentimes, measurements are made with little regard for the quality of such measurements. Measurement system analysis (MSA) is the scientific and statistical analysis of variation (ANOVA) that is induced into the process of measurement. A measurement system consists of not only the measurement instrument, but also the person using the measuring instrument i.e. the appraiser, the environment under which the reading has been obtained, the methods used to setup and measure the parts, the tooling and fixture that locates and orients the object under measurement, and any software that performs intermediate calculations and outputs the result. The reading

obtained is thus influenced by each of these components and each component introduces a variation to the measurement process. Therefore, before embarking on using any new measurement systems for a characteristic which has not been previously measured on it, an MSA should be performed. MSA are critical to the success of every measurement and to ensure that future measurements will be representative of the characteristic being measured. MSA has been attempted and done in many quality initiatives in the past. It gained wider recognition when it was formally defined as one of the key requirements in the QS 9000 Quality Standard, and when it was recognized as an important technique in Six Sigma initiatives.

Measurement of surface vibration is such an essential part of the LUIS system being developed that all the information being used to evaluate a solder joint are extracted from the surface vibration signal. For this reason, the inspection system under development should also be considered as a piece of measurement equipment, and an MSA study of this system is necessary to prove its reliability and measurement capacity.

Digital Signal Processing

In the proposed LUIS system, the out-of-plane displacements detected by the interferometer are in the form of ultrasonic waves buried in white noise. Liu et al (2003) employed a number of signal processing techniques in both time-domain and frequency-domain to precondition, de-noise and extract useful information from the raw signals. In that work, a measured signal was compared to a reference signal directly in the time-domain using an “error ratio (ER)” method. The ER is essentially the differential energy

of the reference signal and the measured signal normalized by the reference signal energy, as represented by equation (1).

$$ER = \frac{\int [f(t) - r(t)]^2 \, dt}{\int [r(t)]^2 \, dt}, \qquad (1)$$

where f(t) is the measured signal, and r(t) is the reference signal.

The ER value appeared to be a relatively sensitive indicator of both the existence and even locations of solder joint defects in certain cases (Liu et al, 2003). Periodogram averaging was also used to analyze the signal power density distribution in the frequency domain. A frequency shift between the reference signal from a good sample and the signal measured from a defective sample was observed as well. These methods formed the basis of experimental data interpretation in this research, even though they have their own limitations.

As mentioned in the section entitled "Modal Analysis and Finite Element Modeling", the surface displacement signals generated under impulse excitation contains the modal information of the structure. The signal power will be concentrated at certain mode frequencies. Spectral estimation techniques can help obtain the mode frequencies from the raw data precisely. The goal of spectral estimation is to describe the distribution (over frequency) of the power contained in a signal, based on a finite set of data. The various spectral estimation methods can be categorized into nonparametric methods, parametric methods, and subspace methods.

Nonparametric methods are those in which the power spectral density (PSD) is estimated directly from the signal itself. Periodogram averaging is the simplest method in this category. An improved version of the periodogram is Welch's method (Welch, 1967). A more modern nonparametric technique is the multi-taper method (MTM). Parametric methods are those in which the PSD is estimated from a signal that is assumed to be the output of a linear system driven by white noise. Examples are the Yule-Walker autoregressive (AR) method and the Burg method. These methods estimate the PSD by first estimating the parameters (coefficients) of the linear system that hypothetically "generates" the signal. They tend to produce better results than classical nonparametric methods when the data length of the available signal is relatively short. Subspace methods, also known as high-resolution methods or super-resolution methods, generate frequency component estimates for a signal based on an eigenanalysis or eigendecomposition of the correlation matrix. Examples are the multiple signal classification (MUSIC) method or the eigenvector (EV) method. These methods are best suited for line spectra, that is, spectra of sinusoidal signals, and are effective in the detection of sinusoids buried in noise, especially when the signal to noise ratios are low. Selective and effective use of these methods will help to extract useful information from raw signals for defect identification.

CHAPTER 3

SYSTEM INTEGRATION AND AUTOMATION

Laser Ultrasound Inspection System (LUIS) Setup

The experimental setup, shown in Figure 3-1, consists of: (a) a pulsed Nd:YAG laser to generate the laser pulses, (b) a fiber optic beam delivery system to transmit the laser pulses onto the sample surface, (c) a laser Doppler vibrometer which detects the surface vibration from the sample, (d) an automated motion stage to translate the sample under test, (e) a manual stage on top of the automated motion stage to adjust the position of the laser excitation spot on the sample surface, (f) a vision sensor to locate the sample by capturing the fiducials on the sample board, and (g) a PC to coordinate the operations of these components and to acquire and process vibration signals.

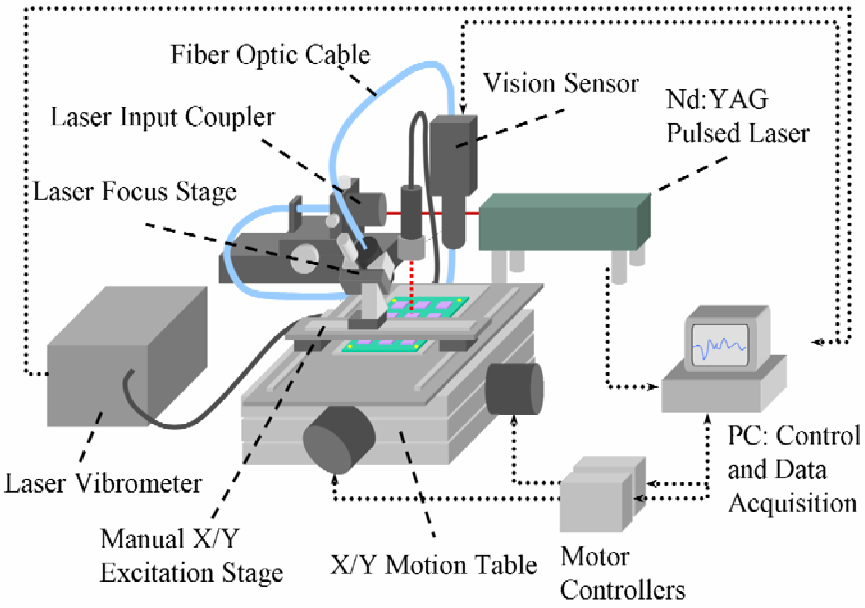

Figure 3-1: System configuration diagram of the laser ultrasound inspection system

Pulsed Nd:YAG Laser Module

A Polaris II model laser module from New Wave Research, shown in Figure 3-2 was used as the excitation source. The pulsed Nd:YAG laser generates short laser pulses with a duration of 4~5ns at the wavelength of 1064 nm. The laser has a variable repetition rate which can be adjusted from 1 to 20 Hz. The pulse energy is adjustable through a motorized optical attenuator and can be up to 45 mJ. The integral motorized variable attenuator used a half wave plate (HWP) and a polarizer to adjust the output energy. This feature allowed a continuous range of pulse energy to be supplied to a specimen while operating the laser at its optimal flash lamp voltage and Q-Switch delay settings, ensuring peak performance and maximum pulse-to-pulse stability. The laser module can also be easily configured to produce 532 nm (green) light with the installation of a second harmonic generator (SHG). The dual wavelength output (1064 nm NIR light vs. 532 nm green light with SHG) will help determine the best excitation conditions for various materials used in future experiments.

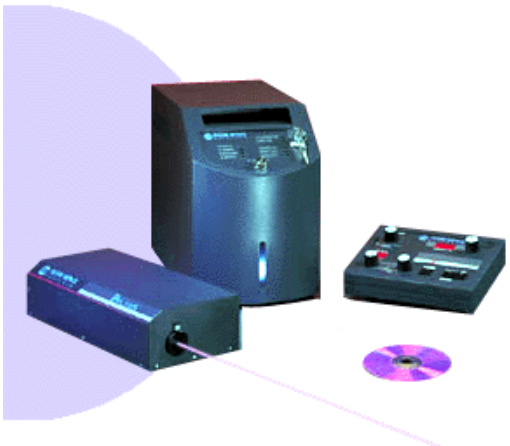

Source: New Wave Research, Inc.

Figure 3-2: Pulsed Nd:YAG laser used as ultrasound excitation source

Fiber Optic Beam Delivery System

The delivery of nanosecond scale laser pulses in the milijoule energy range through optical fibers was a challenging task. These operating conditions pushed the limits of high damage threshold, fused silica fibers. (Howard, 2002) The goal of the fiber delivery system was to deliver the required excitation energy through one fiber with a standoff distance between the delivery system and test specimen. A range of excitation spot sizes was desired to adjust the energy density of light striking a specimen surface. A more uniform beam profile with no "hot spots", a more robust system for injecting the laser energy into the fiber and a more rugged, durable delivery system were also desired.

Figure 3-3 is a schematic representation of the components of the fiber optic beam delivery system. This delivery system from US Laser Corporation consisted of an input coupling assembly, a rugged fiber optic cable with a 600 μm core diameter and an output focusing objective.

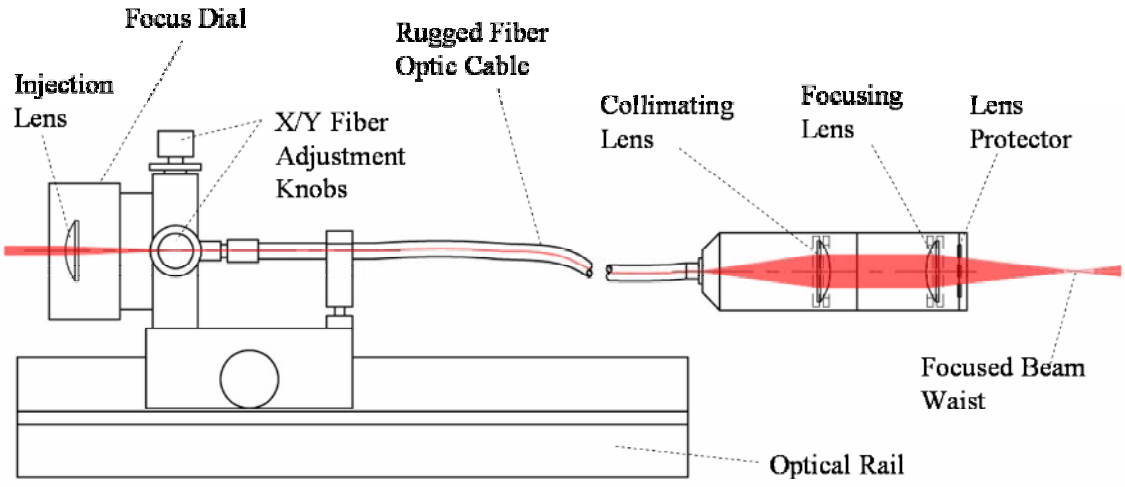

Figure 3-3: Fiber optic laser beam delivery system.

Fiber Optic Laser Doppler Vibrometer

As shown in Figure 3-4, the fiber-optic laser Doppler vibrometer is a model OFV-511 heterodyne fiber interferometer with an OFV-2700 Ultrasonics Vibrometer Controller purchased from Polytec Incorporated. The principle of heterodyne interferometer was shown previously in Figure 2-4. The vibrometer is used to directly measure the out-of-plane surface vibration response at selected points. Its sensor head is positioned perpendicular to and 55 mm away from the sample surface. The sensor head has a spot size of 3 μm to facilitate a high spatial resolution. The maximum range of displacement measurements is 150 nm peak-to-peak. The vibrometer has a displacement measurement resolution of 0.25 nm and a bandwidth from 25 kHz to 20 MHz. For a single detection point, multiple measurements are taken at a series of laser pulses and averaged to suppress signal noises. The output bandwidth of the vibrometer can be configured as to measure vibrations either up to 2 MHz or up to 20 MHz, depending on the application. The former has a smaller bandwidth but with better resolution. Most of the experiments are done with the 2 MHz bandwidth output as the signals of interest are normally below 2 MHz.

Figure 3-4: Polytec fiber optic heterodyne interferometer

X/Y Positioning Table

The X/Y positioning table, as shown in Figure 3-5 features excellent accuracy, orthogonality and bidirectional repeatability. The manufacturer's specifications claimed an accuracy of 7.5 μm per 100 mm of travel, orthogonality error of less than 7.5 arc-seconds and bidirectional repeatability of ±1.0 μm. The precision, preloaded, crossed-roller bearings in the stage eliminated the problems with play. The precision-grade lead screw drive also provides positioning accuracy and repeatability. The motion stage has a travel of 200 x 200 mm and a large mounting surface.

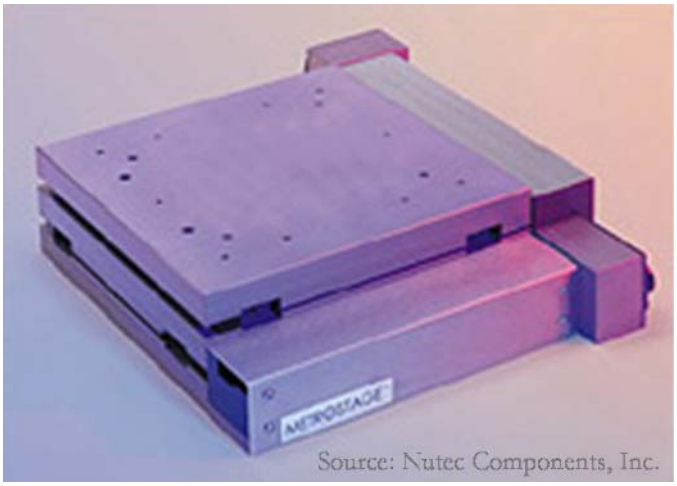

Figure 3-5: X-Y positioning table by Nutec.

The motion stage positions the test device under the vibrometer sensor beam for measurement. The positioning repeatability of the motion stage is verified to be approximately ±6 μm and ±4 μm in the X- and Y-axis, respectively.

Vacuum Fixture

During an experiment, a PCB is constrained by a vacuum fixture shown in Figure 3-6. This fixture consisted of a vacuum plate to hold test substrates as large as 152.4 x 203.2 mm. The vacuum plate had channels on its back surface to connect two vacuum ports in the fixture base plate to 48 individual ports in the vacuum plate. Two separate vacuum port arrangements for holding various specimen sizes were built into this fixture. A precision alignment fence was again used for repeatable component placement and orientation. The vacuum plate was clear anodized to improve its long-term durability and scratch resistance.

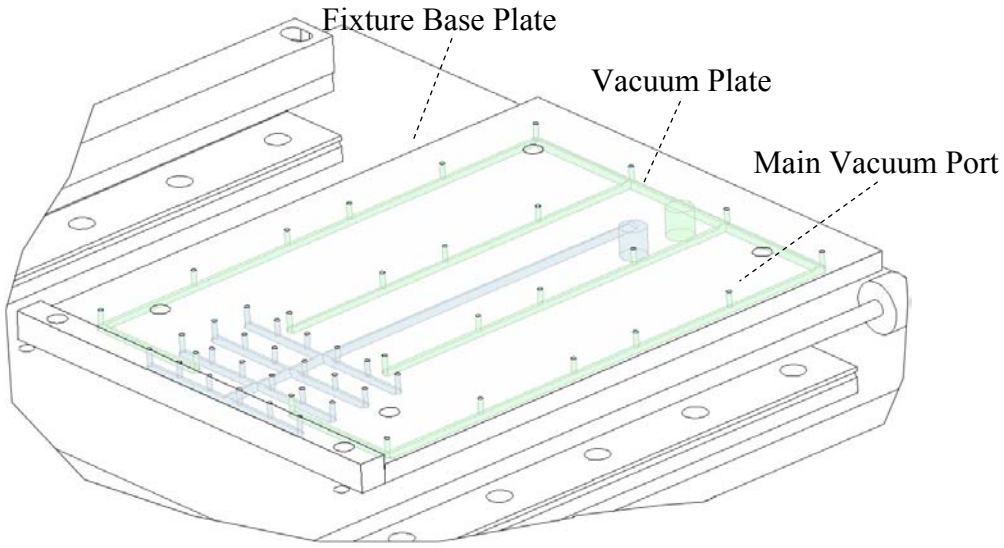

Figure 3-6: Vacuum specimen fixture.

Excitation Laser Positioning Stage

Repeatable excitation source positioning is realized by a manual X/Y stage shown in Figure 3-7. It uses preloaded linear motion components and linear encoders for

precision positioning. The stage was designed with a locking mechanism that allowed fine positioning through an adjustor screw when locked and rapid manual repositioning when unlocked. The linear encoders have 1.0 μm resolution, and the overall stage precision was estimated at better than ±10 μm in each axis.

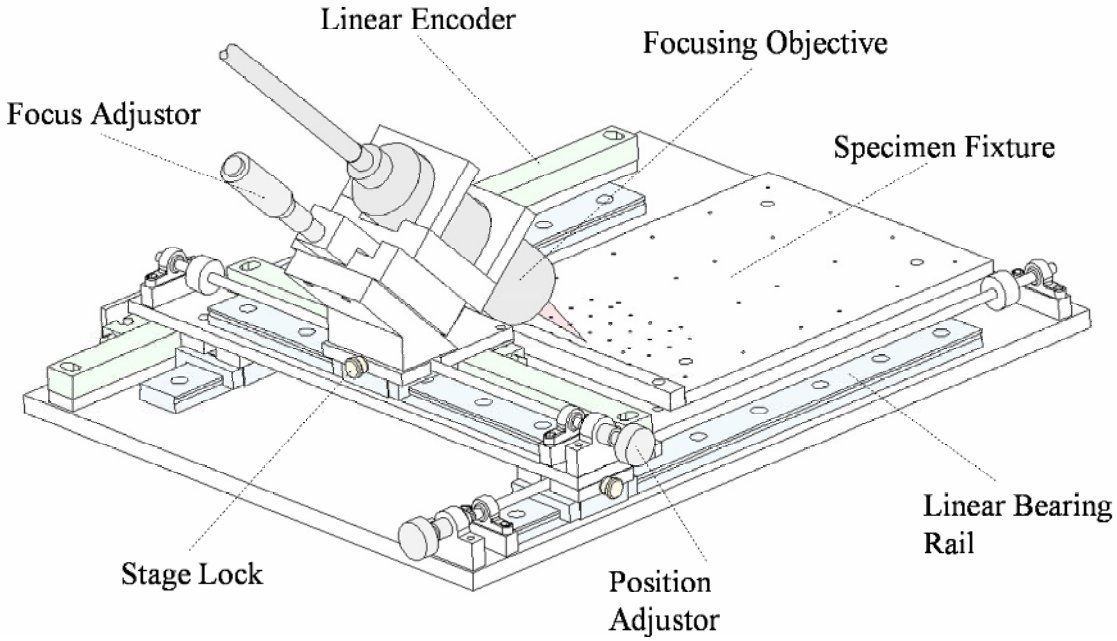

Figure 3-7: Manual X/Y laser excitation positioning stage.

The manual focus stage for the output objective of the fiber optic beam delivery system was mounted on the X/Y stage with a 45° angle mount, as shown in Figure 3-7. This focus stage had 25.0 mm of total travel, allowing the laser spot size to be adjusted over a wide range from the minimum possible beam diameter of 0.75 mm to spots larger than 2.5 mm for both the green and NIR wavelengths.

The laser spot imaged on a specimen was elliptical rather than circular because the output objective was mounted at a 45° angle to allow vibration measurement from

above. The range of possible excitation areas varied from 0.6 mm^2 to approximately 8 mm^2, providing much more flexibility in spot size.

Vision System for Fiducial Mark Locating

Fiducial marks are usually circular, square or cross-shaped solid pads on the printed wiring boards used for the placement of critical components on the PWB. The fiducial marks serve as reference features for board assembly machines that use vision systems to accurately place components on their corresponding bond pads. In much the same way, these fiducial marks were used to precisely align a specimen to be inspected with the interferometer measurement spot. The DVT Series 600 sensor (shown in Figure 3-8) selected for this research used a 3.6 x 4.8 mm CCD with 480 x 640 pixel resolution. This sensor produced 8-bit grayscale images and incorporated a number of useful software tools for easy image processing.

Figure 3-8: DVT series 600 CCD vision sensor for fiducial mark locating

For fiducial mark locating, the "blob" software tool was most effective because it grouped light or dark pixels together and then calculated the centroid position of the resulting blob of pixels. This tool was ideal for fiducial measurement because fiducial marks are often gold plated pads against the high contrast background of the substrate material, forming a bright spot in an image. The vision system comes with an alignment and calibration procedure to find the actual scale factor between units of pixels and real distance units, as well as to eliminate the image distortion.

The fiducial marks are measured with sub-micron resolution and ±1.0 μm repeatability in the view area of the vision system. Figure 3-9 shows the measurement of an actual fiducial mark on a test substrate.

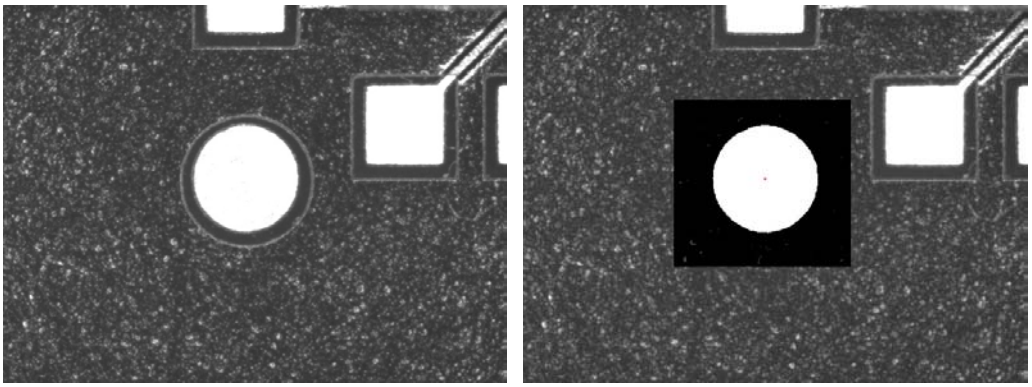

Figure 3-9: Blob measurement of fiducial mark. The raw image is shown at left and the fiducial blob is shown at right.

System Integration and Inspection Process Automation

The different components of the system have to be integrated to function as a whole. Also, the inspection process has to be automated to facilitate online inspection, reduce inspection cycle time, and to increase measurement repeatability.

During a typical inspection process, the vision sensor was programmed to read two fiducials from a given PCB first, then use a coordinate transformation program to calculate the translation and rotation of the measurement coordinate system and the coordinate system in the design file (Gerber file in this case). Once the translation distance and rotation angle are found, all coordinates in the design file can be transformed to the measurement coordinates and to locate the inspection and excitation points. The motion stage can be driven automatically to each inspection location and complete the inspection process.

Coordinate Transformation

In order to use fiducial measurements for accurate alignment to a specimen, the offset distance between the vision system coordinate frame and the laser vibrometer measurement spot was calibrated. The location of the excitation laser spot relative to the vision system was also calibrated for accurate positioning of the excitation source on the surface of a test specimen (Howard, 2002). Previous work also thoroughly examined all the coordinate frames necessary to locate and position a test specimen. Figure 3-10 shows the components of the system with their respective coordinate frames. Four coordinate systems were chosen to describe the inspection system from the base frame of the vision system to the local frame of a specimen on the test substrate (Chip A).

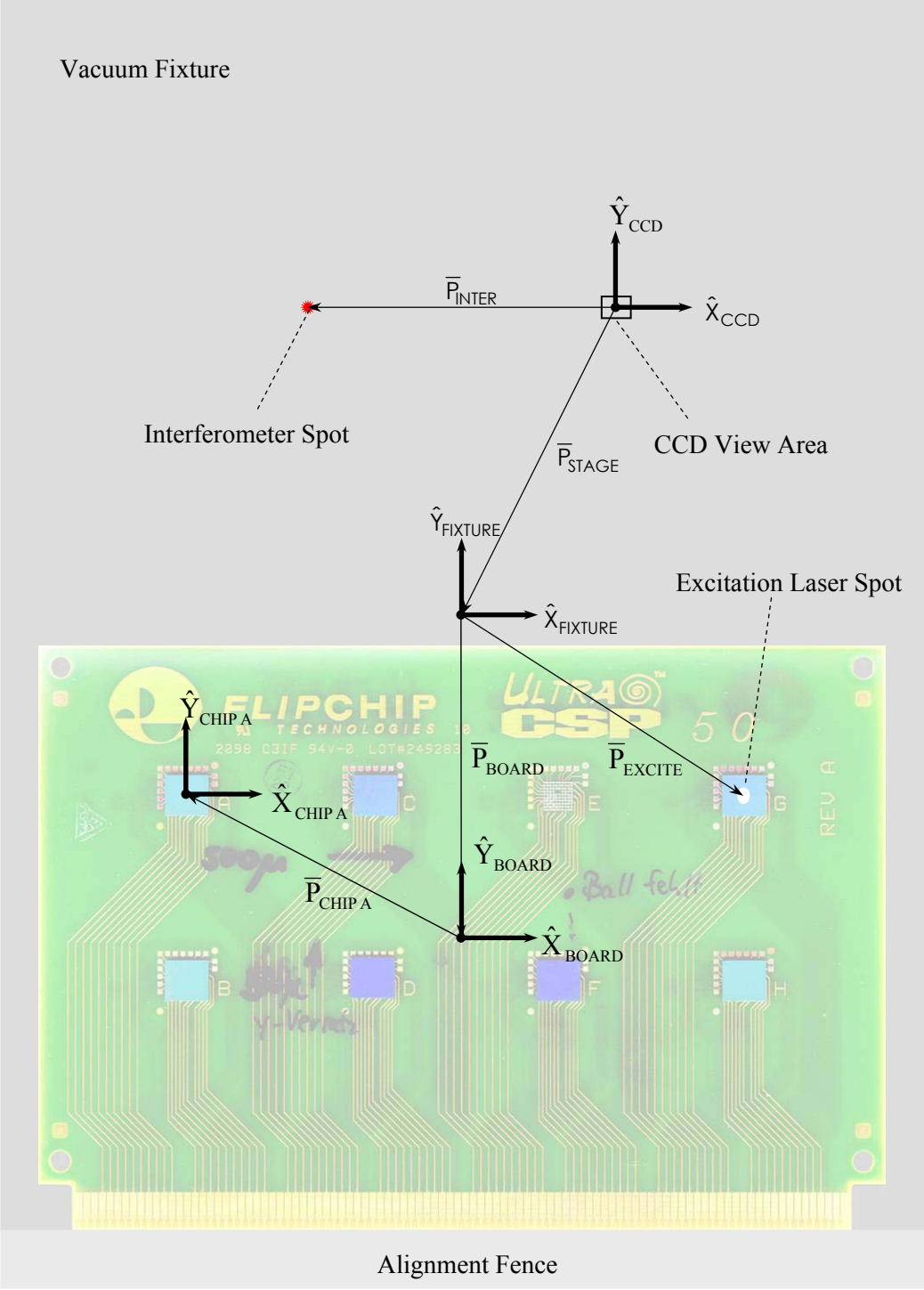

Figure 3-10: Coordinate frames for inspection. The chain of coordinate frames from the base frame (CCD) to the local specimen frame (Chip A) is shown. (Howard, 2002)

To complete the coordinate transformations, instead of finding out all of the translation and rotation data between all four coordinate frames as previously suggested, the method discussed below uses only two coordinate frames namely the PCB design coordinate system (the CAD frame) and the measured coordinates by the vision sensor (the measurement frame) to calculate the rigid body transformations. The method calculates both translation and rotation by measuring two fiducial points on the board under test and combining with their respective coordinates in the PCB design file (e.g. the Gerber file). Once the rigid body transformations, i.e. translation and rotation between the two frames are obtained, all the inspection and excitation locations can be transformed from the CAD frame to the measurement frame. The rotation transformation provides skew correction allowing the sample to be arbitrarily positioned on the fixture as opposed to having to be aligned against an alignment fence.

For discussion, the coordinates of a fiducial point in the CAD frame can be denoted as x' and y', the coordinates of that point in the measurement frame can be denoted as x and y, the translation between the two frames as X and Y, and the rotation between the frames as θ. We want to find out the translation (X and Y) and the rotation (θ) between the two frames by fiducial coordinates in these two frames. The translation matrix $T(X,Y)$ in a 2-dimensional homogeneous form can be written as:

$$\begin{bmatrix} x \\ y \\ 1 \end{bmatrix} = T(X,Y)\begin{bmatrix} x' \\ y' \\ 1 \end{bmatrix} = \begin{bmatrix} 1 & 0 & X \\ 0 & 1 & Y \\ 0 & 0 & 1 \end{bmatrix}\begin{bmatrix} x' \\ y' \\ 1 \end{bmatrix} \tag{2}$$

The rotation matrix $R(z,\theta)$ can be written as:

$$\begin{bmatrix} x \\ y \\ 1 \end{bmatrix} = R(z,\theta)\begin{bmatrix} x' \\ y' \\ 1 \end{bmatrix} = \begin{bmatrix} \cos\theta & -\sin\theta & 0 \\ \sin\theta & \cos\theta & 0 \\ 0 & 0 & 1 \end{bmatrix}\begin{bmatrix} x' \\ y' \\ 1 \end{bmatrix} \tag{3}$$

Thus, the composition of XY translation and z-axis rotation is:

$$\begin{bmatrix} x \\ y \\ 1 \end{bmatrix} = T(X,Y)R(z,\theta)\begin{bmatrix} x' \\ y' \\ 1 \end{bmatrix} = \begin{bmatrix} \cos\theta & -\sin\theta & X \\ \sin\theta & \cos\theta & Y \\ 0 & 0 & 1 \end{bmatrix}\begin{bmatrix} x' \\ y' \\ 1 \end{bmatrix} \tag{4}$$

Given two measured fiducial points: x_1', y_1', x_2', y_2', and their coordinates in the CAD frame: x_1, y_1, x_2, y_2, we can solve the simultaneous equations to find $\sin\theta$, $\cos\theta$, X and Y as below:

$$\sin\theta = \frac{(x_1' - x_2')(y_1 - y_2) - (x_1 - x_2)(y_1' - y_2')}{(x_1' - x_2')^2 + (y_1' - y_2')^2} \tag{5}$$

$$\cos\theta = \frac{(x_1 - x_2)(x_1' - x_2') + (y_1 - y_2)(y_1' - y_2')}{(x_1' - x_2')^2 + (y_1' - y_2')^2} \tag{6}$$

$$X = x_1 - x_1'\cos\theta + y_1'\sin\theta \tag{7}$$

$$Y = y_1 - x_1'\sin\theta - y_1'\cos\theta \tag{8}$$

Implementation of this coordinate transformation in Matlab can be found in Appendix A.

Once the coordinate transformation matrix is constructed, all inspection and excitation locations can be transformed from the CAD frame to the measurement frame. The motion stage control program then moves the fixture around for the interferometer to complete the inspection process.

Integration and Automation

The integration of sample positioning, laser excitation, interferometer measurement and data acquisition is mostly realized by communicating different devices with computer software, As all these systems come with either RS-232 or Ethernet interface as well as software development kits (SDKs).

For a given test board, the inspection pattern and excitation pattern are determined by the user first. The coordinates of these user selected points can be imported from the Gerber file. The test board is then held onto the vacuum fixture and its fiducials are read by the vision sensor. The above mentioned coordinate transformation program then finds out the translation and rotation matrix, and converts the inspection and excitation coordinates in the CAD frame into the measurement frame. These converted coordinates are fed into the motion control module, which will then control the motion stage to perform necessary homing sequences, and move to the first chip to be tested. The user is then prompted to align the excitation laser with already calculated coordinates. The sample is then moved to the first inspection point on the first chip to be tested. After focusing the interferometer manually (this part has not been automated at this time, but

interferometer with auto-focus feature is commercially available), the laser is fired, and the data acquisition is triggered at the same time, the interferometer output in the form of voltage is digitized and acquired. The data is stored with a predefined naming convention automatically. The stage then moves to the next inspection location automatically and the inspection process repeats. The C++ code controlling the stage motion and coordinating the data acquisition is listed in Appendix B.

The integration and automation of the system resulted in a reduced inspection time and improved throughput. The integration and automation also eliminated human intervention of the inspection process and thus reduces measurement variations and increase measurement repeatability. The system measurement capability is then characterized using a standard measurement system analysis (MSA) procedure in the following section.

Measurement System Analysis

Measurement is a process of evaluating an unknown quantity and expressing it as a numerical quantity. It is therefore subject to all the laws of variation and statistical process control (SPC). Oftentimes, measurements are made with little regard for the quality of such measurements. Measurement system analysis (MSA) is the scientific and statistical analysis of variation (ANOVA) that is induced into the process of measurement. A measurement system consists of not only the measurement instrument, but also the person using the measuring instrument, i.e. the appraiser, the environment under which the reading has been obtained, the methods used to setup and measure the parts, the tooling and fixture that locates and orients the object under measurement, and any

software that performs intermediate calculations and outputs the result. The reading obtained is thus influenced by each of these components and each component introduces a variation to the measurement process. Therefore, before embarking on using any new measurement systems for a characteristic which has not been previously measured on it, an MSA should be performed. MSA are critical to the success of every measurement and to ensure that future measurements will be representative of the characteristic being measured.

Measurement of surface vibration is such an essential part of the LUIS system being developed that all the information being used to evaluate a solder joint are extracted from the surface vibration signal. For this reason, the inspection system under development should also be considered as a piece of measurement equipment, and an MSA study of this system is necessary to prove its reliability and measurement capacity.

Rules for MSA Analysis

There are certain rules governing the MSA process that must be strictly adhered to in order to get meaningful result. Firstly, the measurements should be made in a random order to ensure that any drift or changes that occur due to unknown factors will be spread randomly throughout the study. Secondly, the operators should be unaware of which numbered part is being checked in order to avoid any possible knowledge bias. However, the person conducting the study should know which numbered part is being checked and record the data accordingly. For example, Operator A, Part 1, first trial; Operator B, Part 4, second trial, etc. The study should be observed by a person who recognizes the importance of the caution required in conducting a reliable study. The measurement procedure should be documented and all operators trained to the procedure

prior to the study. Finally, each operator should use the same procedure - including all steps - to obtain the readings. The LUIS's system stability and precision will be studied strictly following these rules.

Stability Study

Stability study statistically monitors the state of the measurement system over a period of time as shown in Figure 3-11. A measurement system will induce more variations in the readings due to wear and tear as it gets into use. Each measurement system will go out of stability after different intervals based on their usage. Rather than fixed period schedules, a stability test can be an excellent guideline to signal when a measurement system should be taken up for calibration. A stability test scientifically assures the predictability of the measurement system behavior over an extended time period. Stability can be evaluated using a control chart and plotting measurements on the same part over time.

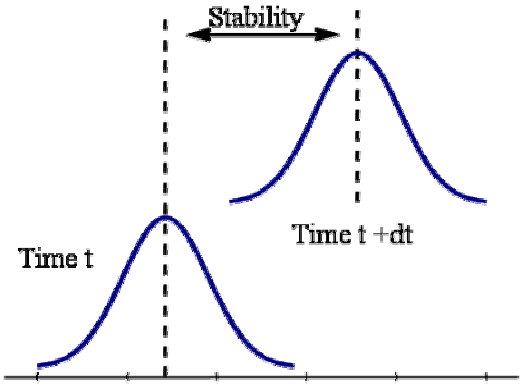

Figure 3-11: Stability is a consistency measure of the system performance over time

The stability study was performed according to the following procedure: 1) repeatedly measure the same chips at the same locations in different experiments at different times, 2) after each experiment, shut down the measurement system completely, and 3) obtain measurement data of the same chip at the same location across 20 different days. To study the stability, one chip with one inspection point is enough. However, two chips (a good chip and a thermal cycled chip) and 16 inspection points were used to get redundant data.

Figure 3-12 through Figure 3-14 shows plots of the calculated correlation coefficient or error ratio values across 20 different days on a control chart. In Figure 3-12, a reference chip was measured 20 times at the same inspection location on 20 different days, then, these measurements were compared to a measurement made on a reference chip. The result is plotted in an individual measurement control chart.

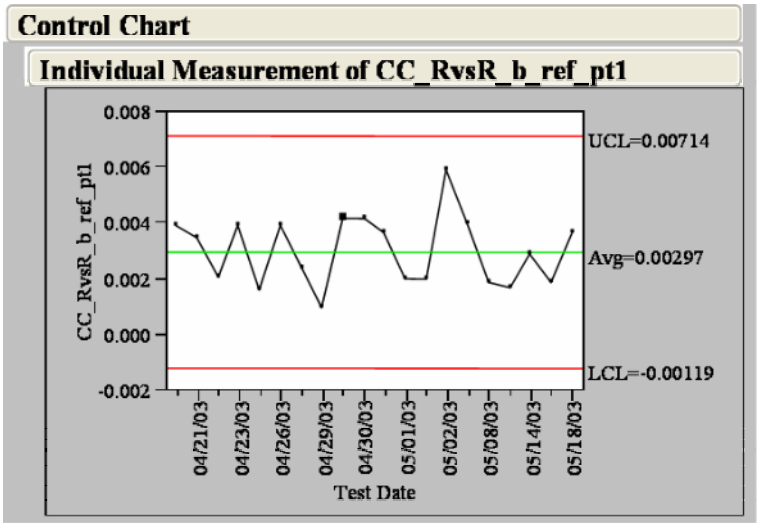

Figure 3-12: Control chart shows the correlation coefficient values measured and calculated from the same part at the same inspection location over 20 different days. All measurements are compared to a signal measured from a reference chip to calculate correlation coefficient. Chart shows a stable measurement system

In Figure 3-13 and Figure 3-14, both a reference chip and a defective chip were measured on each of the 20 days, and the measurements on each day were compared against each other using either the correlation coefficient (Figure 3-13) or the error ratio (Figure 3-14) method. All these figures show a stable measurement system.

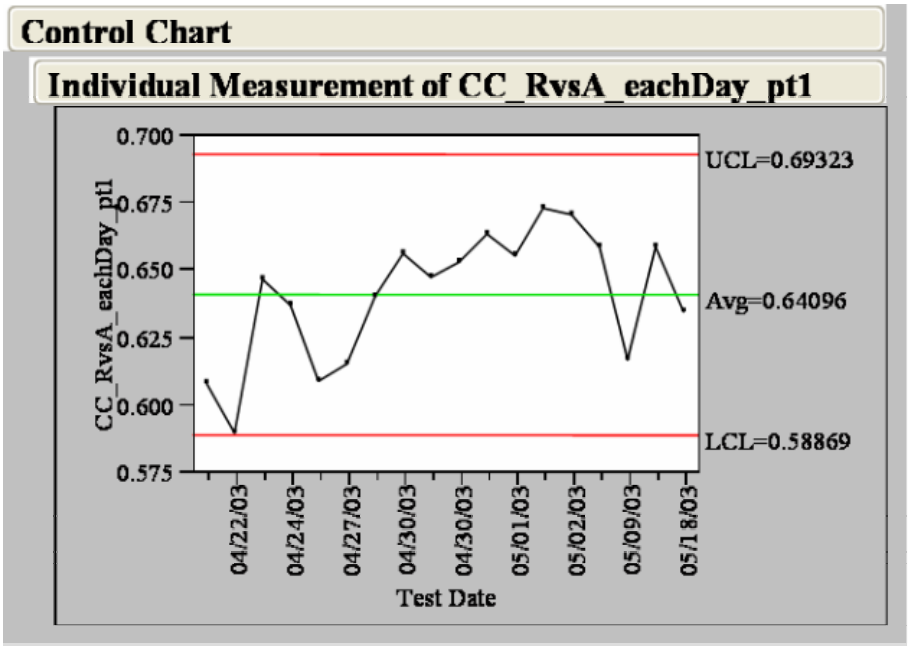

Figure 3-13: Control chart shows the correlation coefficient values calculated by comparing measurements from a defective chip and a reference over 20 different days. For each day, measurements were taken on both the reference and the defective chip, and a correlation coefficient value was calculated. Chart shows a stable measurement system.

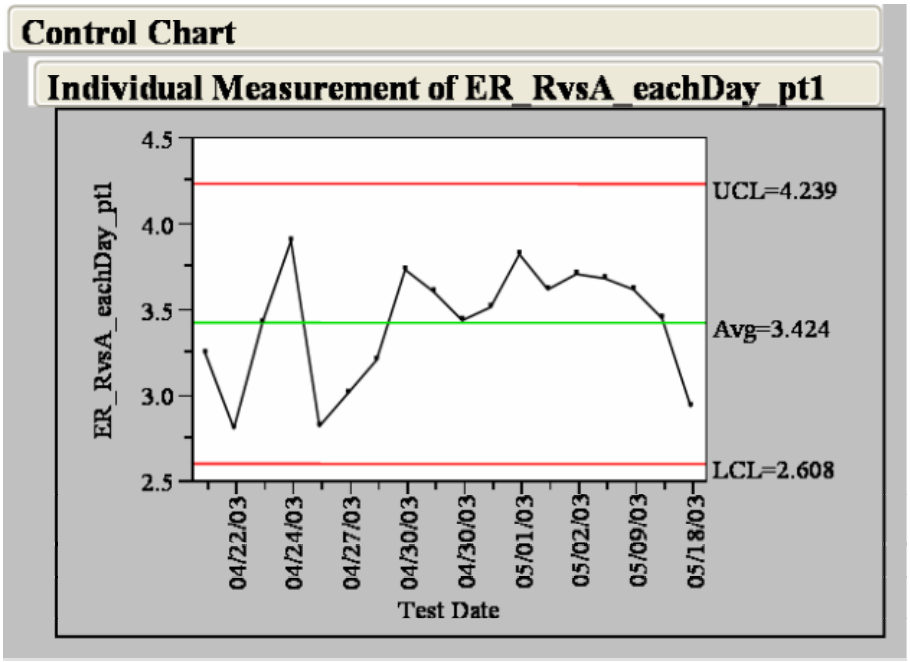

Figure 3-14: Control chart shows the error ratio values calculated by comparing measurements from a defective chip and a reference over 20 different days. For each day, measurements were taken on both the reference and the defective chip, and an error ratio value was calculated for that day. The chart shows a stable measurement system.

Gage Repeatability and Reproducibility (GR&R)

Gage Repeatability and Reproducibility (GR&R) methodology is used to understand the variations due to the measurement system. The objective of this study is to determine whether the measurement procedure and instrument is adequate for making measurements. Repeatability and reproducibility are two components of a GR&R study. Repeatability is the inherent deviation of the gage around the average value under repeated measurements of the same input by the same operator. Reproducibility is the variability due to the effects of different operators measuring the same input. The definitions for repeatability and reproducibility are represented by the diagram in Figure 3-15.

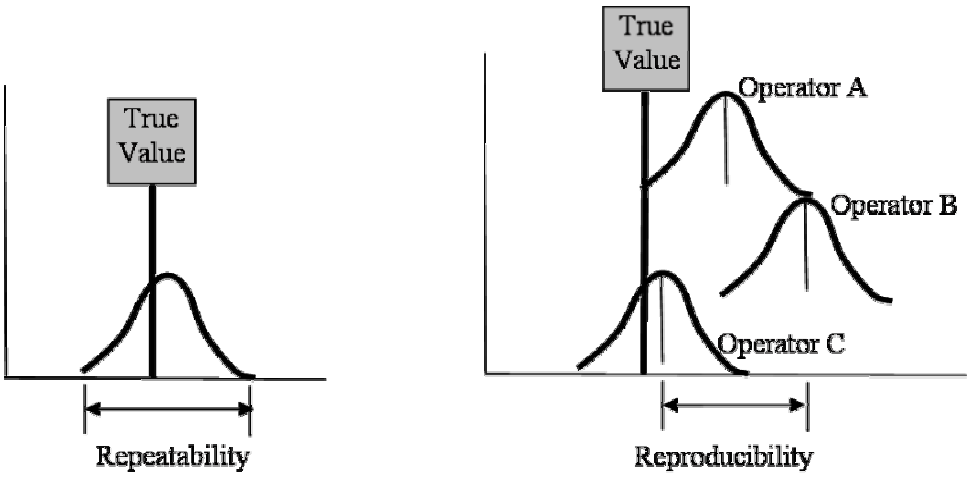

Figure 3-15: Definitions of repeatability (left) and reproducibility (right)

The objective of the GR&R study is to determine the amount of variability in a set of measurements taken on a single measurement instrument that can be attributed to the measurement instrument itself (repeatability) and to the entire measurement system (reproducibility). A GR&R analysis reports the attribution of each variation by using analysis of variance (ANOVA). The definitions of terms in GR&R analysis is listed in Table 3-1.

Table 3-1: Definition of terms and sums in GR&R analysis

Variances Sums	**Term**	**Abbr.**	**Alternate Term**
V(Within)	Repeatability	EV	Equipment Variation
V(Operator)	Reproducibility	AV	Appraiser Variation
V(Oper*Part)	Interaction	IV	Interaction Variation
V(Within)+V(Oper)+V(Oper*Part)	Gage R&R	RR	Measurement Variation
V(Part)		PV	Part Variation
V(Within)+V(Oper)+V(Oper*Part)+V(Part)	Total Variation	TV	Total Variation

For this GR&R study, ten sample boards including both good and defective samples were used. Two appraisers, D and L, performed the study in a completely randomized order. Each appraiser measured each part for three repetitions. Both appraisers used the same testing parameters and measured at the same designated locations. The detailed measurement procedure is:

- Randomly number the ten boards from 1~10.
- L measures boards 1 to 10 in the sequential order,
- D measures boards in the randomized order (5, 9, 2, 10, 1, 8, 7, 4, 3, 6)
- L measures boards in the randomized order (2, 6, 1, 9, 3, 8, 4, 10, 5, 7)
- D measures boards in the randomized order (10, 6, 3, 9, 7, 4, 5, 2, 1, 8)
- L measures boards in the randomized order (4, 10, 8, 1, 7, 2, 9, 6, 5, 3)
- D measures boards in the randomized order (9, 1, 4, 6, 8, 10, 2, 7, 3, 5)
- Then use one reference measurement as the reference, calculate the error ratios and correlation coefficients. The calculated error ratios or correlation coefficients are then used to calculate different types of variances. JMP software is used to calculate and plot the GR&R result.

ANOVA was performed on the data to calculate different sources of variability, including: appraiser variation (AV), part variation (PV), appraiser by part interaction variation (IV), and equipment variation (EV). These variations as well as total variations are calculated. Then the percent contribution of each component is calculated. Figure 3-16 and Figure 3-17 show the GR&R reports of measurement taken at two different locations generated by the JMP software.

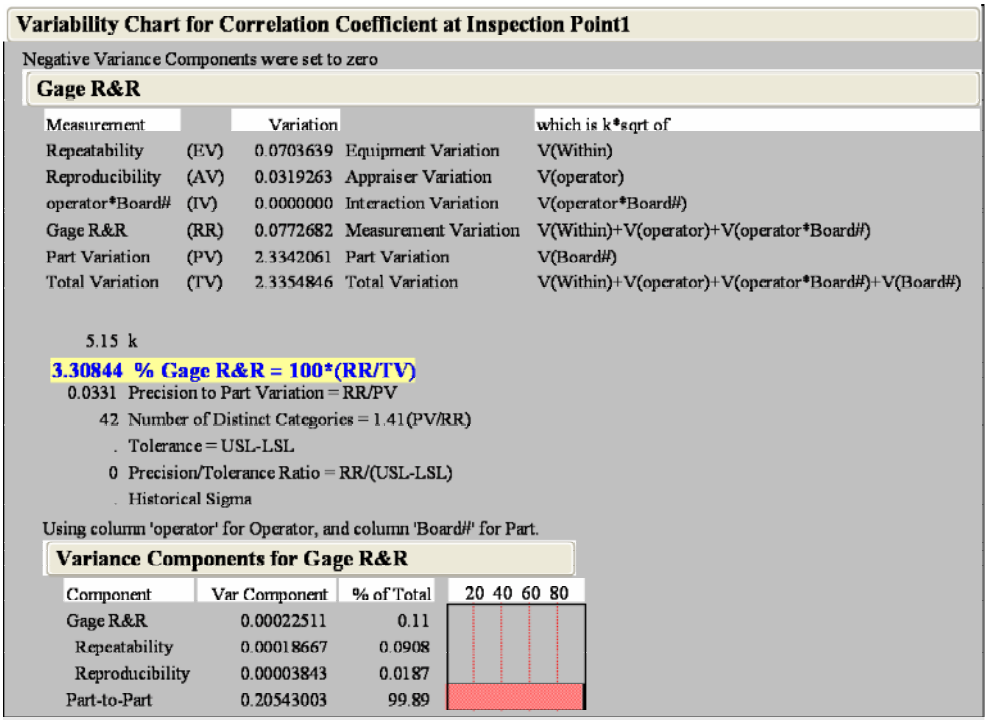

Variability Chart for Correlation Coefficient at Inspection Point1

Negative Variance Components were set to zero

Gage R&R

Measurement		Variation		which is k*sqrt of
Repeatability	(EV)	0.0703639	Equipment Variation	V(Within)
Reproducibility	(AV)	0.0319263	Appraiser Variation	V(operator)
operator*Board#	(IV)	0.0000000	Interaction Variation	V(operator*Board#)
Gage R&R	(RR)	0.0772682	Measurement Variation	V(Within)+V(operator)+V(operator*Board#)
Part Variation	(PV)	2.3342061	Part Variation	V(Board#)
Total Variation	(TV)	2.3354846	Total Variation	V(Within)+V(operator)+V(operator*Board#)+V(Board#)

5.15 k

3.30844 % Gage R&R = 100*(RR/TV)

0.0331 Precision to Part Variation = RR/PV

42 Number of Distinct Categories = 1.41(PV/RR)

. Tolerance = USL-LSL

0 Precision/Tolerance Ratio = RR/(USL-LSL)

. Historical Sigma

Using column 'operator' for Operator, and column 'Board#' for Part.

Variance Components for Gage R&R

Component	Var Component	% of Total
Gage R&R	0.00022511	0.11
Repeatability	0.00018667	0.0908
Reproducibility	0.00003843	0.0187
Part-to-Part	0.20543003	99.89

Figure 3-16: GR&R report showing a 3.3% GR&R at measurement location # 1

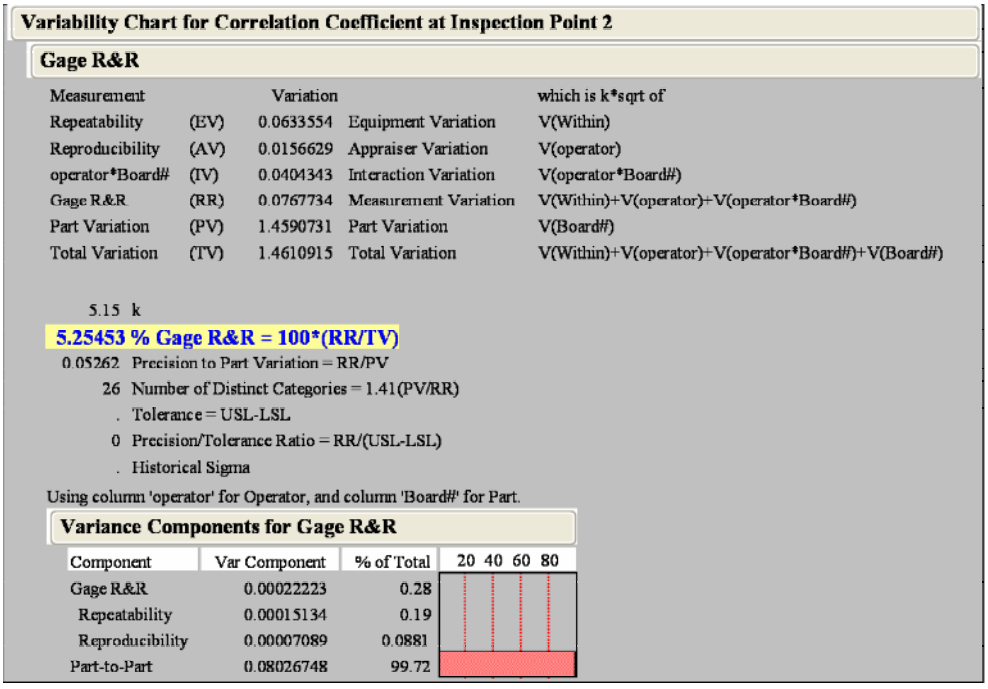

Variability Chart for Correlation Coefficient at Inspection Point 2

Gage R&R

Measurement		Variation		which is k*sqrt of
Repeatability	(EV)	0.0633554	Equipment Variation	V(Within)
Reproducibility	(AV)	0.0156629	Appraiser Variation	V(operator)
operator*Board#	(IV)	0.0404343	Interaction Variation	V(operator*Board#)
Gage R&R	(RR)	0.0767734	Measurement Variation	V(Within)+V(operator)+V(operator*Board#)
Part Variation	(PV)	1.4590731	Part Variation	V(Board#)
Total Variation	(TV)	1.4610915	Total Variation	V(Within)+V(operator)+V(operator*Board#)+V(Board#)

5.15 k

5.25453 % Gage R&R = 100*(RR/TV)

0.05262 Precision to Part Variation = RR/PV

26 Number of Distinct Categories = 1.41(PV/RR)

. Tolerance = USL-LSL

0 Precision/Tolerance Ratio = RR/(USL-LSL)

. Historical Sigma

Using column 'operator' for Operator, and column 'Board#' for Part.

Variance Components for Gage R&R

Component	Var Component	% of Total
Gage R&R	0.00022223	0.28
Repeatability	0.00015134	0.19
Reproducibility	0.00007089	0.0881
Part-to-Part	0.08026748	99.72

Figure 3-17: GR&R report showing a 5.3% GR&R at measurement location # 2

The guidelines of an acceptable percent R&R is suggested as (Barrentine, 1991): If the percent R&R is less than 10%, the system has excellent repeatability and reproducibility; if the percent R&R is between 11% and 20%, the system has adequate repeatability and reproducibility; otherwise if the percent R&R is between 21% and 30%, system repeatability and reproducibility is marginally acceptable; The system repeatability and reproducibility is unacceptable if the percent R&R is greater than 30%, corrective actions need to be taken before the measurement tool can be used. From the GR&R reports obtained in this study, the system percent GR&R is less than 10% regardless of the measurement locations. Thus, the integrated and automated system has excellent repeatability and reproducibility.

CHAPTER 4

INTERPRETATION OF VIBRATION SIGNALS: TIME- AND FREQUENCY-DOMAIN SIGNAL ANALYSIS

The previous chapter discussed the construction and integration of the LUIS system to facilitate a repeatable and precise surface displacement measurement under pulsed laser excitation. A significant part of this research is to determine how to interpret and relate the measured vibration signals, i.e., out-of-plane displacement data at different locations of the sample surface, to the qualities of solder joints is a significant part of this research. In this chapter, the measured vibration signals are examined both in the time-domain and in the frequency-domain, different signal processing methods are developed or introduced to relate the vibration signals to actual solder joint interconnection quality. Time-domain correlation coefficient analysis was introduced as a method complimentary to the previously developed Error Ratio method. An Auto-Comparison method was developed to eliminate the reliance of a reference chip when performing solder joint inspection. In order to extract vibrational mode frequencies precisely in the frequency domain, a number of spectral estimation algorithms were examined and implemented.

Time-Domain Signal Correlation Coefficient Analysis

Figure 4-1 shows signals collected from a single point on five different boards. These signals are collected from the same chip location on each panel in order to minimize positional variations. The waveforms of three reference signals match each

other well, while the other two waveforms from thermally cycled samples deviate from the reference signals.

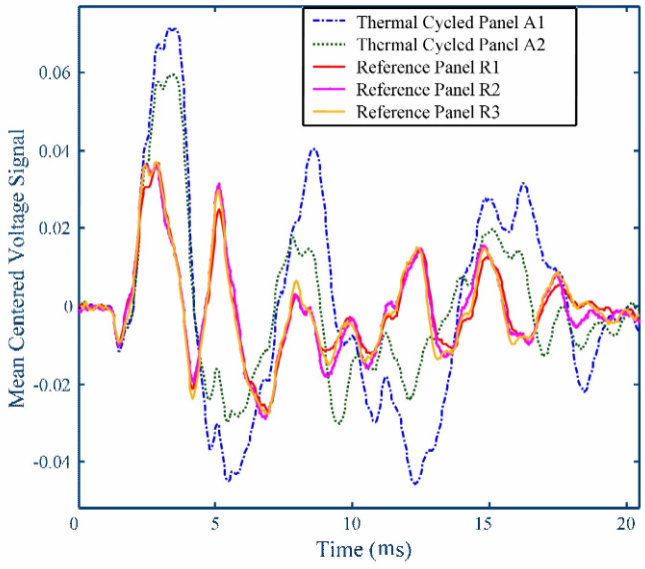

Figure 4-1: Waveforms of signals collected at the same location on five different chips. The laser pulse durations are 4~5 ns, and the laser power is 70mW.

To quantitatively identify the signal differences, Liu et al (2003) used the error ratio (ER) method. This method integrates the total squared error between the waveforms, and then normalize this integrated value by one waveform chosen to be as reference. The ER is computed using equation (9),

$$ER = \frac{\int [f(t) - r(t)]^2 \, dt}{\int [r(t)]^2 \, dt} \qquad (9)$$

where f(t) is the measured waveform, and r(t) is the reference waveform.

Since a number of factors other than the solder joint integrity itself affect ER values, there are some limitations with this method. The scale of the ER depends on the device being tested and should only be used for relative comparisons between similar product types (Howard et al, 2002). This limitation makes it difficult to set up a universal threshold ER to separate defective samples from reference samples. ER values can also be affected by laser power fluctuation. To better explain this, vibration signals at the same detection point on the same chip were collected at different laser power levels and are plotted in Figure 4-2. The figure shows that the vibration waveform amplitude increases with increasing excitation laser power, but the waveform shape changes very little. Since the ER calculation uses integration of the amplitude differences, the amplitude change caused by laser power variation will change the ER, although theoretically the ERs in these cases should remain zero.

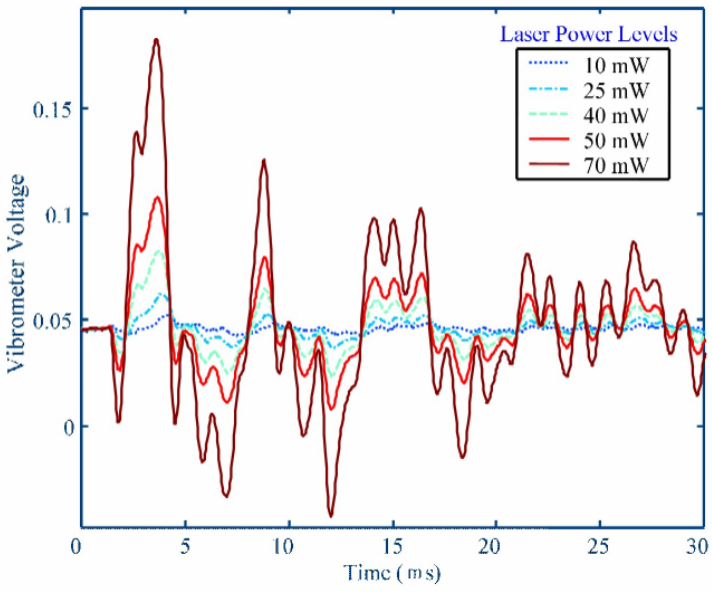

Figure 4-2: Signals collected from the same point at different laser power levels

Since the laser power fluctuation causes little change in signal frequency and phase, an algorithm, which is insensitive to signal amplitude but is able to reflect the change of signal phase and frequency, is needed to factor out the effect of power fluctuation.

The scatterplots in Figure 4-3 are generated by using amplitudes of two signal sequences as the X and Y coordinates, respectively. Figure 4-3(a) clearly shows that signals obtained from different reference samples have some extent of linear dependence, while Figure 4-3(b) shows the signals from the reference and defective samples are quite independent. The linear relationship between two reference signals forms the basis for the correlation coefficient calculation.

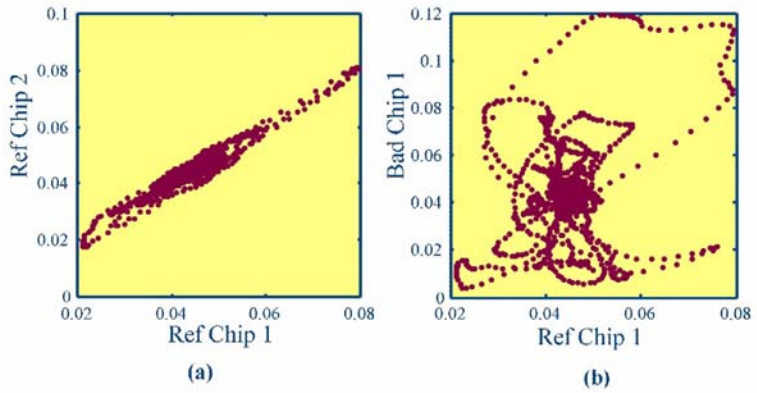

Figure 4-3: Signal scatterplots of (a) two reference chips and (b) a reference chip with a thermally cycled chip

The correlation coefficient, *r*, is calculated by (Hayter, 2002),

$$r = \frac{\sum_n (R_n - \overline{R})(A_n - \overline{A})}{\sqrt{\left(\sum_n (R_n - \overline{R})^2\right)\left(\sum_n (A_n - \overline{A})^2\right)}} \qquad (10)$$

where R_n is the reference signal, $\bar{R}$ is mean of R_n, A_n is the signal to be compared with R_n, $\bar{A}$ is the mean of A_n.

The correlation coefficient is a scalar value which lies between -1 and 1. The correlation coefficient is a normalized measure of the strength of the linear relationship between two vectors. A value of r equals to 1 indicates that the two vectors R_n and A_n correlate positively and perfectly. If on the other hand the two vectors vary oppositely and perfectly, r will be equal to -1. If the two vectors vary independently, then r will be equal to 0. The previously used ER method gives larger values when the differences between two signals are large. In order to make the correlation coefficient results consistent with those of ER and to limit the result in the range of 0 to 1, a modified correlation coefficient, $(1 - r^2)$, was used in this analysis instead of r. Thus, when $(1 - r^2)$ equals to 1, the two signals are independent, and when $(1 - r^2)$ is close or equal to 0, the two signals have strong linear dependence.

Figure 4-4(a) shows the modified correlation coefficient (MCC) analysis results of two reference chips. The two chips are at the same location on two different panels. The mean value of $(1 - r^2)$ is about 0.03, indicating strong linear relationship. Figure 4-4(b) shows the analysis results of a reference chip and a thermally cycled chip. The two chips are at the same location of two different panels. The mean value of $(1 - r^2)$ in this case is 0.917, indicating that the signals from a reference (good) chip did not correlate well with the signals from a thermally cycled (cracked) chip. Furthermore, the maximum value of $(1 - r^2)$ resulting from the comparisons between the reference chips is 0.197, which is much less than the minimum $(1 - r^2)$ value of comparisons between a reference

and a cracked chip. If, for instance, a user sets a threshold (1 - r^2) value equal to 0.4, then the quality of chip's solder joint connection can be checked by inspecting any point on the chip surface. Comparison of signals collected from all 36 chips with bad electrical connections on the two thermal cycled panels with reference chips with good connections showed high values of (1 - r^2) close to 1, while the results of the 54 reference chips had very low values of (1 - r^2) when compared with each other.

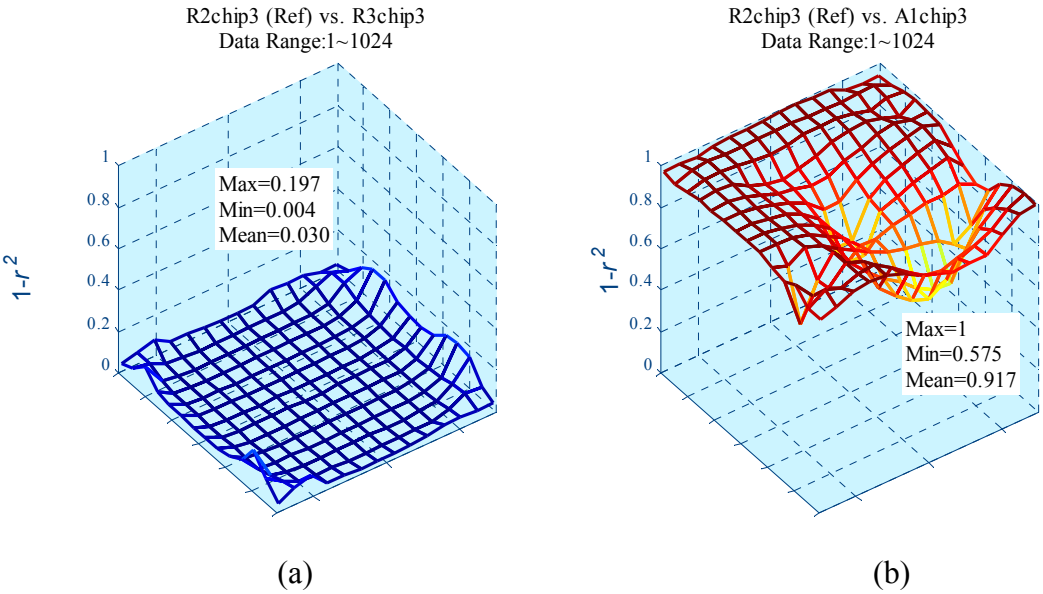

(a) (b)

Figure 4-4: Modified correlation coefficient values of: (a) two reference chips and (b) a reference chip with a thermal cycled chip.

Effects of Laser Power Variations

The effects of laser power fluctuation on ER analysis and MCC analysis were investigated. Signals were collected from the same point on the same sample while adjusting the laser power level from 25 mW to 70 mW. The signal collected when the laser power level was set at 57 mW was chosen as the reference signal, and this signal

was used to compare the other signals for both ER and MCC analyses. Ideally, ER and the MCC values should be close to zero. Figure 4-5 shows the results of both the ER and the MCC values. The MCC values are all close to 0 when the laser power level is between 45 mW and 70 mW, but the ER values have significant variation even when the power level is near 57 mW. Fifty seven mW was chosen as the reference power level because it was the power level setting used in this study. If a different power level such as 50mW was chosen as the reference, a similar trend is observed. The excitation laser power has to be within a certain range. It has to be high enough to generate measurable and less noisy vibration signals, but not too high to go beyond the thermoelastic regime and cause ablation. The fiber optic laser beam delivery system has a damage threshold of about 85mW, which imposes another upper bound for the laser power setting. Experiments show that for this flip chip sample, a power level between 50 mW and 70 mW is appropriate. When the laser power is set within this range, the MCC method allows a wider range of laser power variation than the ER method. The figure also shows that when the laser power is below 40 mW, both the ER value and the MCC value increase and deviate from 0. This means that in order to get comparable data, the laser power used in exciting both the reference chip and the defective chip has to be kept in a range of about ±10 mW. This condition can be easily met with a fixed laser attenuator setting.

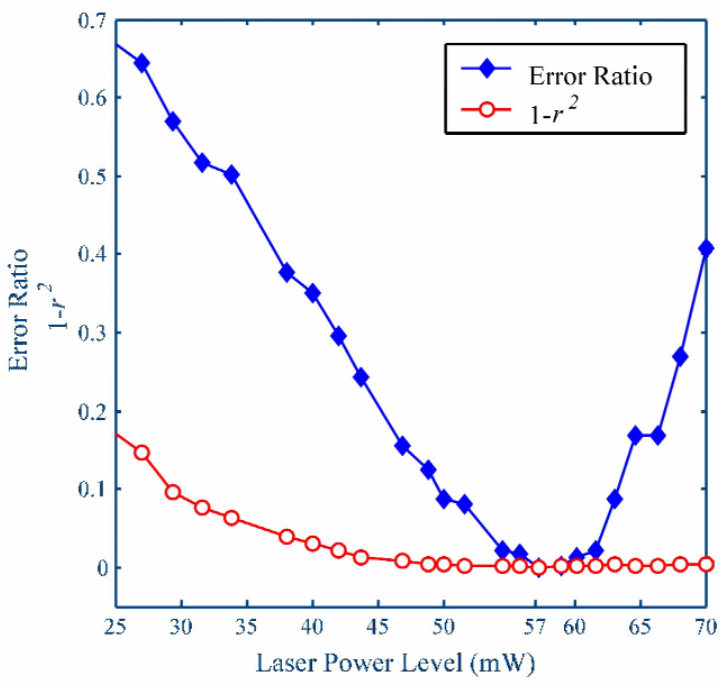

Figure 4-5: Effects of laser power level on ER and MCC methods

By choosing the optimum inspection locations, only a few inspections may be enough. Figure 4-6 shows the average MCC values collected at different distances from the center of the chip. When comparing defective chips (on panel A1 and A2) with a reference chip (on panel R2), the closer the inspection points are to the chip edge (solder bump locations), the higher the MCC values are, but the closer they are to the chip center (excitation point), the smaller the MCC values. For the comparison between two reference chips (on panels R2 and R3 respectively), the MCC values vary in the same pattern but in a much smaller range. This observation indicates that the locations closer to the solder joints are the optimum choices for inspection. Analyses have shown that by using the data collected on the four corners of the chip, evaluating the chip's solder joint quality using the MCC method is sufficient.

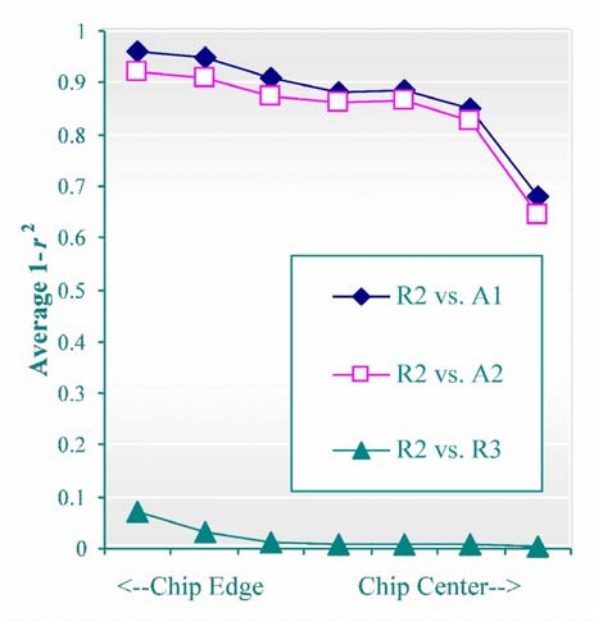

Figure 4-6: MCC value distribution over the chip surface (R2 and R3 are reference panels, A1 and A2 are temperature cycled panels)

Auto-Comparison Method

All the above mentioned identification methods rely on a reference chip(s) with "known good" solder joints. Finding such a reference chip can be a problem in practice. To find a method that can inspect a chip using only data collected from the chip being inspected, the vibration responses of the whole chip surface were studied. Figure 4-7 shows a raster scan inspection pattern used to get a detailed vibration response of the chip surface. The excitation laser beam was projected at the center of the chip surface, as indicated by the elliptical shape in Figure 4-7. The vibrometer inspection points are denoted by the 14 x 14 star arrays. This 14 x 14 points inspection pattern is selected so that the pitch of the inspection points is the same as the solder bump pitch, and each

solder bump has an inspection point right on top of it. The 48 gray circles on the peripheral of the chip are the solder bump locations.

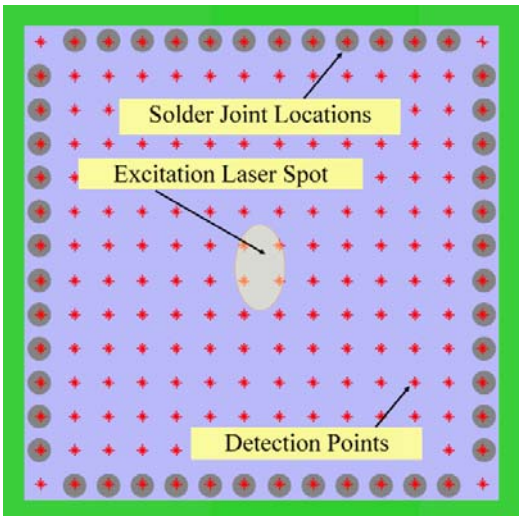

Figure 4-7 Top view of test device indicating points of excitation and detection, the red stars represent the detection locations, the grey circles represent the solder joint locations, and the elliptical spot at the center represents the excitation laser spot.

Figure 4-8(a) shows the vibration shape at the instant 6.4 μs after the laser excitation of a reference chip. A very regular circularly symmetric pattern was observed. Figure 4-8(b) shows the shape of a thermally cycled chip at the same time instant. This difference between the reference chip and the thermally cycled chip was observed during the whole response period.

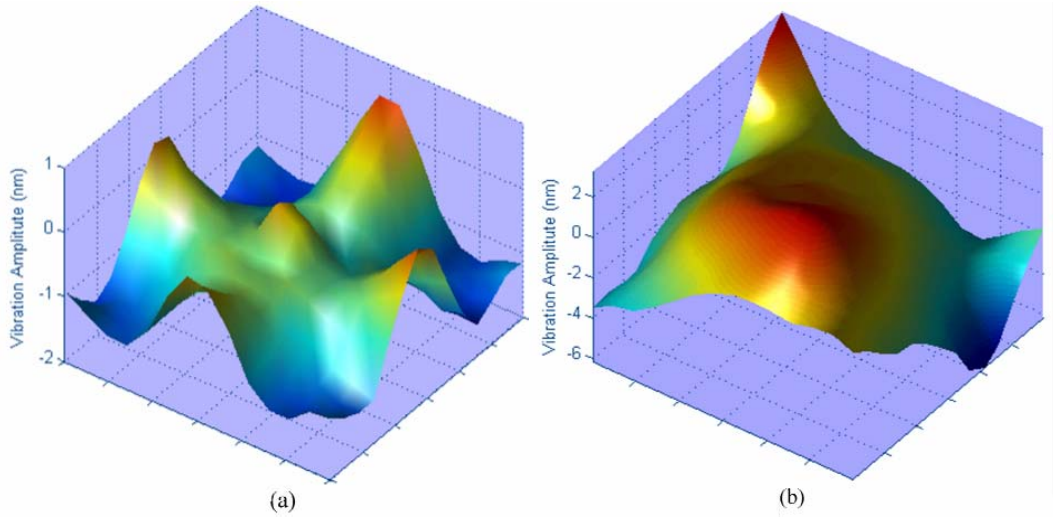

Figure 4-8: Surface response of: (a) a reference chip, and (b) a thermally cycled chip at the same time instant

Figure 4-9 shows the surface contour plots at two time instants. Figure 4-9(a) and Figure 4-9(b) give the response of a reference chip at two time instants. Both show circularly symmetric patterns. Figure 4-9(c) and Figure 4-9(d) show the response of a thermal cycled chip at the two time instants. Note that Figure 4-9(b) and Figure 4-9(d) are contour plot representations of the vibration shapes shown in Figure 4-8(a) and Figure 4-8(b), respectively. Since the chip's bumps are symmetrically distributed and the laser excitation point is located at the center of symmetry, if all the solder joints are well-connected, then the response should show a symmetric shape as verified by the experimental data. The asymmetric response shape of the thermally cycled sample indicates weak solder joint connections at some locations. Whether or not the system can indicate the precise locations of cracked solder joints is not required for a go/no go inspection and is not discussed in this study.

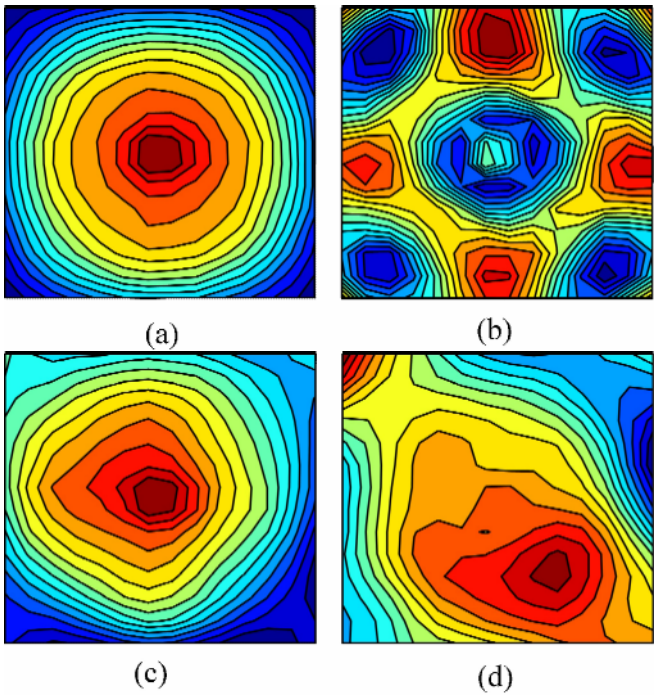

Figure 4-9: Contour plots of surface vibration responses

The above observation shows that comparing signals collected from symmetric locations on a single chip can be used to evaluate the chip's solder joints. As long as the chip's bump locations are symmetrically distributed (most IC packages have this kind of symmetry) and the laser excitation point is located at the center of symmetry, the symmetry of the surface's vibration shape should reflect the quality of the solder joint connections. Both ER and MCC analyses can be used to perform "Auto-Comparison" – comparing data from symmetric locations on the same chip.

Figure 4-10 shows the result of the Auto-Comparison method. A total of 90 samples on five different panels were analyzed. For each sample chip, only four signals collected from the four corners of the chip were used for calculation. The signal detected from the lower left corner of the chip was compared with the one detected from the upper right corner, the signal detected from the lower right corner was compared with the one

from the upper left corner, all using the MCC method. The two ($1-r^2$) values were then averaged to give the final value for the test. In Figure 4-10, the three rows in the front are the results for the chips located on panels R1, R2, and R3. All reference panels have good solder joint connections. The average values of MCC are all lower than 0.1 with only one exception (Chip 7 on panel R2). The two rows in the back are the results for the chips located on panels A1 and A2, which are both thermally cycled panels. The values of MCC are much higher than those of the reference group. A threshold value of 0.2 for the MCC would successfully separate all the 36 chips with bad connections from the 54 well-connected chips.

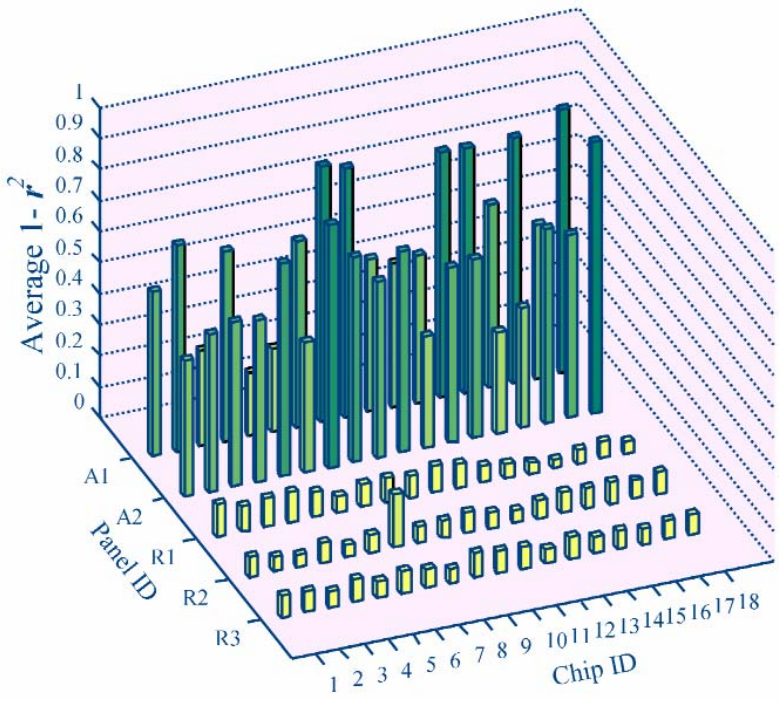

Figure 4-10: Auto-Comparison results of 90 flip chips mounted on five different panels: A1, A2, R1, R2, and R3. MCC values were used to perform Auto-Comparison

In summary, the Auto-Comparison using the MCC calculation can evaluate the chip's solder joint connection using only a few number of symmetrically distributed inspection points, provided that the component shape and solder bump distribution have symmetry, and the laser excitation source is at the symmetry center.

Frequency-Domain Spectral Estimation

As explained in Chapter 2, the LUIS system uses pulsed laser excitation to cause structural vibration in the chip to substrate assembly. The surface displacement signals measured thus represent the impulse response of the chip-solder joint-substrate structure. There are natural frequencies associated with any mechanical structure, and resonance will occur at these frequencies under excitation. The chip-solder joint-substrate structure can be modeled as a thin plate connected to a constrained surface via solder joints. When there are defects in the solder joints, the natural frequency will change. The surface displacement signals generated under impulse excitation contains the modal information of the structure. The signal power will be concentrated at certain mode (natural) frequencies. Spectral estimation techniques can help obtain the mode frequencies from the raw data precisely. Thus, it is very important to look at these vibration signals in the frequency domain using spectral estimation techniques to extract the resonance frequencies.

The goal of spectral estimation is to describe the distribution (over frequency) of the power contained in a signal, based on a finite set of data. The quality of the estimated spectrum depends on: a) how well the assumed signal model represents the data, b) what values we assign to the unavailable signal samples, and c) which spectrum estimation

method is used. Meaningful application of spectrum estimation in practical problems requires sufficient a priori information, understanding of the signal generation process, knowledge of theoretical concepts, and experience. The various spectral estimation methods can be categorized into nonparametric methods, parametric methods, and subspace methods. In the following sections, both nonparametric methods and parametric methods will be examined and compared to find out the most suitable spectral estimation method for this application.

Nonparametric Methods

Nonparametric techniques do not assume a particular functional form of the signal model, but allow the form of the estimator to be determined entirely by the data, i.e., the power spectral density (PSD) is estimated directly from the signal itself. These methods are based on the discrete Fourier transform (DFT) of either the signal segment or its autocorrelation sequence. Periodogram averaging is the simplest method in this category. An improved version of the periodogram is Welch's method (Welch, 1967). A more modern nonparametric technique is the multi-taper method (MTM).

PSD Estimation via Periodogram

The periodogram is an estimator of the power spectrum, introduced by Schuster (1898) in his efforts to search for hidden periodicities in solar sunspot data. The *periodogram* of the data segment $\{x(n)\}_0^{N-1}$ is defined by:

$$\hat{R}_x\left(e^{j\omega}\right) = \frac{1}{N}\left|\sum_{n=0}^{N-1} v(n)e^{-j\omega n}\right|^2 = \frac{1}{N}\left|V\left(e^{j\omega}\right)^2\right| \qquad (11)$$

where $V\left(e^{j\omega}\right)$ is the discrete-time Fourier transform (DTFT) of the windowed sequence

$$v(n)=x(n)w(n)\,,\quad 0 \le n \le N-1 \tag{12}$$

Usually, the term *periodogram* is used when the window function $w(n)$ is a rectangular window. While the term *modified periodogram* is used to stress the use of nonrectangular windows such as the hamming window, the hanning window, etc.

The resolution of the periodogram, i.e., its ability to discriminate spectral features depends on the sampling frequency f_s and the data length L. For two sinusoids of frequencies f_1 and f_2, the resolvability condition requires that

$$\Delta f = f_1 - f_2 > \frac{f_s}{L} \tag{13}$$

The data acquisition program of the LUIS system normally takes 2,048 data points (L=2048), thus the resolution can be improved by reducing the sampling frequency f_s. Figure 4-11 shows a typical measured waveform using a sampling frequency of 10 Mhz.

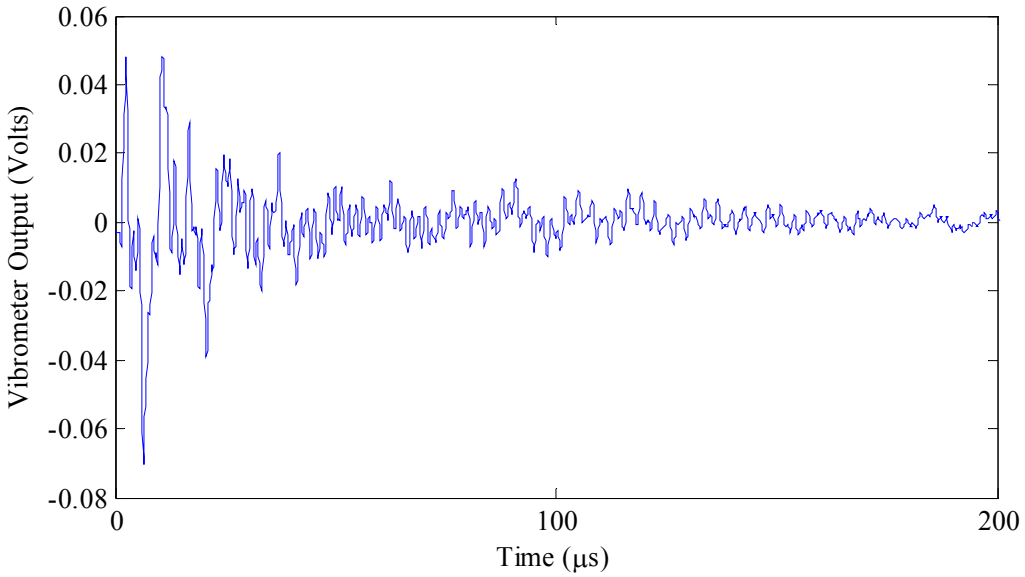

Figure 4-11: A typical measured vibration waveform

The periodograms of the same signal but acquired at different sampling frequencies are plotted in Figure 4-12 through Figure 4-14. The Plots clearly show that at lower sampling frequency (5 MHz), a better frequency resolution is obtained in the periodograms. However, the sampling frequency must be higher than 4 MHz to avoid aliasing, since the output signal from the interferometer is pre-filtered with a low pass anti-aliasing filter with a cut-off frequency of 2 MHz.

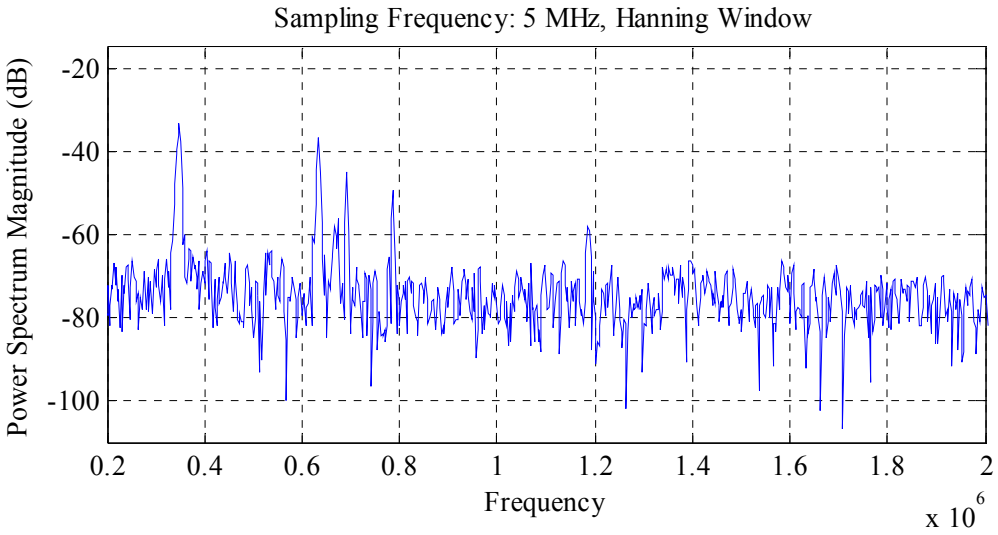

Figure 4-12: Periodogram of signal in Figure 4-11 using 5 MHz sampling frequency

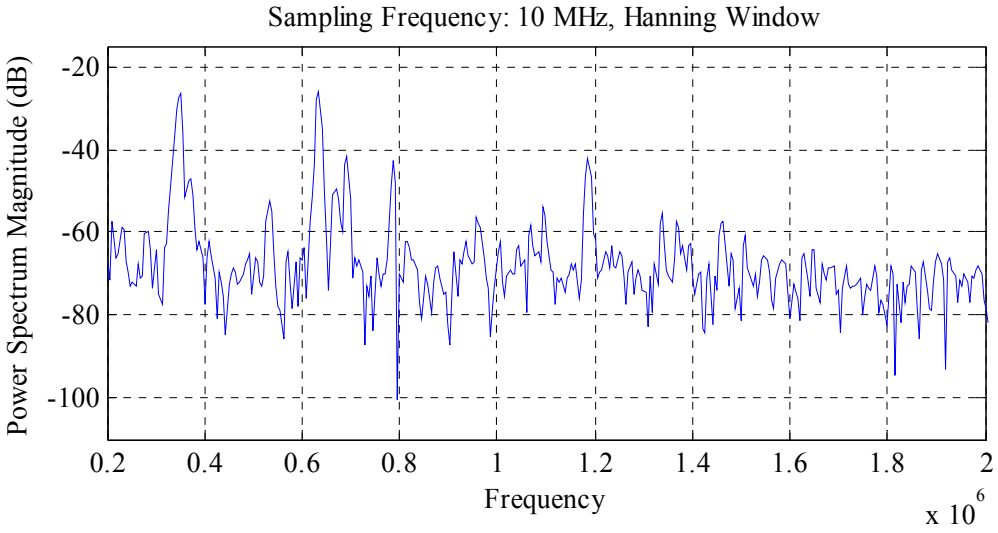

Figure 4-13: Periodogram of signal in Figure 4-11 using 10 MHz sampling frequency

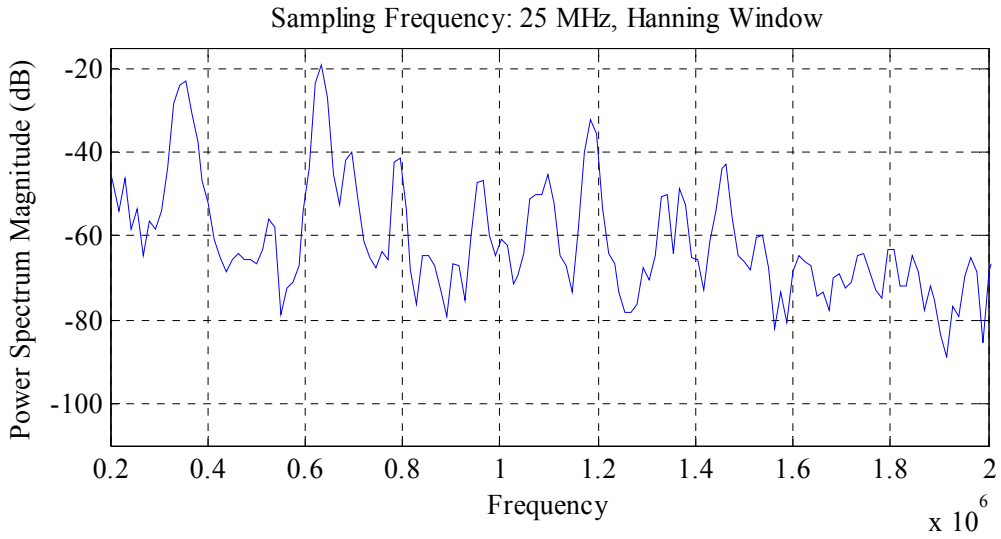

Figure 4-14: Periodogram of signal in Figure 4-11 using 25 MHz sampling frequency

The major problem with using a periodogram or a modified periodogram lies in its variance. The variance of the periodogram can be shown to be approximately:

$$\operatorname{var}\left\{\frac{|X_L(f)|^2}{f_s L}\right\} = P_{xx}^2(f)\left[1+\left(\frac{\sin(2\pi L f / f_s)}{L\sin(2\pi f / f_s)}\right)^2\right] \qquad (14)$$

which indicates that the variance does not tend to zero as the data length L tends to infinity. In statistical terms, the periodogram is not a consistent estimator of the PSD. Nevertheless, the periodogram can be a useful tool for spectral estimation in situations where the signal-to-noise ratio (SNR) is high, and especially if the data record is long.

PSD Estimation via Welch's Method

To reduce the variance, the Welch method consists of dividing the time series data into (possibly overlapping) segments, computing a modified periodogram of each

segment, and then averaging the PSD estimates. The result is Welch's PSD estimate. Figure 4-15 shows the PSD estimate of a vibration signal using periodogram. Figure 4-16 shows the PSD estimate of the same signal using the Welch's method. The data is divided into four segments with 50% overlap between them. A Hamming window is used to compute the modified periodogram of each segment. By comparing Figure 4-15 and Figure 4-16, we can see that the averaging of modified periodograms tends to decrease the variance of the estimate relative to a single periodogram estimate of the entire data record. Although overlap between segments tends to introduce redundant information, this effect is diminished by the use of a nonrectangular window, which reduces the importance or weight given to the end samples of segments (the samples that overlap).

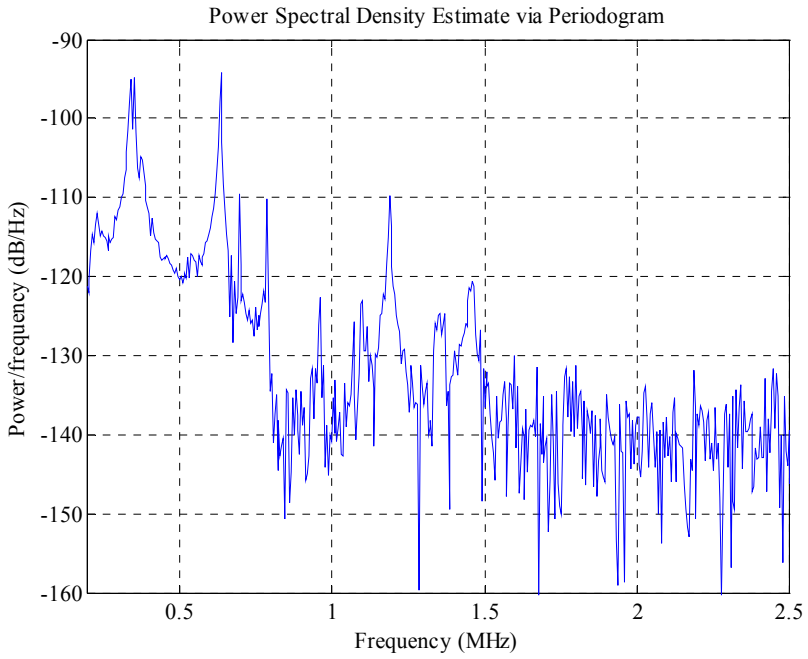

Figure 4-15: Power spectral density estimate via periodogram

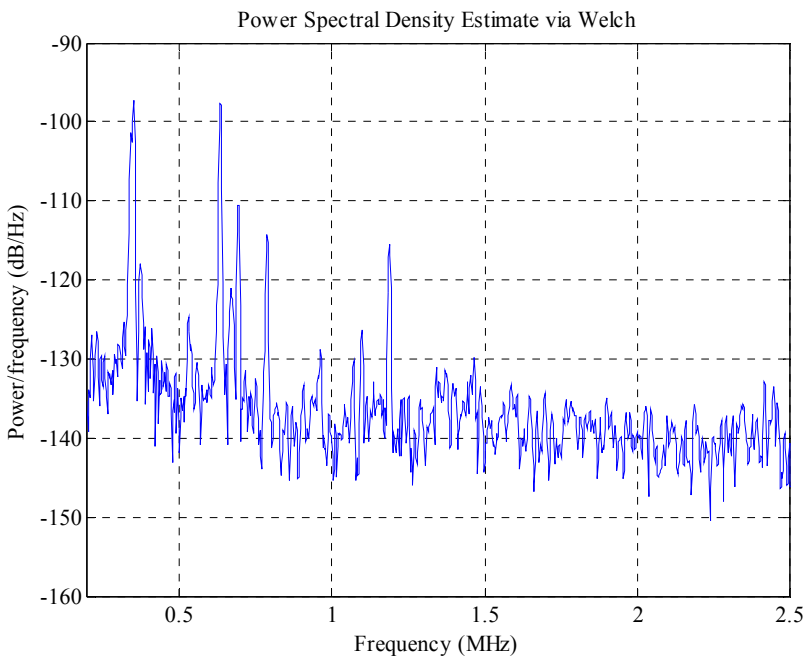

Figure 4-16: Power spectral density estimate of the same signal as in Figure 4-15 via Welch method

PSD Estimation via Thomson's Multi-Taper Method (MTM)

Thomson introduced the multi-taper approach to power spectral estimation in his seminal 1982 paper (Thompson, 1982), based on Slepian's orthogonal set of tapers (Slepian, 1978). The use of Slepian's tapers is optimal in the sense that the spectral concentration of the main lobe is maximized. This ensures a small spectral leakage. Instead of using band-pass filters that are essentially rectangular windows (as in the periodogram method), the MTM method uses a bank of optimal band-pass filters to compute the estimate. These optimal FIR filters are derived from a set of sequences known as discrete prolate spheroidal sequences (DPSSs). In addition, the MTM method provides a time-bandwidth parameter with which to balance the variance and resolution. For each data set, there is usually a value for this time-bandwidth parameter that allows

an optimal trade-off between bias and variance. Figure 4-17 shows the PSD estimate of the same signal in previous section via the MTM method.

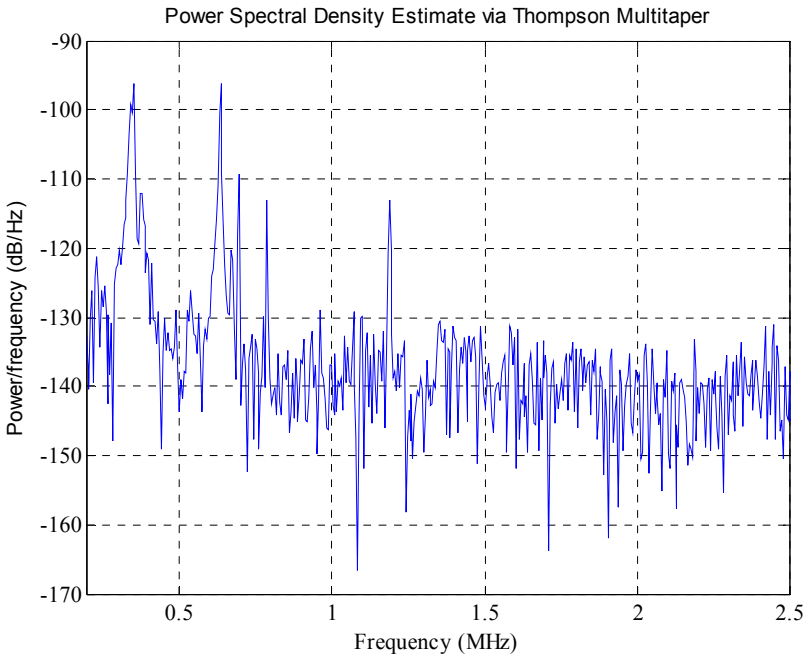

Figure 4-17: Power spectral density estimate of the same signal as in Figure 4-15 via multi-taper method

Parametric Methods

Parametric methods are those in which the PSD is estimated from a signal that is assumed to be the output of a linear system driven by white noise. Examples are the Yule-Walker autoregressive (AR) method and the Burg method. These methods estimate the PSD by first estimating the parameters (coefficients) of the linear system that hypothetically "generates" the signal. Parametric methods tend to produce better results than classical nonparametric methods when the data length of the available signal is relatively short.

Yule-Walker Method and Burg Method

The most commonly used linear system model is the all-pole model, a filter with all of its zeroes at the origin in the z-plane. The output of such a filter for white noise input is an autoregressive (AR) process. The AR methods tend to adequately describe spectra of data that is "peaky," that is, data whose PSD is large at certain frequencies. The data obtained in LUIS system has "peaky spectra" so that AR models are very useful. In addition, the AR models lead to a system of linear equations which are relatively simple to solve. Figure 4-18 shows the estimated PSD of the same signal previously discussed using the Yule-Walker AR method. The spectrum is much smoother than the periodogram since the AR methods assume a simple all-pole signal model. Figure 4-19 shows the resulting PSD of the same signal using the Burg method. The primary advantages of the Burg method are resolving closely spaced sinusoids in signals with low noise levels, and estimating short data records, in which case the PSD estimates are very close to the true values. In addition, the Burg method ensures a stable AR model and is computationally efficient. The Yule-Walker method and the Burg method generated very similar results in this case, with the Burg method showing a slightly better frequency resolution.

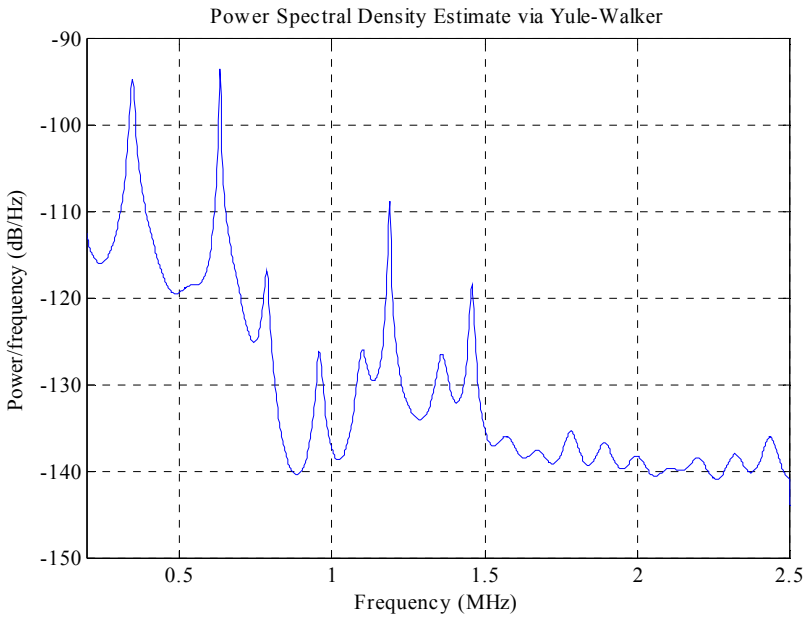

Figure 4-18: Power spectral density estimate of the same signal as in Figure 4-15 via Yule-Walker method

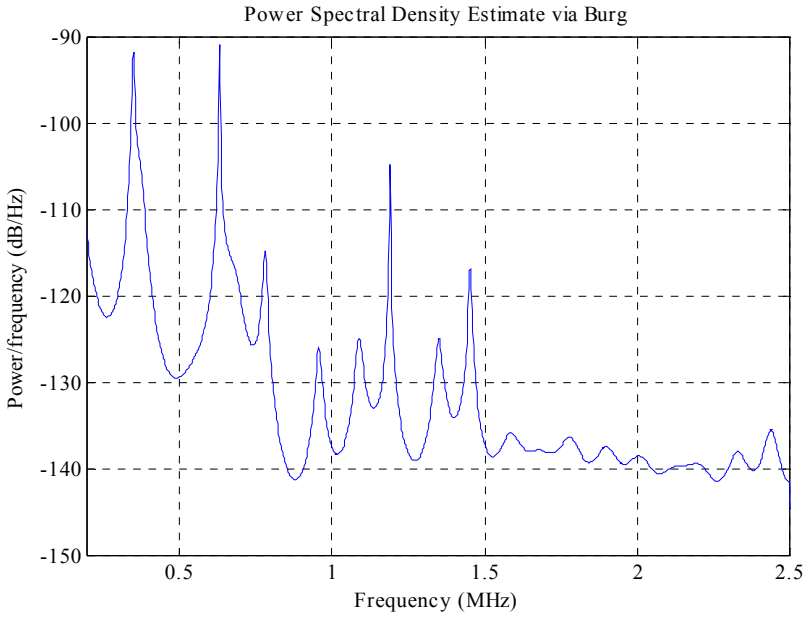

Figure 4-19: Power spectral density estimate of the same signal as in Figure 4-15 via Burg method

Subspace Methods

Subspace methods, also known as high-resolution methods or super-resolution methods, generate frequency component estimates for a signal based on an eigenanalysis or eigendecomposition of the correlation matrix. Examples are the multiple signal classification (MUSIC) method or the eigenvector (EV) method. These methods are best suited for line spectra, that is, spectra of sinusoidal signals, and are effective in the detection of sinusoids buried in noise, especially when the signal to noise ratios are low. Figure 4-20 and Figure 4-21 show the PSD estimates using the MUSIC method and the EV method, respectively. The spectra generated by the subspace methods more clearly show the dominating resonant frequencies buried in noises. The MUSIC result has a slightly better performance than the EV method in this case.

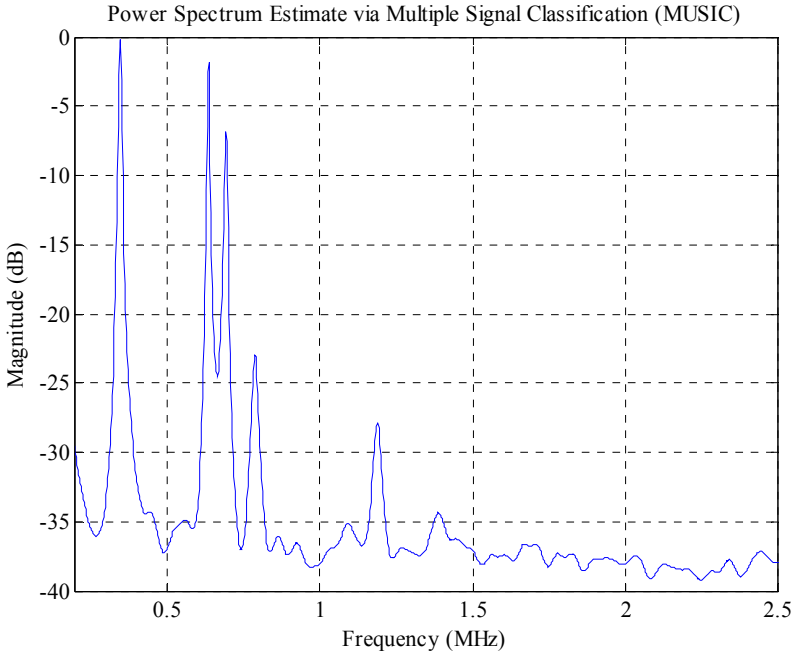

Figure 4-20: Power spectral density estimate of the same signal as in Figure 4-15 via MUSIC method

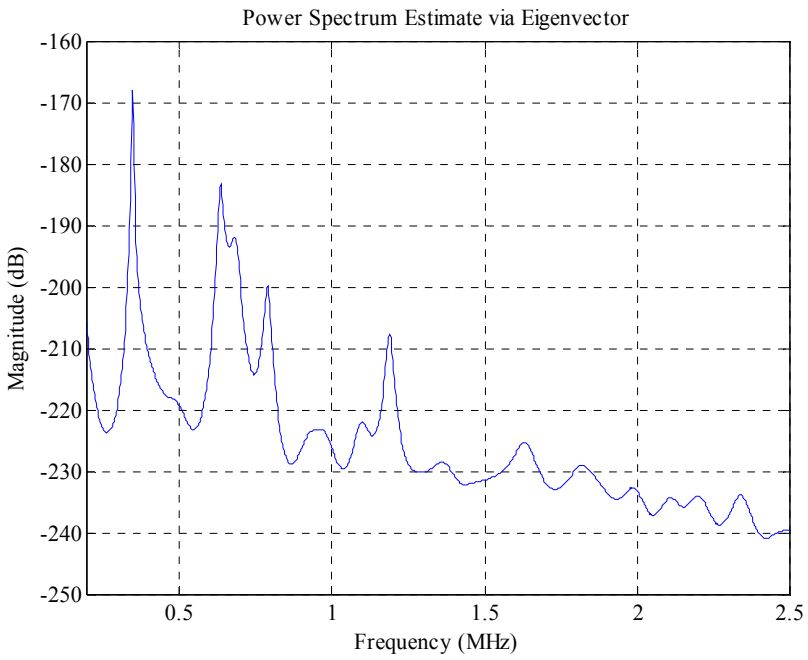

Figure 4-21: Power spectral density estimate of the same signal as in Figure 4-15 via EV method

The vibration responses measured using LUIS are a result of impact loading and with very short durations. The signals are non-stationary during the observation period. The non-parametric spectral estimation such as Periodogram and Welch's method will produce approximation errors since both methods assume stationary signals. For data sets of short duration, these conventional techniques become less reliable, and parametric (model based) spectral estimation such as Yule-Walker method has been proven to be advantageous in extracting high resolution frequency spectra from relatively short data sets. In summary, various signal processing methods are implemented to analyze the vibration signals detected by the LUIS system. Time-domain correlation coefficient and Auto-Comparison methods and frequency-domain spectral estimation methods help to establish the relationship between vibration responses and solder joint qualities. In Chapter 6, the vibration responses from a chip after different number of temperature

cycles are analyzed in detail using the above mentioned time-domain and frequency-domain methods. A Matlab program with graphical user interface (GUI) was written to facilitate these signal analysis methods. The user can load vibration signal data files, plot their vibration waveforms and power spectra, performing error ratio calculation, correlation coefficient analysis, and Auto-Comparison. All the analysis results are represented graphically. Figure 4-22 shows a screen capture of the Matlab GUI.

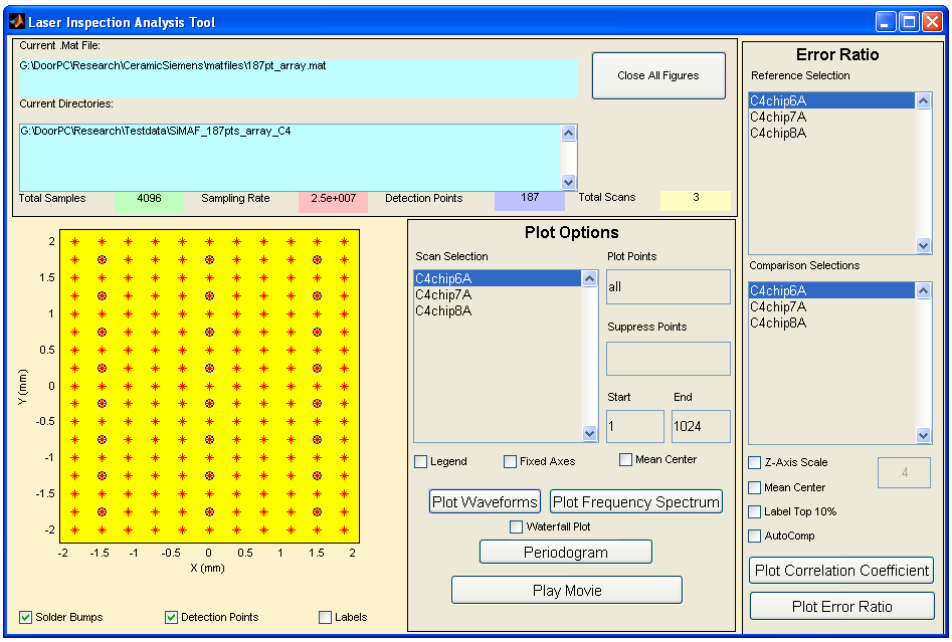

Figure 4-22: Screenshot of signal analysis program - SuperAnalysis Matlab GUI

CHAPTER 5

FINITE ELEMENT AND EXPERIMENTAL MODAL ANALYSIS

There are many discrete frequencies at which a structure will undergo vibration of large amplitude by sustained time varying forces of matching frequencies. These are said to be the natural or free vibration frequencies of that structure. It is also known that associated with each natural frequency is a distinct characteristic or mode shape which the structure acquires as it vibrates. In the LUIS system, a broadband laser pulse is used for dynamic excitation of the chip before its vibration signature is analyzed. Because only the out-of-plane vibration on chip's surface is of interest, and because the chip's length and width are much larger than its thickness, it can be simply modeled as a rectangular plate with pin supports. Analytical solutions to this over-simplified model do exist (Belvins, 1995), but for the complex geometry in the chip-solder joint-substrate assembly, analytical solutions for the vibration response are difficult to develop. Although attempts have been made to use the superposition method or the Ritz method to find analytical solutions for a vibrating plate (similar to an IC chip), the complex boundary conditions created by the high number of connections are a major roadblock in finding a closed-form solution (Gorman, 1982).

Modal analysis is a process whereby a structure is described in terms of its natural characteristics which are the frequency, damping and mode shapes. There are two ways to perform modal analysis nowadays – the experimental modal analysis (EMA) and the finite element analysis (FEA). These two methods are complimentary to each other. If an EMA and an FEA on the same structure both yield the same modes, then presumably

both must be accurately characterizing its structural dynamics. One should not be used to the exclusion of the other. Both tools are useful for gaining a better understanding of the dynamic behavior of physical structures, and in particular for simulating and ultimately solving resonant vibration problems (Mark, 2005). In this chapter, finite element modal analysis of several chip-to-substrate assemblies with and without defective solder joint connections are performed to disclose the effects of solder joint defects on the modal properties of the assemblies. The finite element models are then experimentally validated using the LUIS system.

Finite Element Modal Analysis of PB18 Flip Chip Assembly

The PB18 flip chip test die has 48 eutectic solder bumps evenly distributed along the four edges of the chip as shown in Figure 5-1. The chip size is 6.35 mm x 6.35 mm and the typical solder bump diameter is 190 μm with a bump pitch of 457 μm. The thickness of the die is about 0.65 mm.

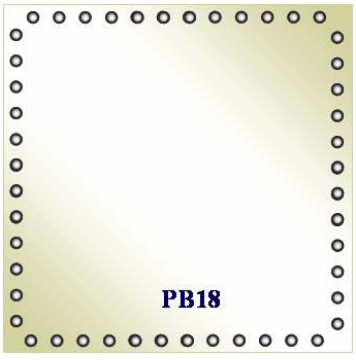

Figure 5-1: PB18 flip chip test die

When the flip chip is surface mounted onto a FR4 substrate, the whole assembly can be simplified as a square plate with pin support on the four edges. For this overly simplified model, the natural frequencies can be calculated by (Belvins, 1995):

$$F = \frac{\lambda^2}{2\pi a^2}\sqrt{\frac{Eh^3}{12\gamma(1-\nu^2)}} \tag{15}$$

where :

- λ^2 is a vector that is specific to the constraint conditions. For pin support on four edges, λ^2 = (35.99, 73.41, 108.3, 131.6)
- a is the length of the square plate and equals to 6.35 mm for PB18 flip chip
- E is Young's Modulus and equals to 110 GPa
- h is the thickness of the chip and equals to 0.65 mm
- ν is Poisson's Ratio and equals to 0.31
- γ equals to the product of μ and h, where μ is the density of silicon and equals to 2330 kg/m^3.

The calculation yields the following natural frequencies: 105.66 kHz, 264.14 kHz, 422.63 kHz and 528.29 kHz. This result can be used for a quick check for the assumptions used in the finite element analysis and experimental modal analysis.

Model Assumptions

Simplifying assumptions are made to allow for creation of the model within the limitations of the software package and the ability of the properties to be verified. The assumptions are listed below.

1. Silicon die is a homogeneous piece of silicon material.
2. The under bump metallurgy (UBM) material is inconsequential to the model, and the solder bump is directly attached to the chip.
3. The natural vibration frequencies of the chip are sufficiently higher than the vibration frequencies of the board to prevent coupling. Therefore, the model neglects the FR-4 board and assumes that the bottoms of the solder bumps are fixed in the X, Y, and Z directions.
4. All material properties are assumed to be linear. During a modal analysis, the software package ignores all nonlinearities.

These assumptions are valid for the model under consideration because the goal is not to exactly determine the thermal, fatigue, or electrical properties. The only goal is to determine the dynamic properties, and to represent the overall characteristics of the device. These simplifications of the model allow for fine meshing parameters and a reasonable solution time.

The ANSYS APDL code for the analysis is listed in Appendix C.

Geometric Modeling and Material Properties

The geometric modeling of the PB18 flip chip test die is straightforward with the simplification assumptions mentioned above. The silicon die is a homogeneous silicon

plate. The UBM is ignored in the model due to its inconsequential role in modal behavior. The solder bumps are modeled as a spherical shape flattened at the top and the bottom. The dimensions are listed in Table 5-1 and Figure 5-2 shows the geometric model of the test die and the solder bump.

Table 5-1: PB18 geometric dimensions

Die Length	6.35 mm	Die Thickness	0.65 mm
Die Width	6.35 mm	Bump Diameter	0.19 mm
Bump Pitch	0.457 mm	Bump height	0.14 mm

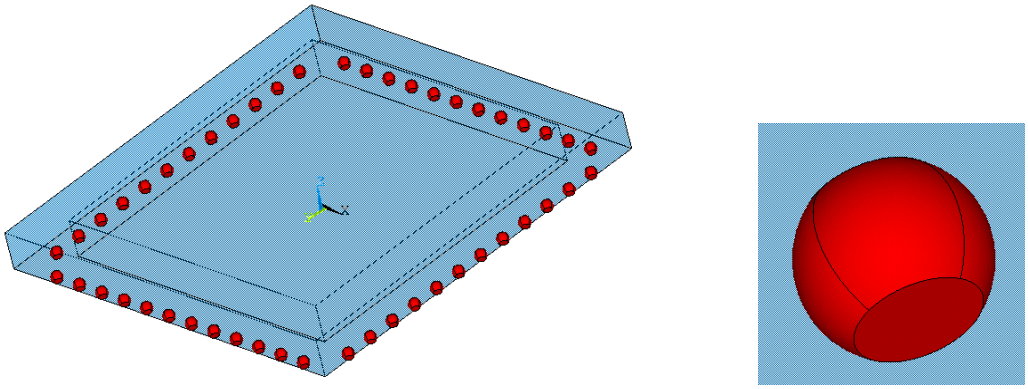

Figure 5-2: Geometric model of a PB18 test die and a solder bump

The material properties required for a modal analysis are: density (ρ), Young's modulus (E) and Poisson's ratio (ν). Material property values used in this model are listed in Table 5-2.

Table 5-2: Material properties used in finite element model

	Silicon	Eutectic Solder
Density (ρ) (kg/m^3)	2329	8400
Young's Modulus (E) (GPa)	112.4	32
Poisson's Ratio (ν)	0.28	0.38

Meshing and Boundary Conditions

A number of element types were chosen to mesh the structure. First, a PLANE2 element was used to area mesh the top surface of the solder bump, so that meshing of the solder bumps can be swept based off the area mesh. This area mesh also defines the interface between the die and the solder bump. As shown in Figure 5-3, PLANE2 element is a 6-node triangular element that has a quadratic displacement behavior and is well suited to model irregular meshes. The element is defined by six nodes having two degrees of freedom at each node: translations in the nodal x and y directions. The area meshing only helps to control the meshing of the solder bumps and the silicon die. The PLANE2 elements will be removed after meshing the die and the solder bumps and before calculating the modal solutions.

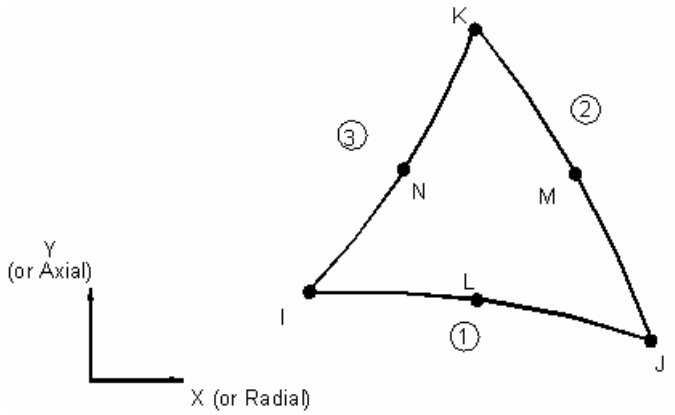

Figure 5-3: PLANE2 2-D 6-node triangular structural solid (Source: ANSYS User Manual)

The meshing of the solder bumps uses SOLID45 brick element. As shown in Figure 5-4, SOLID45 is defined by eight nodes having three degrees of freedom at each node: translations in the nodal x, y, and z directions. The prism option is used to match the PLANE2 area mesh and the SOLID92 tetrahedral elements in the silicon die.

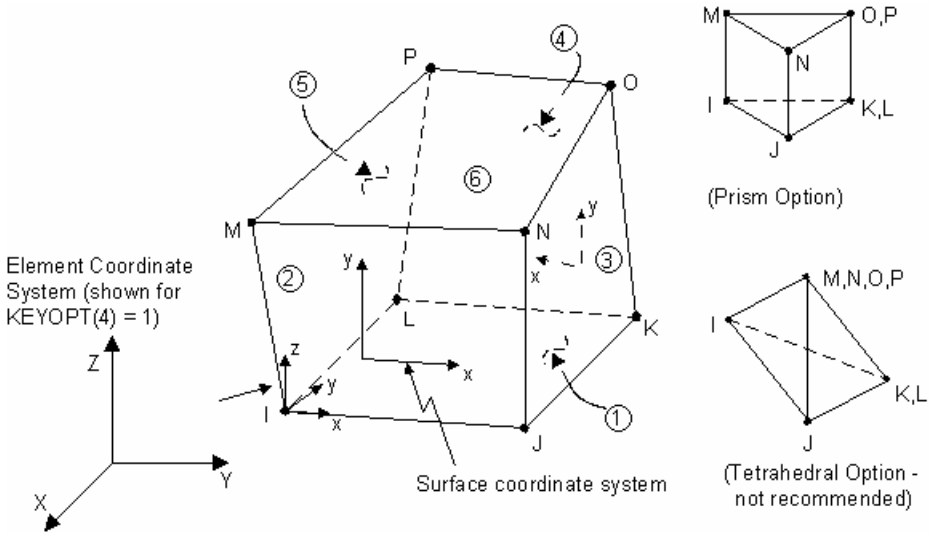

Figure 5-4: SOLID45 3-D structural solid (Source: ANSYS User Manual)

Finally, the silicon die is meshed with SOLID92, a 10-node tetrahedral structural solid element. The element has a quadratic displacement behavior and is well suited to model irregular meshes. As shown in Figure 5-5, the element is defined by ten nodes having three degrees of freedom at each node: translations in the nodal x, y, and z directions.

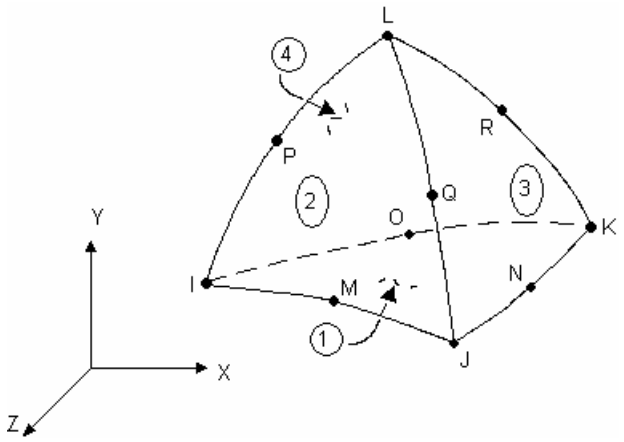

Figure 5-5:3-D 10-node tetrahedral structural solid (Source: ANSYS User Manual)

To control the element number, line segments were defined in the geometrical model before meshing. By adjusting the length of the line segments, the number of the total meshed elements can be easily controlled. Figure 5-6 shows the meshed model of the PB18 flip chip. The blue colored plate is the silicon die, and the red balls are the meshed solder bumps.

Modal analysis assumes a free vibration state and requires no force input. The boundary condition is only the displacement constraints on the bottom surface of the 48 solder balls. During the testing process, it is assumed that the PCB does not move, therefore it is assumed that there is no displacement on the bottom surface of all solder

balls. Open solder joint defects can be simulated by changing the boundary conditions as well.

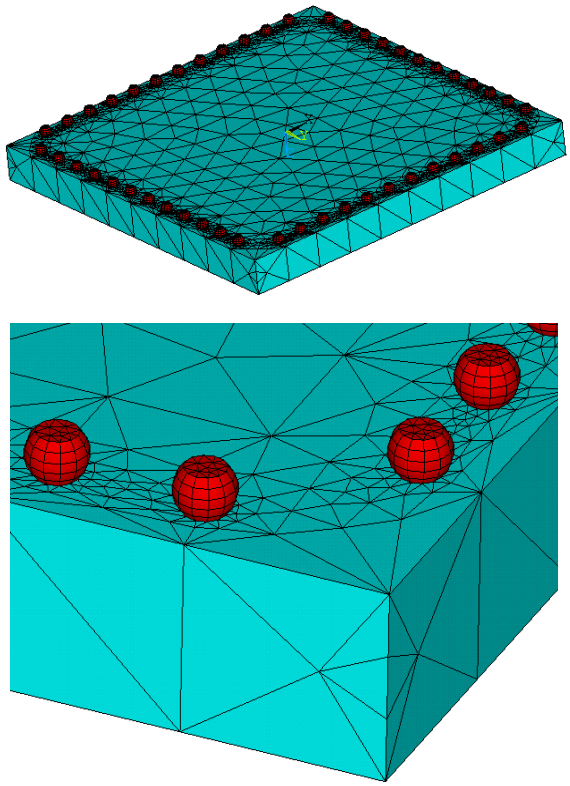

Figure 5-6: Meshed model of PB18 flip chip.

Solution

The Block Lanczos modal analysis solver that accompanying the finite element package is used to solve the modal parameters. This solver finds the natural vibration modes for an object based on geometry, mass distribution and material properties that provide parameters for the stiffness matrix for the structure. The solution process is automated, and the first 160 modes are extracted using the Block Lanczos mode extraction method. The solver provides a mathematical solution, calculating modes in all

six degrees of freedom. However, the laser interferometer measurement only allows detection of modes that have strong vibration response in the direction normal to the chip surface. Therefore, only those modes that are prominent in this direction can be compared to the experimental results.

Convergence Study

Mode frequency and mode shape are the two major results expected from the modal analysis. Therefore, the mode frequencies of an initial coarse model and a refined model are used to determine the convergence of the finite element modal. The refined model is obtained by changing the length of the line element size during geometrical modeling, thus control the number of meshed elements.

The initial and refined meshing are shown in Figure 5-7 and Figure 5-8, respectively. The initial meshing has 110 elements for each solder bump and a total of 14255 elements for the whole assembly. The refined meshing results in 496 elements in each solder bump and a total of 50798 elements for the whole assembly.

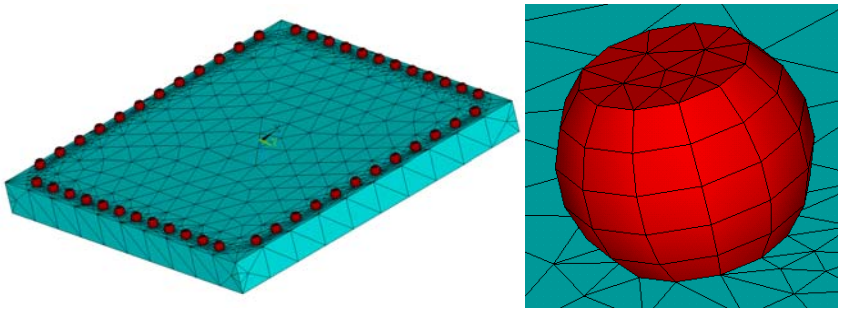

Figure 5-7: Initial meshing of PB18 flip chip

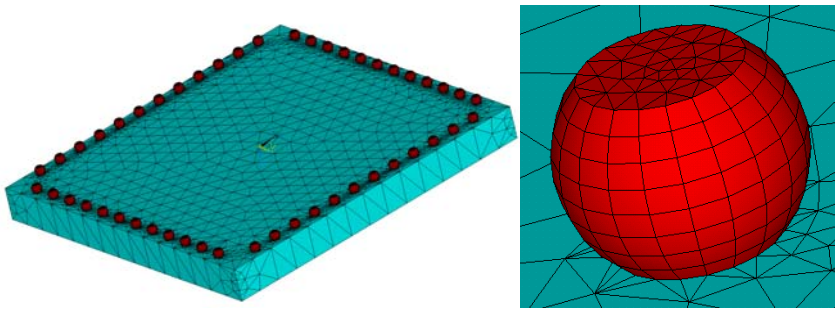

Figure 5-8: Refined meshing of PB18 flip chip

The mode frequency results of both the initial model and the refined model are listed in Table 5-3. The percent differences between the refined model and the initial model are listed in the last column. For the top nine most significant modes, the percent difference in the mode frequencies ranges from 0.82% to 2.59%, which all meet the 5-10% difference requirement and indicating a converged solution.

Table 5-3: Mode frequencies of initial model and the refined model

Modes	Mode Frequencies (Hz)		% Difference
	Initial Model	Refined Model	
1	104483	103371	1.06%
2	384826	378863	1.55%
3	628090	621800	1.00%
4	651547	646225	0.82%
5	480484	473429	1.47%
6	750837	736348	1.93%
7	1162080	1132200	2.57%
8	1113880	1085060	2.59%
9	1285180	1251830	2.59%

Results

A total of 160 modes are extracted using Block Lanczos method. Since the modal result contains all six degrees of freedom, the modes of interest, i.e. those out-of-plane displacement modes that have high participation factors are considered according to their significance level. The mode frequencies along with their participation factor ratios of a good (defect-free) PB18 flip chip are plotted in Figure 5-9. The vertical axis represents each mode's participation factor ratio. The most dominant mode has a mode frequency of about 104 kHz, which is very close to the previous analytical solution of an over simplified plate-with-pin-support model, which gives a mode frequency of 105.66 kHz. This close match indicates that both the simplified model and the finite element modal model are reasonable approximations of the dynamic behaviors of the actual PB18 flip chip assembly. Most of the dominant modes are located in the 100 kHz to 1 MHz frequency range. This assures us that we are not missing any significant modes by using a 2 MHz low-pass filter in the interferometer when acquiring the ultrasonic displacement signal.

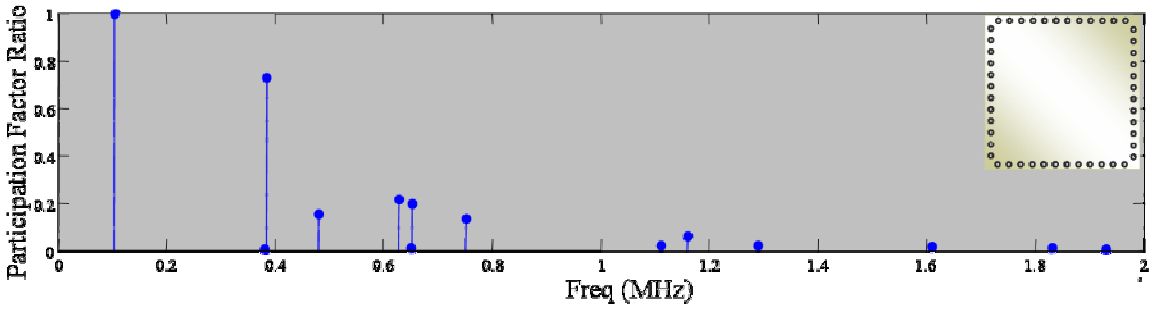

Figure 5-9: Modeling result: dominant frequencies for a good PB18 flip chip

To study the effects of defects on modal parameters, PB18 flip chips with different numbers of missing bumps at different locations are also modeled. Figure 5-10 shows the modeling result of a PB18 flip chip with one missing bump at the lower left corner. The result is very similar to the defect-free flip chip plotted in Figure 5-9. Differing from previous modeling result on a 14 bump flip chip assembly which reported a discernable frequency shift, there is no significant frequency shift observed when comparing the mode frequencies of the PB18 flip chip with one missing bump to a good PB18 flip chip. This indicates that mode frequency shifting will become smaller with increasing number of solder joint connections, and will become indiscernible when the number of solder joints reaches to a certain level. But there are a few modes that are not present in the model of the good flip chip show up in the model of chip with one missing bump, with the most prominent one located around 400 kHz in Figure 5-10.

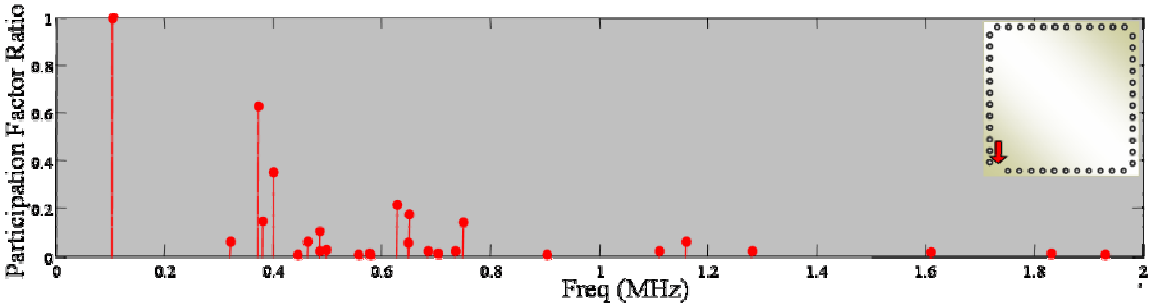

Figure 5-10: Modeling result: dominant frequencies of a chip with one missing bump at the corner

The mode shape may disclose the differences in modal parameters between a good flip chip model and a defective flip chip more clearly. Figure 5-11 shows the 12 most significant out-of-plane deflection modes of a good PB18 flip chip. Both the mode

frequencies and the mode shapes are presented. The result of such a flip chip with one missing bump at the lower left corner is plotted in Figure 5-12. For the first mode, the dominant frequency changes from 104.48 kHz in the good chip to 104.34 kHz in the bad chip. The natural frequency decrease indicates weaker solder joint connection which is reasonable with one bump missing. Unfortunately, the frequency shift is too small (merely 0.14 kHz) to be detected by the LUIS system.

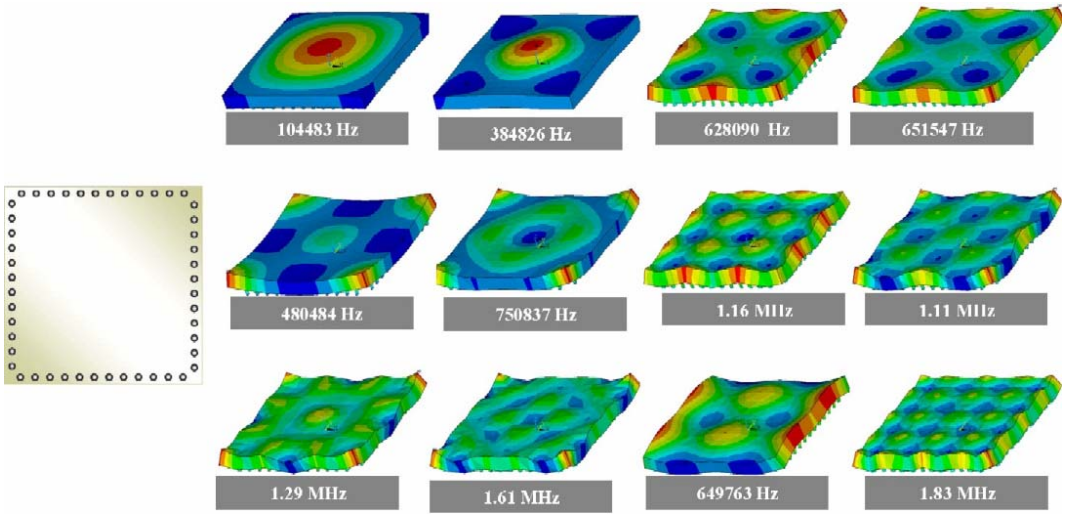

Figure 5-11: Mode frequencies and mode shapes of the 12 most significant modes of a defect-free PB18 flip chip

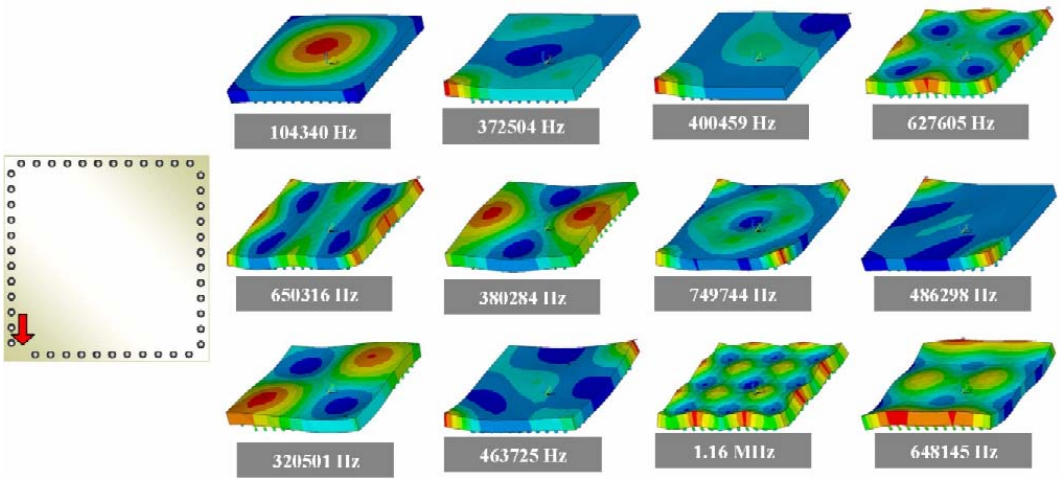

Figure 5-12: Mode frequencies and mode shapes of the 12 most significant modes of a PB18 flip chip with one missing bump at the lower left corner

Even though the frequency shift is minute, there are new modes that have unique mode shapes and can by easily identified. In Figure 5-12, the second mode (372 kHz) and the third mode (400 kHz) are two unique modes that appear in the flip chip with one missing bump at the lower left corner. The mode shapes are also very indicative of the missing bump location. Most of the modes that are present in the good chip model do exist in the defective chip model as well, except that their participation factors and mode frequencies have slightly changed.

To verify these unique mode shapes are defect specific, different defective models are constructed and the results are plotted in Figure 5-13 through Figure 5-15. In Figure 5-13, the missing bump location moved from the lower left corner to the bump location next to it. Again, a slight frequency shift is observed and more unique modes appear. The second mode (377 kHz) and third mode (381 kHz) have unique shapes that are present in neither the good chip nor the chip with one missing bump at the lower left corner. For a chip with two missing bumps at the corner as shown in the contour mode shape plots in

Figure 5-14, the dominant frequency decreases further. There are also unique mode shapes that are present in neither the good chip nor the chip with one missing bump at the corner. This indicates both the number and the location of the solder joint defects will affect the mode shapes. In Figure 5-15, a flip chip with two missing bumps located in the middle of the lower edge shows an even lower dominant frequency (102 kHz) and unique mode shapes that are specific to this defective pattern.

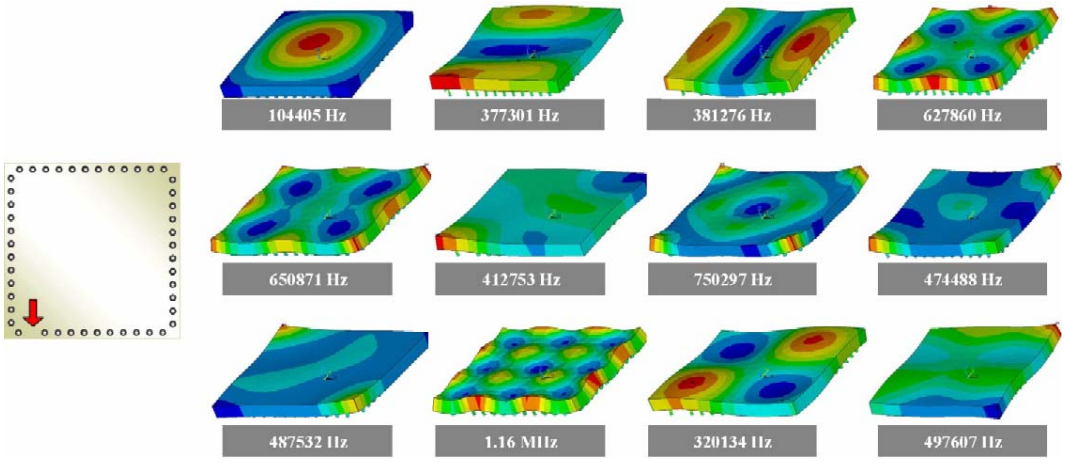

Figure 5-13: Mode frequencies and mode shapes of the 12 most significant modes of a PB18 flip chip with one missing bump next to the lower left corner

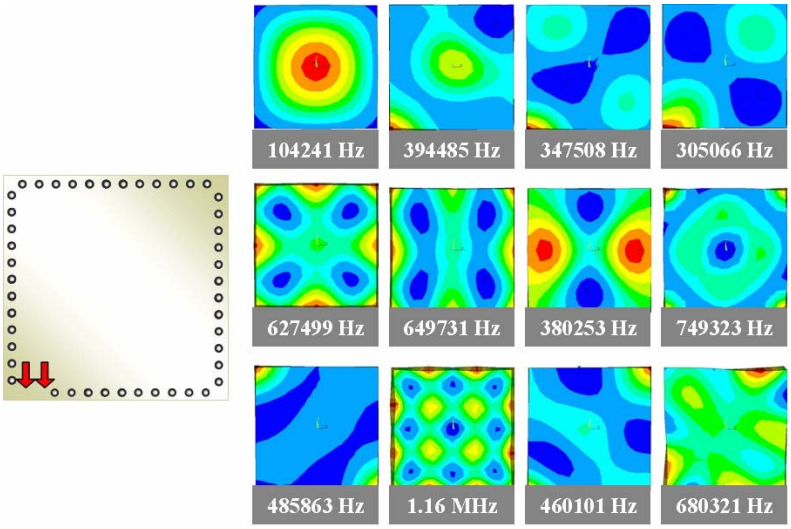

Figure 5-14: Mode frequencies and mode shapes of the 12 most significant modes of a PB18 flip chip with two missing bump at the lower left corner

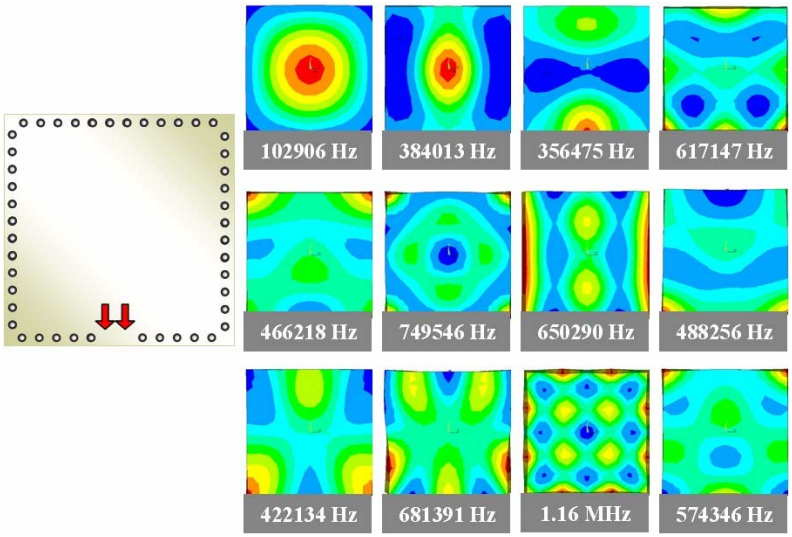

Figure 5-15: Mode frequencies and mode shapes of the 12 most significant modes of a PB18 flip chip with two missing bump at the center of the bottom edge

Experimental Modal Analysis of PB18 Flip Chip Assembly

Experimental modal analysis of the same PB18 flip chip as previously modeled was performed to validate the finite element modal model. Since the LUIS uses a pulse

laser to excite the chip assembly into structural vibration, and since the duration of the laser pulse is very short (4~5 nanoseconds.), the excitation can be approximated as an impulsive force, thus the structural vibration approximates the assembly's impulse response. Power spectra of the vibration signals can be directly used to extract the mode frequencies of the chip assembly. To obtain a full field vibrational pattern, LUIS is used to perform a raster scan of the chip surface using the inspection pattern depicted in Figure 4-7. The 14 x 14 inspection point array covers the whole chip surface and gives a relatively fine spatial resolution (with a pitch of 0.457 mm). The power spectra of the 196 measurements are superimposed to obtain the dominant frequencies. For each identified dominant frequency, a band-pass filter is designed to filter the vibration signal in that frequency region. The filtered data are plotted in the time domain to form the vibrational pattern in that dominant frequency. The resulting vibrational pattern is thus the "pseudo mode shape" of that specific mode. Using this approach, 8 dominant modes were identified and their constructed mode shapes and corresponding band-pass filters are plotted and listed in Figure 5-16 and Figure 5-17. The corresponding mode shapes and mode frequencies from the finite element model are also plotted and listed. We can see a very close match between the mode frequencies and the band-pass filter pass-bands, as well as between the finite element mode shapes and the experimentally obtained pseudo mode shapes. This result not only validates the finite element model, it also verifies that the vibrational signals measured by the LUIS system are indeed representative of the structural vibration of the chip-solder joint-substrate assembly. As a result, the LUIS system can be used to study the structural change of flip chip assemblies and the finite

element model can be exploited to simulate different kinds of electronics packages and defects.

Model	Experimental Result
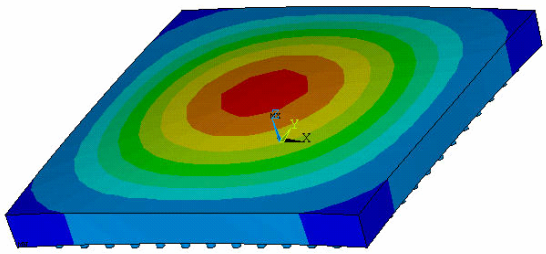	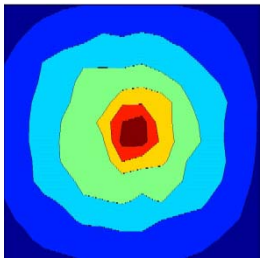
Mode Frequency: 104 kHz	Band-pass Filter Pass-band: 95 kHz – 115 kHz
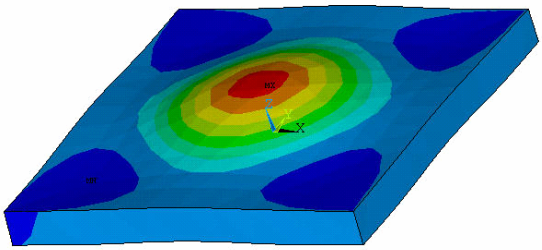	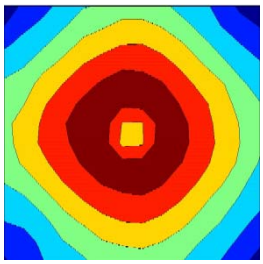
Mode Frequency: 385 kHz	Band-pass Filter Pass-band: 400 kHz – 430 kHz
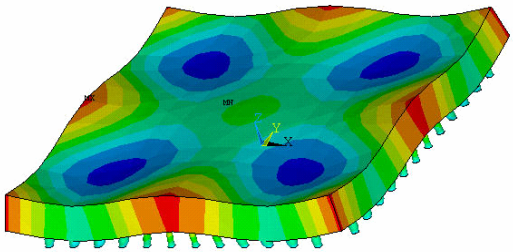	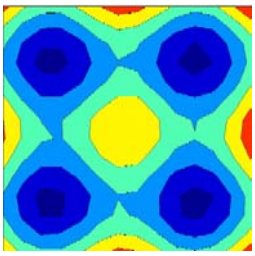
Mode Frequency: 628 kHz	Band-pass Filter Pass-band: 650 kHz – 680 kHz
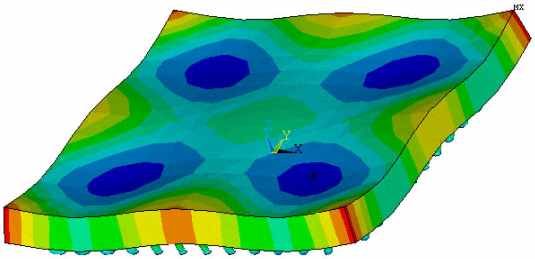	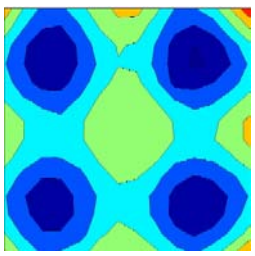
Mode Frequency: 652 kHz	Band-pass Filter Pass-band: 705 kHz – 725 kHz

Figure 5-16: Finite element modal analysis result and experimental result - Part I

Model	Experimental Result
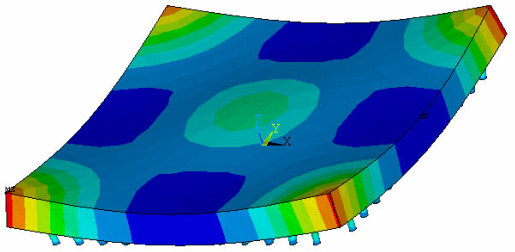	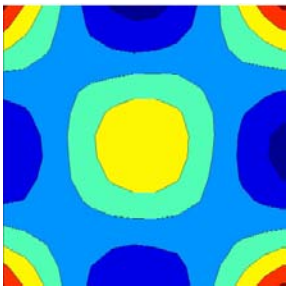
Mode Frequency: 480 kHz	Band-pass Filter Pass-band: 500 kHz – 550 kHz
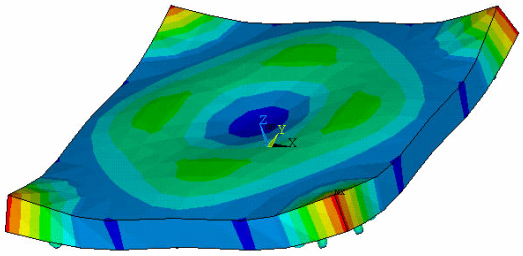	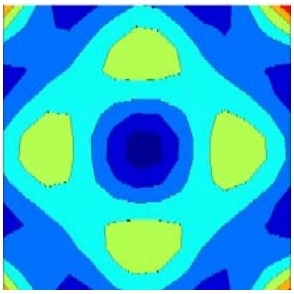
Mode Frequency: 751 kHz	Band-pass Filter Pass-band: 780 kHz – 820 kHz
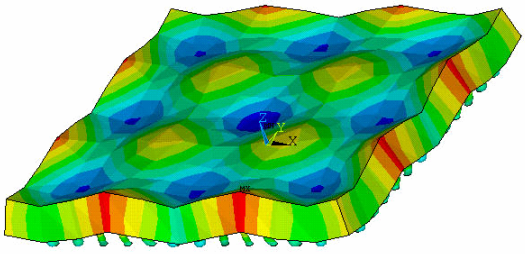	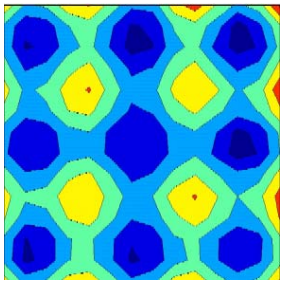
Mode Frequency: 1.16 MHz	Band-pass Filter Pass-band: 1.32 MHz – 1.38 MHz
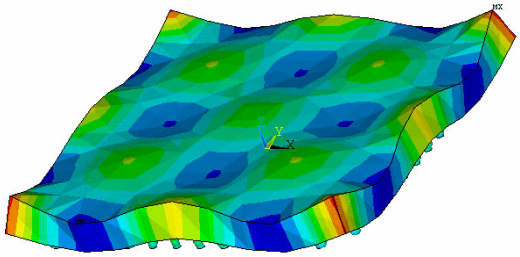	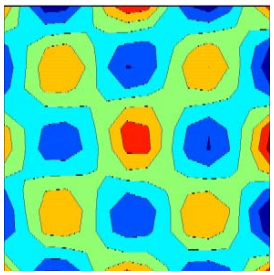
Mode Frequency: 1.11 MHz	Band-pass Filter Pass-band: 1.1 MHz – 1.3 MHz

Figure 5-17: Finite element modal analysis result and experimental result - Part II

CHAPTER 6

DETECTION OF SOLDER JOINT CRACKS IN A FLIP CHIP ASSEMBLY

Introduction to Solder Joint Crack Inspection

Solder joints with cracks often have intermittent connections and they often can pass functional test or in-circuit test, but will cause problems in the field. Flip chip solder joints are hidden from direct view and are hard to access with automated optical inspection equipment. Among the many techniques being used for solder joint inspection, automated X-ray inspection (AXI) and acoustic microscopy imaging (AMI) are the two widely used techniques in industry for hidden solder joint inspection. However, both of them have difficulties in detecting solder joint cracks (O'Conchuir et al, 1991). Both AMI and AXI are able to generate penetrative images, but both methods have difficulties in imaging cracks, especially cracks in the direction perpendicular to the imaging plane. X-ray laminography is capable of identifying defects in virtually any direction but is not suitable for in-line inspection because of its slow throughput and the complicated image interpretation algorithms necessary to evaluate data. In addition, both AMI and AXI systems usually have high operation and equipment costs.

This chapter discusses the LUIS system's capability in detecting solder joint cracks in a flip chip assembly. A systematic study of parameters such as error ratio, correlation coefficient, resonant frequency, electrical resistance, and the extension of solder joint cracks is performed to quantitatively characterize the relationships among

them. These relationships verify that the laser ultrasound inspection system provides a reliable and efficient way to evaluate flip chip solder joint cracks nondestructively.

In order to investigate the relationship between parameters such as error ratio, correlation coefficient, resonant frequency, electrical resistance, and the actual initiation and propagation of fatigue cracks, assembled flip chip samples were put through temperature cycling testing, and measurements were taken at different numbers of temperature cycles. These samples were also cross-sectioned afterwards to observe the extension of solder joint cracks at different fatigue stages.

Flip Chip Test Die

The flip chip used is a daisy chain flip chip test die (PB18). It has 48 eutectic solder bumps evenly distributed along the four edges of the chip. The chip size is 6.35 mm x 6.35 mm and the typical solder bump diameter is 190 μm with a bump pitch of 457 μm. The chips were surface mounted on to FR4 based printed wiring boards and reflowed without underfill. Each board has three such flip chips assembled. Figure 6-1 shows an assembled board, and the detailed drawing gives the locations of the solder bump and the laser excitation spot.

During an inspection, the excitation laser beam was projected onto the center of the chip surface at a 45° incident angle. The laser spot on the chip surface is indicated by the elliptical shape in Figure 6-1. The sample board is moved around by the X-Y motion stage so that the vibrometer beam is pointing to the desired inspection point. A total of 48 inspection points on the chip surface are chosen so that each of the 48 solder bumps has one inspection point right above it.

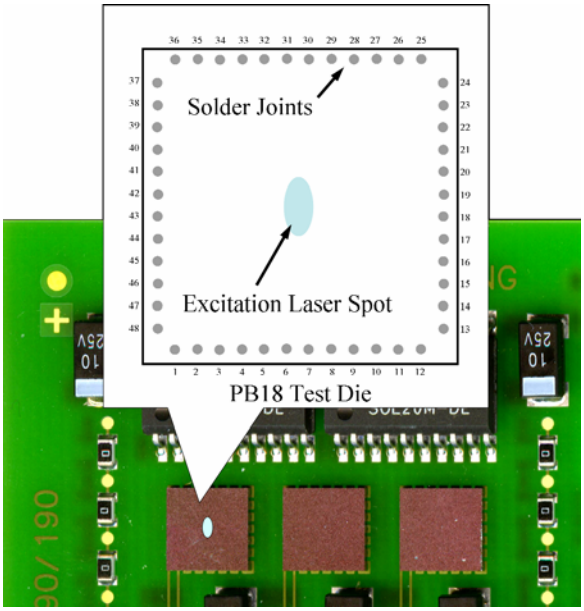

Figure 6-1: PB18 flip chip test die

Experimental Procedure

The experiments were performed in two phases. During phase I, one sample board assembled with three flip chips was used. First, the three flip chips were tested to ensure good electrical connections by measuring the total resistance of the daisy chains. Then, the vibration responses from the 48 inspection points from each of the three chips were recorded using the laser ultrasound inspection system. Then, the sample board was put through temperature cycling tests. After every ten temperature cycles, the board was taken out from the thermal chamber. Each of the three flip chips was measured for its total electrical resistance first, and then was measured by the laser ultrasound inspection system for its vibration responses. The temperature cycling test followed the conditions specified in JEDEC standard JESD22-A104-B (JEDEC, 2000), using test condition G with a nominal temperature range from -40 ˚C to 125 ˚C, soak mode No. 4 (minimum 15

minutes soak time at both maximum and minimum soak temperatures), and a once cycle per hour cycle rate. The phase I experiments terminated after 100 temperature cycles.

The second phase of the experiments used ten different sample boards. Flip chips on each board were measured for electrical resistances and inspected for vibration responses before temperature cycling. Then, each board was put through different numbers of temperature cycles, and was measured for resistances and vibration responses again after temperature cycling. The resistance measurement results obtained in phase I indicated that open connections occurred after 50 to 60 temperature cycles. Therefore, the ten sample boards used in phase II experienced different number of temperature cycles – instead of incrementing the number of cycles by 10 starting from zero and ending at 100 cycles, the number of cycles was incremented by five cycles starting from 45 cycles and ending at 65 cycles, in order to get more measurements when open connection is about to occur. After all the measurements were taken, the flip chips on the boards were cross sectioned to inspect solder joint cracks using scanning electron microscope (SEM). Since cross-sectioning is destructive, instead of the single board used in phase I, 10 sample boards were used in phase II so that SEM could be used to inspect cracks in solder joint connections at many different number of temperature cycles.

Phase I Experiment Result

Resistance Measurement Result

Table 6-1 shows the resistance measurement results of the three flip chips on the sample board after different number of temperature cycles. The resistances increased initially as the number of temperature cycles increased, followed by steep increases of the

resistances, indicating a broken connection(s) has occurred somewhere along the daisy chain. The three specimens showed steep increases in resistances after 50 (chip 1), 60 (chip 3), and 70 (chip 2) cycles respectively. Although the change of the electrical resistance values did not give much detail about the degradation of the solder joint integrity during temperature cycling, it did give a rough indication on when a through fatigue crack formed. For examples, from the results listed in Table 6-1, the open connection thus the through crack occurred in chip 3 after about 60 temperature cycles, and the initiation and formation of a partial crack must have occurred earlier than that. The rest of the discussions of this paper will use chip 3 as examples.

Table 6-1: Resistance values of three flip chips after different number of temperature cycles

Number of Cycles	Chip1 (Ω)	Chip2 (Ω)	Chip3 (Ω)
0	1.8	1.8	1.8
10	1.8	1.8	1.8
20	1.8	1.8	1.8
30	1.8	1.8	1.8
40	1.9	1.9	1.8
50	∞	1.9	1.8
60	∞	2.0	∞
70	∞	∞	∞
80	∞	∞	∞
90	∞	∞	∞
100	∞	∞	∞

Vibration Measurement Result – Time Domain Analysis

The vibration responses measured by the LUIS before temperature cycling were used as the references when calculating the error ratios and the correlation coefficients. For a single PB18 chip in Figure 6-1, each one of the 48 vibration responses measured from the 48 inspection points on the chip before temperature cycling was used as the reference signal and compared to the responses from the same location after each temperature cycle test. This gave 48 comparisons with either the ER or the correlation coefficient signal analysis method, for a single chip after a certain number of temperature cycles. The maxima, minima and averages of the 48 comparisons of chip 3 after different number of cycles were plotted in Figure 6-2. The correlation coefficient values at different cycles of chip 3 were plotted in Figure 6-2(a), and the corresponding error ratio values of the same chip were plotted in Figure 6-2(b). To make the two plots comparable, the vertical axis in Figure 6-2(a) uses a slightly modified correlation coefficient, 1-*r*. The range of 1-*r* is from 0 to 2, and the bigger the value, the greater the difference between the two signals being compared. The shaded areas in both figures represent regions where a through crack(s) has formed, since open electrical connection was detected after 60 cycles in chip 3. Partially cracked solder joints may cause a slight increase in electrical resistance but not an open electrical connection. Thus the cracks may have existed well before 60 cycles.

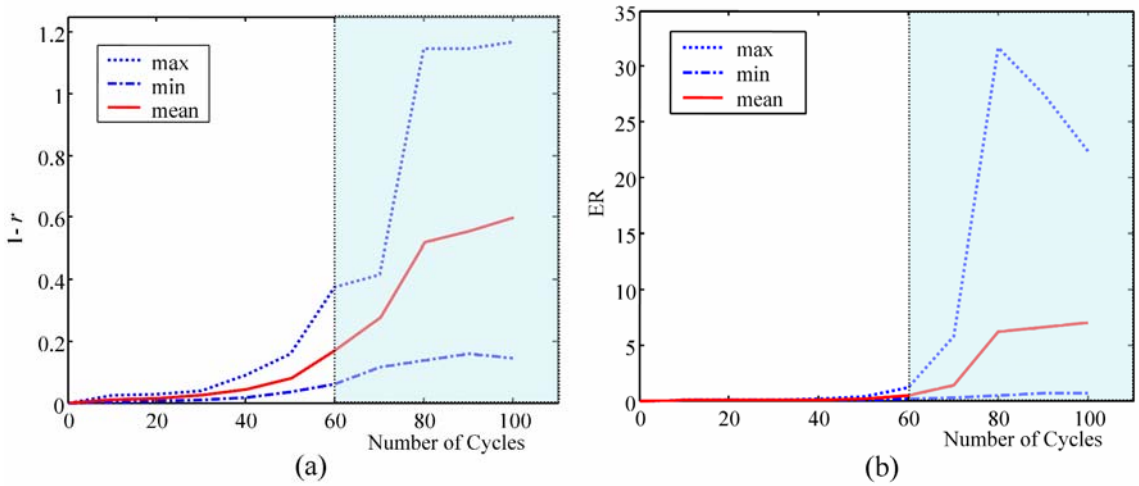

Figure 6-2: Laser ultrasound inspection results of flip chip 3 after different number of temperature cycles. (a) modified correlation coefficient results, (b) error ratio results.

The modified correlation coefficients increased after the first 10 cycles and kept increasing as the number of cycles increased. At 40 cycles, the average 1-*r* value was about 0.05 and the maximum was about 0.1. At this time, fatigue cracks might have initiated and started to grow, although open electrical connections have not been detected. At 60 cycles, when an open connection was measured the first time, the average 1-*r* value was about 0.2, and the maximum value reached 0.4. Comparisons between two reference (good) chips gave 1-*r* values below 0.01, thus the comparisons can clearly differentiate chips with good connections and chips with bad connections. The error ratios showed similar trends as the number of cycles increased. Because the error ratio values are not bounded by a limit, they can be as high as 30 (as the maximum error ratio at 80 cycles shown in Figure 6-2(b)) and lead to flat curves up to 60 cycles. In fact, the error ratio values start and keep increasing from the first 10 cycles. The curves up to the first 60 cycles appear to be flat is just because of the large error ratio value ranges.

Vibration Measurement Result – Frequency Domain Analysis

More insight was gained by looking at the vibration responses in the frequency domain. The laser pulse irradiation serves as an impulse input to the mass-spring system made up of the silicon chip and the solder joints, respectively. The broadband excitation from the impulse input causes the mechanical system to vibrate in many different modes. Resonances will occur at the mode frequencies of the whole system. Since the mode frequency of a mass-spring system only depends on the mass and the spring stiffness, when the integrity of the solder joints is compromised by fatigue cracks, the spring stiffness will decrease, causing the mode frequency to change. Figure 6-3(a) shows the power spectra of responses from point 17 on chip 3 before temperature cycling and after 20, 40, 60, 70 cycles. The frequencies corresponding to the peaks in the power spectra are the resonant frequencies. All five responses show highest power at around 100 kHz, indicating the fundamental frequencies of the responses. Resonant frequencies also appear at around 300 kHz, 400 kHz, 650 kHz, and 800 kHz. These resonances correspond to different vibration modes. In a certain mode, there is a shift of the mode frequencies when the number of temperature cycles changes. Figure 6-3(b) shows the details of the power spectra at the frequencies from 350 kHz to 500 kHz. The locations of the peak powers, i.e., the resonant frequencies vary with the number of temperature cycles. The resonant frequency is about 425 kHz before temperature cycling and decreases as the number of cycles goes up. After 70 cycles, the resonant frequency drops down to around 385 kHz. The resonant frequencies' decreasing trend is a good indication of the degradation of the solder joint connections with increasing number of temperature cycles.

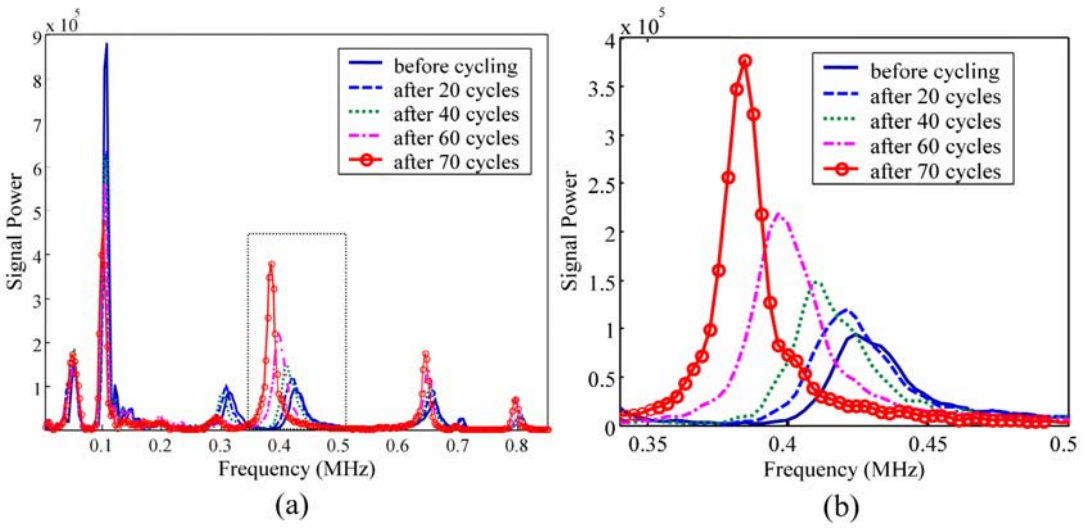

Figure 6-3: (a) Power spectra of the vibration signals collected from the same point on a flip chip after different number of temperature cycles. (b) Details showing the resonant frequencies (frequencies corresponding to the peak powers) at around 400 kHz decrease as the number of temperature cycles increase.

Figure 6-4 summarizes the changes of two resonant frequencies of the three flip chips at different number of cycles. Figure 6-4(a) shows the resonant frequencies of three chips that are in the 320 kHz to 440 kHz frequency band. The three resonances show a similar decreasing trend, starting from around 430 kHz before temperature cycling and decreasing to about 340 kHz after 100 cycles. Figure 6-4(b) shows another resonance of the three chips, which is in the 632 kHz to 680 kHz band. The resonances of the three chips are around 660 kHz before temperature cycling and decrease to around 640 kHz after 100 cycles. Similar trends were observed at other resonant frequencies as well. These curves verified that there is a strong correlation between the resonant frequencies and the number of temperature cycles and therefore the solder joint integrity. It was also noted that there is a variation of the resonances among the three flip chips at the same

stage of temperature cycling, but this variation is smaller than the changes of resonant frequencies incurred by fatigue cracks.

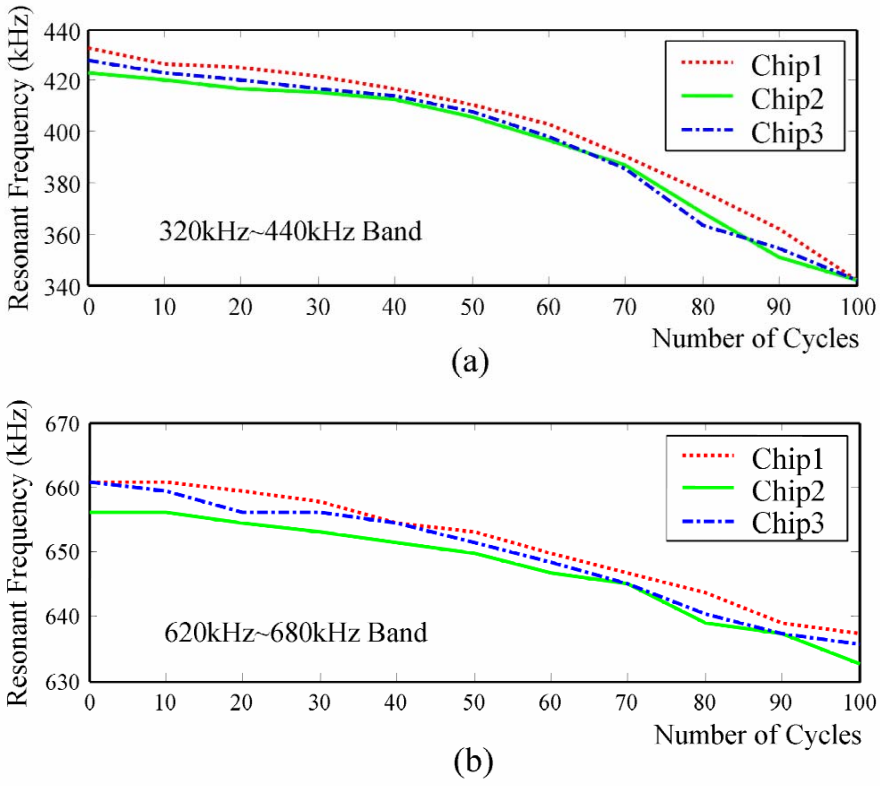

Figure 6-4: Resonant frequencies decrease with increasing number of temperature cycles: (a) shows the resonant frequency at the 320 kHz to 440 kHz band, and (b) shows another resonance at the 620 kHz to 680 kHz band.

Phase II Experiment Result

During phase II, each flip chip was measured for initial vibration response first, then, it was put through different number of temperature cycles and was measured for resistance and vibration response again after cycling. After that, the chip was cross-sectioned for observation of solder joint cracks using SEM. Since cross-sectioning is a

destructive test, a total of ten sample boards were used, each board has three flip chips assembled on it and was put to different number of cycles. During phase II, the number of temperature cycles between measurements was adjusted so that more measurements could be performed around 60 cycles since that was where open electrical connections were first detected in Phase I. The resistance measurement results of the 30 flip chips are summarized in Table 6-2. Open connections were found in chips that experienced 60 or more temperature cycles.

Table 6-2: Phase II resistance measurement result

Number of Cycles	Chip1 (Ω)	Chip2 (Ω)	Chip3 (Ω)
25	1.9	1.9	1.9
35	2.0	2.0	2.0
45	2.0	2.0	2.0
50	2.1	2.1	2.1
55	2.2	2.2	2.2
60	∞	∞	∞
65	∞	∞	∞
75	∞	∞	∞
90	∞	∞	∞
110	∞	∞	∞

Since the cross-section of a solder joint exposes only one plane at a time, the presence of cracks in the SEM images only tells what is happening in that specific plane. But these SEM images still give a rough indication of the extension of cracks in solder joints. According to the cross-sectional images, there were no cracks found in the solder joints from 25 to 35 temperature cycles. Cracks started to appear after 45 cycles with various dimensions, although resistance measurement results showed good electrical

connection up to this point. Almost all the cracks are located near the chip and solder interface. With increasing number of temperature cycles, the number and extension of fatigue cracks grow. Through cracks are common in solder joints which have experienced 70 or more cycles. Figure 6-5 shows SEM images of two solder joints after 70 temperature cycles. The solder joint in Figure 6-5(a) has a small crack near the edge, while the crack in Figure 6-5(b) almost propagated through the solder joint.

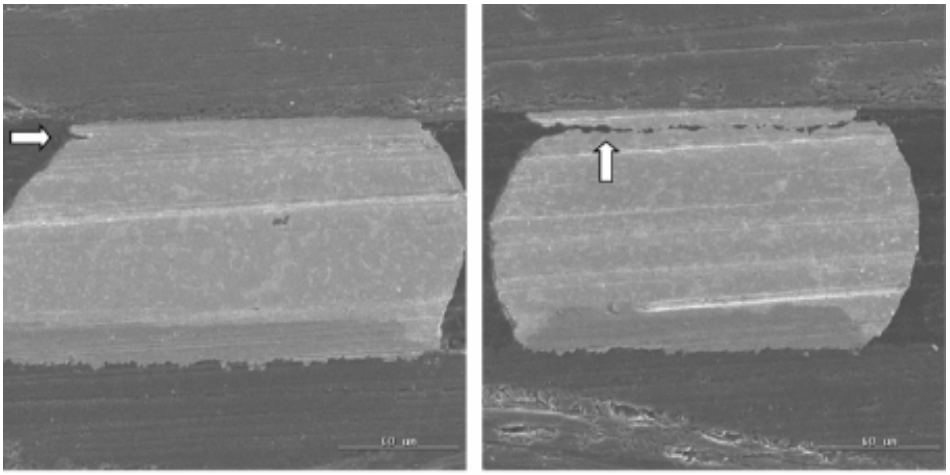

Figure 6-5: SEM images of two solder joints after 65 temperature cycles. (a) Shows a crack started near the chip-solder interface, and (b) shows a nearly through crack.

The correlation coefficient and error ratio results of the vibration responses obtained in phase II shown in Figure 6-6 display a similar trend to the result of phase I. Figure 6-6(a) shows the progression of the 1-*r* value at different number of cycles. After 45 cycles, when cracks started to appear in the SEM images, the average 1-*r* value is about 0.16, and the maximum reaches 0.36. Since the comparisons between two references usually have 1-*r* values lower than 0.01, the 1-*r* values can clearly differentiate

chips with fatigue cracks from reference ones. Again, the error ratios shown in Figure 6-6(b) display similar relationship, except that the error ratio values are unbounded.

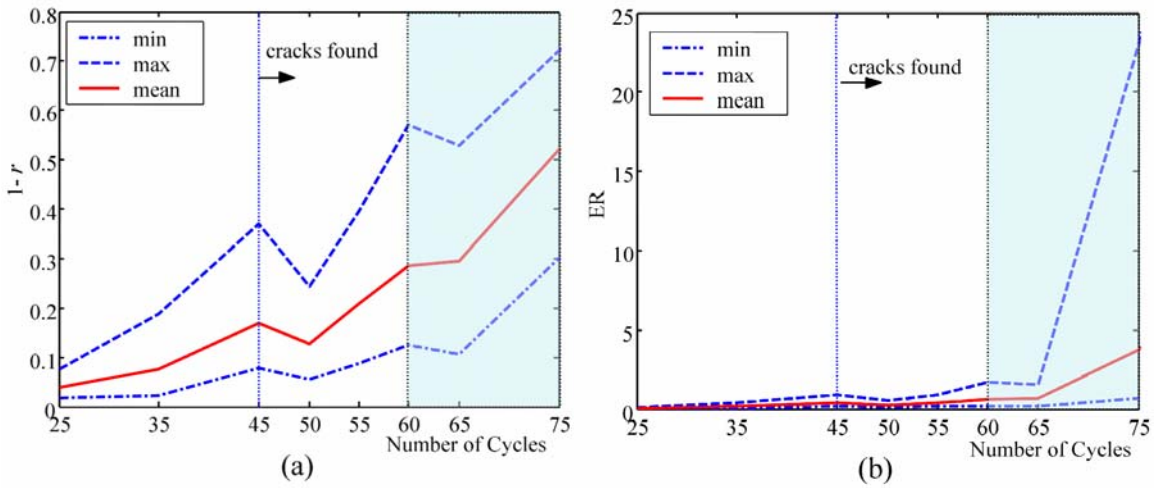

Figure 6-6: Phase II laser ultrasound inspection results. (a) Modified correlation coefficient results, (b) error ratio results.

Summary

The relationships among resonant frequencies of the vibration response, correlation coefficient comparisons, error ratio comparisons, resistance measurements, and the extension of solder joint cracks were studied for the range of temperature cycles performed. These relationships verified that thermal fatigue induced solder joint cracks can be evaluated by measuring the vibration response using the laser ultrasound inspection system. The vibration response can be analyzed in the time domain, using either correlation coefficient or error ratio method, or in the frequency domain, where resonant frequency at a certain frequency range decreases as the number of temperature cycles increases.

CHAPTER 7

CONCLUSION

Research Impact

Realization of the ultimate goal of this research will result in the development of a novel and automated non-contact, non-destructive, fast, sensitive, accurate and low cost solder bump quality inspection system. It is also expected to be applicable to many types of surface mount devices such as chip resistors and capacitors, and conventional lead frame packages, making it a versatile and cost-effective automated manufacturing tool. This tool could be used on-line as a go/no-go inspection tool, and off-line during process development for process optimization. Use of this new Laser Ultrasound-Interferometric inspection technology for automated manufacturing inspection will bring tremendous cost savings by catching defects early in the process. With access to rapid, accurate inspection systems, cost savings will also be realized in process development by reducing the time to market new products, and allowing better process optimization before manufacturing ramp-up.

Contribution

The LUIS solder joint inspection system was integrated and automated. System throughput and measurement repeatability was improved as a result of the integration and automation. The system measurement capability was characterized using measurement system analysis and gage repeatability and reproducibility study methods.

Correlation coefficient based analysis method was introduced to effectively identify solder joint defects. The implementation of correlation coefficient analysis methods increased defect detection sensitivity and efficiency of the system by providing higher signal-to-noise ratio as well as fast processing speed.

Auto-Comparison based analysis method was designed and developed to effectively identify solder joint defects while eliminating the reliance of a reference chip.

Spectral estimation based analysis methods were implemented to extract resonant frequencies in the frequency domain. The adoption of advanced spectral estimation algorithm to this system improved the accuracy in frequency domain analysis.

A finite element modal model of a flip chip assembly was constructed and validated. The model provides a tool to simulate and predict dynamical behaviors of any packages with solder joint defects and can be used as a virtual reference chip when using the comparison methods.

The system's capability in detecting solder joint fatigue cracks was studied by generating thermal fatigue cracks with temperature cycling followed by inspecting the solder joint cracks using the LUIS system.

Throughout this research, a variety of electronic packages of various representative defective types were studied. These include: flip chip assemblies, wafer-level chip scale packages, open solder joints, missing solder bumps, solder joint cracks, lead-bearing and lead-free solder joints, etc. These studies significantly extended the application scope of this system, making it a versatile inspection tool.

CHAPTER 8

RECOMMENDATIONS FOR FUTURE WORK

Alternative Ultrasound Generation Methods

Expanding Plasma Excitation

The pulsed laser direct excitation method currently being used will eventually run into a dilemma for some devices: at low energy density level, the ultrasound generation will fall into the thermoelastic regime, there will be no material ablation and the method can be considered as non-destructive. But the vibration induced at low energy density level is normally weak and stronger vibration is desired to have an admissible signal to noise ratio. Stronger vibration will be induced at higher energy density level, but oftentimes the energy density will be above the thermoelastic threshold, causing ablation, which is not acceptable for sensitive IC packages. This factor has limited the use of laser in ultrasonic generation because the possible damage to the surface of a sample. This damage can range from pitting or cracking the surface to the removal of a surface coating, which are unacceptable for sensitive electronic devices. Using optical fiber array (Yang et al, 1994) can alleviate the problem by exciting the chip to substrate structure at multiple locations, the superposition of the multiple excitations can cause stronger vibration and each excitation itself is still in the thermoelastic regime.

Dixon et al (1996) reported a technique that uses the plasma created by a focused pulsed laser beam to generate ultrasound without the sample actually being illuminated directly by the laser light. This is achieved by focusing a TEA CO_2 laser onto a dummy target, and allowing the plasma to expand away from the dummy target and to impact on

an experimental sample such that it generates ultrasound at the surface of that sample. Figure 8-1 shows one possible setup of ultrasound generation by expanding plasma. Other configurations can also be set up to allow the plasma to expand both around and over edges and through holes (Dixon et al, 1996). Plasma generation of ultrasound will provide stronger structural vibration without actually causing surface or subsurface damage to the sample.

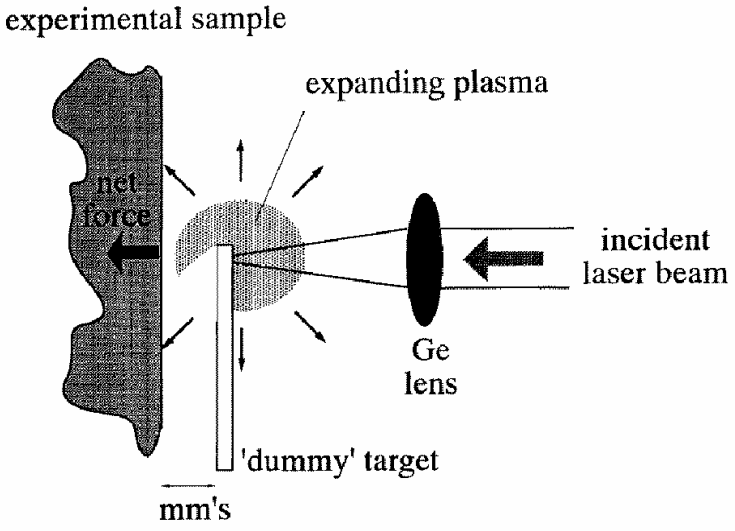

Figure 8-1: Schematic Diagram of one possible setup for plasma generation of ultrasound, where the laser is focused on a dummy plate and the plasma expands over the plate edge to impact on an experimental sample. (Courtesy of Dixon et al, 1996)

Scanning Laser Doppler Vibrometer

One of the major drawbacks of the current setup is the efficiency of the laser vibrometer. The single point detection setup will hold up the system throughput when the number of inspection points increases. Also, the sensor head has a relatively low light-collecting efficiency and the output signal is highly affected by the surface conditions.

Oftentimes the sensor head needs to be manually readjusted to get enough reflected light, preventing a fully automated inspection process without human intervention. Scanning laser vibrometer is already commercially available and can be adopted into this system to fully automated the inspection system and improve system throughput.

Signal Analysis Approach

The ultimate success of this project relies heavily on the interpretation of the measured vibration signals. Since the vibrational responses are not directly related to the presence, location, and dimension of the defects, advanced signal analysis methods are necessary to extract the useful information buried in the complex vibrational responses. The correlation coefficient analysis and spectral estimation methods introduced in this thesis work are effective with the samples that have been tested so far. For devices with higher I/O connection, finer pitch and complicated structure (stacked packages, for example), the vibrational response becomes more complicated and will be less and less directly related to the solder joint defects, posing a limit to these analysis methods. Advanced methods, such as wavelet analyses may be employed to gain better understanding of the responses.

Application Scope Expansion

The project started with a focus of inspection of flip chip solder joint defects for, along the way many other types of electronics components have been tested, including wafer-level chip scale package, multi-layer chip capacitors, thin-film resistors and some recent work on ball grid array packages. Various solder joint defect types such as missing

solder bumps, open solder joints, misaligned components, and solder joint cracks have been studied as well. To further expand the system's application scope, a multitude of package and defect types needs to be studied. These include but are not limited to: flip chip with higher I/O count, smaller bump size and finer bump pitch, flip chip with underfill, stacked dies, stacked packages, system-in-packages (SiP), etc. Beside the inspection of solder joints in electronics packages, another possible application of the current setup is the characterization of MEMS devices' dynamic behaviors, using the system's unique capability in measuring high-frequency nanometer-scale out-of-plane vibration signals. All these work will lead to a more versatile tool for defect inspection and failure analysis.

APPENDIX A

COORDINATE TRANSFORMATION MATLAB CODE

Matlab Code for Inspection Pattern Generation and Coordinate Transformation:

```
%%%%%%%%%%%%%%%%%%%%%%%%%%%%
% Object Finding Function %
%%%%%%%%%%%%%%%%%%%%%%%%%%%%

function index = FindObject(actual_xy, selected_xy)

for i = 1:size(selected_xy, 1)
    min = 1000;
    for j = 1:size(actual_xy, 1)
        distance = norm(actual_xy(j,:)-selected_xy(i,:));
        current_min = distance;
        if current_min < min,
            min = current_min;
            index(i) = j;
        end
    end
end



%%%%%%%%%%%%%%%%%%%%%%%%%%%%%%%%%%%%%%%%%%%%%%%%
% Machine Configuration/Calibration Data %
%%%%%%%%%%%%%%%%%%%%%%%%%%%%%%%%%%%%%%%%%%%%%%%%

FIXTURE_SIZE = [6*25.4, 8*25.4];        % units are millimeters
FIXTURE_HOME = [-25.77, 1.737];         % offset of fixture from CCD
base frame at home (mm)
FENCE_SIZE = [6*25.4, .375*25.4];       % units are millimeters
FENCE_OFFSET = [0 -4.1875*25.4];        % units are millimeters

CCD_SCALE = 134;                        % units are pixels per
millimeter
CCD_SIZE = [640 480];                   % units are pixels

P_INTER = [-252407,-38];                % units are microsteps in
[upper axis(x), lower axis(y)]
P_LASER = [108.880, 34.318];            % units are millimeters from
camera origin after homing stage and
                                            %positioning laser spot at
the origin of vision frame

STEPS2MM = 2.54/12800;                  % conversion from microsteps to
millimeters
```

```
%%%%%%%%%%%%%%%%%%%%%%%%%
% Patch Update Function %
%%%%%%%%%%%%%%%%%%%%%%%%%

function [Xdata, Ydata] = PatchUpdate(position, size)

x_vertex = size(1)/2;
y_vertex = size(2)/2;
Xdata = [position(1)-x_vertex, position(1)+x_vertex,
position(1)+x_vertex, position(1)-x_vertex]';
Ydata = [position(2)-y_vertex, position(2)-y_vertex,
position(2)+y_vertex, position(2)+y_vertex]';


%%%%%%%%%%%%%%%%%%%%%%%%%
% Patch Update 1 Function %
%%%%%%%%%%%%%%%%%%%%%%%%%

function [Xdata, Ydata] = PatchUpdate1(position, size)

x_vertex1 = size(1);
y_vertex1 = size(2);
Xdata = [position(1), x_vertex1+position(1), x_vertex1+position(1),
position(1)]';
Ydata = [position(2), position(2), y_vertex1+position(2),
y_vertex1+position(2)]';

%%%%%%%%%%%%%%%%%%%%%%%%%%%%
% Coordinate Transformation %
%%%%%%%%%%%%%%%%%%%%%%%%%%%%

function TRANSM =
RotAngCalc(fid1_view,fid1_measured,fid2_view,fid2_measured)

x1=fid1_view(1);
y1=fid1_view(2);
x1p=fid1_measured(1);
y1p=fid1_measured(2);

x2=fid2_view(1);
y2=fid2_view(2);
x2p=fid2_measured(1);
y2p=fid2_measured(2);

CTHETA=((x1-x2)*(x1p-x2p)+(y1-y2)*(y1p-y2p))/((x1-x2)^2+(y1-y2)^2);
STHETA=((x1-x2)*(y1p-y2p)-(y1-y2)*(x1p-x2p))/((x1-x2)^2+(y1-y2)^2);

THETA=atan(((x1-x2)*(y1p-y2p)-(y1-y2)*(x1p-x2p))/((x1-x2)*(x1p-
x2p)+(y1-y2)*(y1p-y2p)));

TRANSX1=x1p-x1*CTHETA+y1*STHETA;
TRANSY1=y1p-x1*STHETA-y1*CTHETA;
TRANSX2=x2p-x2*CTHETA+y2*STHETA;
TRANSY2=y2p-x2*STHETA-y2*CTHETA;
```

```
TRANSX=(TRANSX1+TRANSX2)/2;
TRANSY=(TRANSY1+TRANSY2)/2;

%x'=x*cos(theta)-y*sin(theta)+X
%y'=x*sin(theta)+y*cos(theta)+Y
TRANSM=[CTHETA,-STHETA,TRANSX;STHETA,CTHETA,TRANSY;0,0,1];

%%%%%%%%%%%%%%%%%%%%%%%%
% Board Draw Function %
%%%%%%%%%%%%%%%%%%%%%%%%

function [figure_handle, fid_xy, device_xy] =
BoardDrawFB250array(board_origin)

%%%%%%%%%%%%%%%%%%%%%%%%%%%%%%%
% load specimen/machine data %
%%%%%%%%%%%%%%%%%%%%%%%%%%%%%%%

FB250boardNSarray
MachineConfig

%%%%%%%%%%%%%%%%%%%%%%%%
% Create figure window %
%%%%%%%%%%%%%%%%%%%%%%%%

set(0,'Units', 'pixels')
position = [6 50 700 580];
figure_handle = figure('Color', [1 1 1], 'Position', position);
% plot the substrate outline
[sub_Xdata, sub_Ydata] = PatchUpdate1(board_origin, SUBSTRATE_SIZE);
patch('Xdata',sub_Xdata,'Ydata',sub_Ydata,'FaceColor',[.2 .8 .2],
'EdgeColor', 'none')
daspect([1,1,1])
hold on
axis off

% plot the board outlines
for j=1:2
for i=1:3
rectangle('position',[sub_Xdata(1)+(i-1)*SUBSTRATE_SIZE(1)/3,
sub_Ydata(1)+(j-1)*SUBSTRATE_SIZE(2)/2,...
        SUBSTRATE_SIZE(1)/3,SUBSTRATE_SIZE(2)/2],'EdgeColor','b');
end
end


% plot overall board fiducials
sub_fid_x = SUBSTRATE_FIDUCIAL_XY(:,1)+board_origin(1);
sub_fid_y = SUBSTRATE_FIDUCIAL_XY(:,2)+board_origin(2);
plot(sub_fid_x,sub_fid_y,'yo','MarkerSize',5,'MarkerFaceColor','y','era
semode','background')
daspect([1,1,1])
% plot all chip outlines
for i = 1:length(DEVICE_XY),
    [chip_Xdata(:,i), chip_Ydata(:,i)] =
PatchUpdate(DEVICE_XY(i,:)+board_origin, DEVICE_SIZE);
```

```
end
patch('Xdata',chip_Xdata,'Ydata',chip_Ydata,'FaceColor', [.7 .7 1], ...
    'EdgeColor','none','erasemode','background')
daspect([1,1,1])
text(DEVICE_XY(:,1)+board_origin(1),DEVICE_XY(:,2)+board_origin(2) ...
    ,num2str(DEVICE_LABEL),'HorizontalAlignment','center')
title('Panel View')

% concatenate all board fiducial locations together
fid_xy = [sub_fid_x, sub_fid_y];
device_xy =
[DEVICE_XY(:,1)+board_origin(1),DEVICE_XY(:,2)+board_origin(2)];
for i=7:9
    text((fid_xy((i-7)*2+1,1)+fid_xy((i-
7)*2+2,1))/2,fid_xy(i,2),'SIEMENS CT
MM6','HorizontalAlignment','Center',...
    'FontSize',10,'Rotation',0,'color','y')
end
for i=16:18
    text((fid_xy((i-16)*2+1,1)+fid_xy((i-
16)*2+2,1))/2,fid_xy(i,2),'SIEMENS CT
MM6','HorizontalAlignment','Center',...
    'FontSize',10,'Rotation',0,'color','y')
end

%%%%%%%%%%%%%%%%%%%%%%%%%
% Device Draw Function %
%%%%%%%%%%%%%%%%%%%%%%%%%

function figure_handle = DeviceDrawFB250NS(device_origin)

%%%%%%%%%%%%%%%%%%%%%%%%%%%%%%%
% load specimen/machine data %
%%%%%%%%%%%%%%%%%%%%%%%%%%%%%%%

FB250boardNSarray
MachineConfig

%%%%%%%%%%%%%%%%%%%%%%%%%
% Create figure window %
%%%%%%%%%%%%%%%%%%%%%%%%%

set(0,'Units', 'pixels')
position = [550 50 400 400];
figure_handle = figure('Color', [.2 .8 .2], 'Position', position);
      %plot the device outline
[chip_Xdata, chip_Ydata] = PatchUpdate(device_origin, DEVICE_SIZE);
patch('Xdata',chip_Xdata,'Ydata',chip_Ydata,'FaceColor',[.7 .7…
      1],'EdgeColor','none')
daspect([1,1,1])
hold on
axis off
%plot device fiducials
%plot solder joint locations
plot(SOLDER_XY(:,1), SOLDER_XY(:,2),'.','MarkerEdgeColor',[.5 .5 .5],…
      'MarkerFaceColor',[.5 .5 .5],'MarkerSize',48)
```

```
%plot detection points in correct order of scanning
plot(DETECT_XY(:,1), DETECT_XY(:,2), '.r')
detect_pitch = max([abs(DETECT_XY(1,1)-DETECT_XY(2,1)),
abs(DETECT_XY(1,2)-DETECT_XY(2,2))]);
title('Device View')


close all
clear all

%%%%%%%%%%%%%%%%%%%%%%
% load specimen data %
%%%%%%%%%%%%%%%%%%%%%%

FB250boardNSarray       %load board specific data
MachineConfig           %load machine configuration (calibrated data)

%%%%%%%%%%%%%%%%%%%%%%%%%%%%%%%%%%
% Select the Devices to be Tested %
%%%%%%%%%%%%%%%%%%%%%%%%%%%%%%%%%%
Datafile = 'C:\trsfmd_data.txt';
            %define data file name to be outputed
            % Invoke BoardDraw function
[board_figure, fid_xy, device_xy] =
BoardDrawFB250NSarray(BOARD_OFFSET+FIXTURE_HOME);
            % Select the devices to test from user inputs
num_device = input('\nEnter the number of devices to test: ');
fprintf(['\nSelect ' num2str(num_device) ' devices in the figure…
window\n'])
device_select = ginput(num_device);
device_index = FindObject(device_xy, device_select);
for i = 1:length(device_index)
    device_xy_select(i,:) = device_xy(device_index(i),:);
    for j=1:length(DETECT_XY(:,1))
        detect_xy_select(i,j,:) = device_xy_select(i,:)+DETECT_XY(j,:);
    end
end
plot(detect_xy_select(:,:,1),detect_xy_select(:,:,2),'.');
hold on

num_fiducials = input('\nEnter the number of fiducials to measure[2]:…
');          %set default value = 2
if isempty(num_fiducials)
    num_fiducials=2;
end
fprintf(['\nSelect ' num2str(num_fiducials) ' fiducials in the figure…
window\n'])
fid_select = ginput(num_fiducials);
fid_index = FindObject(fid_xy, fid_select);

for i=1:length(fid_index)
    fid_xy_select(i,:) = fid_xy(fid_index(i),:);
end
plot(fid_xy_select(:,1),fid_xy_select(:,2),'+');

      % Calculate the stage movements to measure desired fiducials
```

```
fid_xy_view = fid_xy_select;
      %selected fiducial coordinates in design file
borigin=BOARD_OFFSET+FIXTURE_HOME;
fid_xy_view_tm(:,1)=fid_xy_view(:,1)-borigin(1);
      %return to original coordinates for calculation
fid_xy_view_tm(:,2)=fid_xy_view(:,2)-borigin(2);

fid_xy_view_tm(:,1)=fid_xy_view_tm(:,1)+borigin(1);
fid_xy_view_tm(:,2)=fid_xy_view_tm(:,2)+borigin(2);



fid_steps = round(fid_xy_view_tm/STEPS2MM);
      % Account for direction of motor rotation
fid_steps(:,1) = -fid_steps(:,1);

for i = 1:num_fiducials
    fprintf(['\nMove the stage to Absolute Position ['…
num2str(fid_steps(i,1)) ', ' num2str(fid_steps(i,2)) '].'])
    input_string = input('\nEnter the measured fiducial location in mm…
(x,y): ', 's');
    fid_xy_measured(i,:) = sscanf(input_string, '%f,%f')'
    input_string = input(['\nEnter the actual motor movement in…
mircosteps['num2str(fid_steps(i,1)) ', ' num2str(fid_steps(i,2))
']:'],… 's');
    if isempty(input_string)
        fid_xy_moved(i,:) = fid_steps(i,:);
    else
        fid_xy_moved(i,:) = sscanf(input_string, '%f,%f')';
    end

end

fid_xy_measured(:,1) = -fid_xy_moved(:,1).*STEPS2MM +
fid_xy_measured(:,1);
fid_xy_measured(:,2) = fid_xy_moved(:,2).*STEPS2MM +
fid_xy_measured(:,2);


%%%%%%%%%%%%%%%%%%%%%%%%%%%%%%%%%%%%%%%%%%%%
% Calculate Moves to Device Locations %
%%%%%%%%%%%%%%%%%%%%%%%%%%%%%%%%%%%%%%%%%%%%

TM =RotAngCalc(fid_xy_view(1,:),fid_xy_measured(1,:),fid_xy_view(2,:),…
fid_xy_measured(2,:));

vertices=[0,0;SUBSTRATE_SIZE(1),0;SUBSTRATE_SIZE(1),SUBSTRATE_SIZE(2);…
0,SUBSTRATE_SIZE(2)];

vertices(:,1)=vertices(:,1)+borigin(1);
vertices(:,2)=vertices(:,2)+borigin(2);

for i=1:4
    TEMP=TM*[vertices(i,1),vertices(i,2),1]';
    verticesnew(i,1)=TEMP(1);
    verticesnew(i,2)=TEMP(2);
end
```

```
for i=1:length(device_index)
    TEMP=TM*[device_xy_select(i,1),device_xy_select(i,2),1]';
    device_xy_actual(i,1)=TEMP(1);
    device_xy_actual(i,2)=TEMP(2);
    for j=1:length(DETECT_XY(:,1))
        TEMP2=TM*[detect_xy_select(i,j,1),detect_xy_select(i,j,2),1]';
        TEMP2=TEMP2';
        detect_xy_actual(i,j,1)=TEMP2(1);
        detect_xy_actual(i,j,2)=TEMP2(2);
    end
end
device_steps = round(device_xy_actual/STEPS2MM);
detect_steps = round(detect_xy_actual/STEPS2MM);

% Account for direction of motor rotation
 device_steps(:,1) = -device_steps(:,1);
 detect_steps(:,:,1) = -detect_steps(:,:,1);

% Account for interferometer offset
 device_steps(:,1) = device_steps(:,1)+P_INTER(1);
 device_steps(:,2) = device_steps(:,2)+P_INTER(2);

 detect_steps(:,:,1) = detect_steps(:,:,1)+P_INTER(1);
 detect_steps(:,:,2) = detect_steps(:,:,2)+P_INTER(2);

 laser_xy =[device_xy_actual(:,1)+P_LASER(1),device_xy_actual(:,2)+…
      P_LASER(2)+DEVICE_HEIGHT];
 fileid = fopen(Datafile,'w');
 fprintf(fileid,'Total %d Chips to be Tested:\n',length(device_index));
 fprintf(fileid,'Total %d inspection points per chip:\n',…
       length(DETECT_XY(:,1)));

 for i = 1:size(device_steps,1)
     fprintf(['\nMove the stage to chip ' num2str(device_index(i)) '…
           Absolute Position ['num2str(device_steps(i,1)) ', '…
           num2str(device_steps(i,2)) '].'])
     fprintf(['\nMove the excitation point to [%6.3f %6.3f]'], …
            laser_xy(i,1), laser_xy(i,2))

     fprintf(fileid,'Chip %d data:\n',device_index(i));
     fprintf(fileid,'Centroid:\n');
     fprintf(fileid,'%8d%8d\n',device_steps(i,1),device_steps(i,2));

     fprintf(fileid,['Excitation Point:\n']);
     fprintf(fileid,'%8.3f%8.3f\n',laser_xy(i,1),laser_xy(i,2));

     fprintf(fileid,['Inspection Point:\n']);
     for j=1:length(DETECT_XY(:,1))

fprintf(fileid,'%8d%8d\n',detect_steps(i,j,1),detect_steps(i,j,2));
     end

 end
 fclose(fileid);
 fprintf(['\n Transformed Coordinates have been written to ' Datafile
'\n']);
```

```
 plot(fid_xy_measured(:,1),fid_xy_measured(:,2),'+');
 plot(fid_xy_measured(:,1),fid_xy_measured(:,2),'o');
 plot(device_xy_actual(:,1),device_xy_actual(:,2),'+');
 plot(detect_xy_actual(:,:,1),detect_xy_actual(:,:,2),'.');

patch('Xdata',verticesnew(:,1),'Ydata',verticesnew(:,2),'FaceColor','no
ne','EdgeColor',[.2 .8 .2])

device_figure=DeviceDrawFB250NSarray([0,0]);
```

APPENDIX B

C++ CODE FOR INSPECTION MOTION CONTROL

C++ Code for Inspection Motion Control:

```
//
// Motion Control for FB250
//

#include <iostream.h>
#include <stdio.h>
#include <afxwin.h>
#include <stdlib.h>
#include "C:\my documents\lizheng\fb250motion_array\IDrvKernel.h"

#define MAX_MSG             1024      // maximum number of messages

void main(int argc, char *argv[])
{
    argv = argv;                      // keep the compiler happy
    argc = argc;

    long ActPos = 0;
    unsigned long   GlobErrCode = 0;  // logical OR of all synatx error

    // variables for auto file check.
    FILE *stream;
    char list[2];

    int             inx;      // counter
    int             numCmnds = 0;
                        // number of messages from input file
    CIDrvCmnd       *StrtCmnds[MAX_MSG];
                        //Set register message objects
    CIDrvCmnd       *RegChkCmnds[MAX_MSG];
                        // Check register message commands
    CIDrvCmnd       *TrigStatus[MAX_MSG];
                        //Used to watch for change in trigger button
    int             trigCmnds = 0;
                        //counter for TrigStatus
    int             regCmnds = 0;           //counter for RegChkCmnds
    CIDrvCommChn    *IDrv;
                        //communication channel object
    CString         Axis1("0");             // x-Axis to talk with
    CString         Axis2("1");             // y-Axis to talk with
    CString         CommPort("COM1");       // comm port on PC to use

    CString         Data_X;
                        //define data type (centroid, pad or fiducial)
    CString         Data_Y;
                        //define data type (centroid, pad or fiducial)
    CString         StringDump1;
```

```
                    //define data type (centroid, pad or fiducial)
CString         StringDump2;
               // define data type (centroid, pad or fiducial)
CString         Centroid_X[24];
               // define x-axis centroid absolute motion
CString         Centroid_Y[24];
               // define y-axis centroid absolute motion
CString         Laser_X[24];
               // define x-axis manual stage position
CString         Laser_Y[24];
               // define y-axis manual stage position
CString         Detect_X[24][400];
               // define x-axis inspection point absolute motion
CString         Detect_Y[24][400];
               // define y-axis inspection point absolute motion

CString         DataType1;
CString         DataType2;
CString         X_pos;
               //value for x-axis absolute position motion command
CString         Y_pos;
               //value for y-axis absolute position motion command

CRegSet         *TargVel1;
               // Set Axis1 target velocity message
CRegSet         *Accel1;
               // Set Axis1 acceleration message
CRegSet         *Current1;
               // Set Axis1 current message
CRegSet         *Pos1;
               // Set Axis1 position message

CRegSet         *MovingOutMsk1;
               // Set Axis1 Moving Output Mask
CRegSet         *MovingOutMsk2;
               // Set Axis2 Moving Output Mask
CRegGet         *OutState1;             // get Axis1 Output State
CRegGet         *OutState2;             // get Axis2 Output State
CRegSet         *InpDebncMsk1;
CRegSet         *InpDebncMsk2;
CRegSet         *DebncTime1;
CRegSet         *DebncTime2;
CRegSet         *InpStopMsk1;
CRegSet         *InpStopMsk2;

CRegReset       *ResetCmnd1;            // reset drive message
CRegReset       *ResetCmnd2;            // reset drive message

CRegSet         *TargVel2; // Set Axis1 target velocity message
CRegSet         *Accel2;   // Set Axis1 acceleration message
CRegSet         *Current2; // Set Axis1 current message
CRegSet         *Pos2;     // Set Axis1 position message

CRegGet         *InputState1;   //Axis1 Input State message
CRegGet         *InputState2;   //Axis2 Input State message

CExeSeq         *Execute1[MAX_MSG];
```

```
                                    //execute sequence 1 message


    //Establish Communication with the COM Port
    FILE    *outstream;             // stream for output file
    FILE    *trsfmd_data;           // stream for inspection point file

    int num_chips;
    int num_insp_pts;
    int chip_index[24];


    InputState1 =   new CRegGet(new CString("InpState"), &Axis1);
                                //Input Status Register
    InputState2 =   new CRegGet(new CString("InpState"), &Axis2);
                                //Input Status Register
    OutState1   =   new CRegGet(new CString("OutState"), &Axis1);
                                // Output Status Register axis 1
    OutState2   =   new CRegGet(new CString("OutState"), &Axis2);
                                // Output Status Register axis 2

    if ((outstream = fopen("IDrvCmnd.out", "w")) == NULL)
    {
        return;
    }

    IDrv = new CIDrvCommChn(&CommPort);  // create a comm channel
    if (!(IDrv->OpenSerial()))           // connect to the serial port
    {
        cout << "Failed to connect to serial port: " << CommPort <<"\n";
        fclose(outstream);
        delete IDrv;
        return;
    }

    //output message to the screen to let user know what has happened
    printf("Connected to serial port:  %s \n", CommPort);
    printf("Hit enter to continue and execute home sequence on each
axis. \n");
    getchar(); //wait for a bit

     // After setting up communication, run Home Sequence on each axis

    printf("Homing X axis in progress, please wait...\n");

    IDrv->Transmit(new CExeSeq(new CString("0"), &Axis1));
    for (int n1=0;n1<0x6fff;n1++){
    for (int k1=0;k1<0xffff;k1++){};
    }
    printf("Homing of X axis completed\n");
    printf("Homing Y axis in progress, please wait...\n");

    IDrv->Transmit(new CExeSeq(new CString("0"), &Axis2));
    for (int n2=0;n2<0x71ff;n2++){
    for (int k2=0;k2<0xffff;k2++){};
    }
    printf("Homing of Both Axises Completed.\n\n");
```

```
    numCmnds = 0;
    StrtCmnds[numCmnds++] = TargVel1        = new   CRegSet(new
CString("TargVel"), new CString("167774"),  &Axis1);
            //25599 usteps/s
    StrtCmnds[numCmnds++] = Accel1          = new   CRegSet(new
CString("Accel"),   new CString("640"),     &Axis1);
            //40824 usteps/s/s
    StrtCmnds[numCmnds++] = Current1        = new   CRegSet(new
CString("Current"), new CString("15"),      &Axis1);
            //1.35 amps
    StrtCmnds[numCmnds++] = InpStopMsk1         = new   CRegSet(new
CString("StopInpMsk"),  new CString("0"),       &Axis1);
            //40824 usteps/s/s
    StrtCmnds[numCmnds++] = MovingOutMsk1   = new   CRegSet(new
CString("MovingOutMsk"),    new CString("1"),       &Axis1);
            //MovingOutMsk Axis1 set to 1
    StrtCmnds[numCmnds++] = InpDebncMsk1    = new   CRegSet(new
CString("InpDebncMsk"), new CString("0"),       &Axis1);
            //MovingOutMsk Axis1 set to 1
    StrtCmnds[numCmnds++] = DebncTime1  = new   CRegSet(new
CString("DebncTime"),   new CString("0"),       &Axis1);
            //MovingOutMsk Axis1 set to 1


   StrtCmnds[numCmnds++] = TargVel2        = new   CRegSet(new
CString("TargVel"), new CString("167774"),  &Axis2);//25599 usteps/s
    StrtCmnds[numCmnds++] = Accel2          = new   CRegSet(new
CString("Accel"),   new CString("640"),     &Axis2);//40824 usteps/s/s
    StrtCmnds[numCmnds++] = Current2        = new   CRegSet(new
CString("Current"), new CString("15"),      &Axis2);//1.35amps
    StrtCmnds[numCmnds++] = InpStopMsk2     = new   CRegSet(new
CString("StopInpMsk"),  new CString("0"),   &Axis2);//1.35amps
    StrtCmnds[numCmnds++] = MovingOutMsk2   = new   CRegSet(new
CString("MovingOutMsk"),new CString("1"),   &Axis2);
                //MovingOutMsk Axis2 set to 1
    StrtCmnds[numCmnds++] = InpDebncMsk2    = new   CRegSet(new
CString("InpDebncMsk"), new CString("0"),   &Axis2);
                //MovingOutMsk Axis2 set to 1
    StrtCmnds[numCmnds++] = DebncTime2  = new   CRegSet(new
CString("DebncTime"),   new CString("0"),       &Axis2);
                //MovingOutMsk Axis2 set to 1

    for (inx = 0; inx < numCmnds; ++inx)
     {for (int delay2=0;delay2<3;delay2++)
            IDrv->Transmit(StrtCmnds[inx]);
        for (int delay=0;delay<0xffff;delay++){};
     }


    if( (trsfmd_data  = fopen( "C:\\trsfmd_data.txt", "r" )) == NULL )
      printf( "The file 'trsfmd_data' was not opened\n" );
    else
    { printf( "Coordinate Datafile was successfully opened,\n" );
      fscanf(trsfmd_data,"%s%d%s%s%s%s\n",StringDump1,&num_chips,String
Dump2,StringDump2,StringDump2,StringDump2);
      printf( "There are %d chips to be tested\n",num_chips);
```

```
      fscanf(trsfmd_data,"%s%d%s%s%s%s\n",StringDump1,&num_insp_pts,Str
      ingDump2,StringDump2,StringDump2,StringDump2);
      printf( "There are %d inspection points on each
chip\n",num_insp_pts);

      for(int i=0; i<num_chips; i++)
        {

            fscanf(trsfmd_data,"%s%d%s\n",StringDump1,&chip_index[i],St
            ringDump2);
            printf("\n\n Chip %d is going to be tested
            next\n",chip_index[i]);

            fscanf(trsfmd_data,"%s\n",StringDump1);

            fscanf(trsfmd_data,"%s",Data_X);
                Centroid_X[i]=(LPCTSTR)Data_X;
            fscanf(trsfmd_data,"%s\n",Data_Y);
                Centroid_Y[i]=(LPCTSTR)Data_Y;
            printf("\nThe centroid for chip %d is
            [%s,%s]\n",chip_index[i],Centroid_X[i],Centroid_Y[i]);
            printf("\nStage is about to move...\n");
            printf("\nMake sure manual stage is repositioned at its
            safe position!!\n");
            printf("\nPRESS TRIGGER to move to chip %d: \n",
            chip_index[i]);

            do
                {
                IDrv->Transmit(InputState1);

            }while(InputState1->RegVal()!=0xfff70007);

            for (int delay2=0;delay2<3;delay2++) {
            IDrv->Transmit(new CPrepAbsMove(&Centroid_X[i], &Axis1));
            IDrv->Transmit(new CStartMove(&Axis1));
            IDrv->Transmit(new CPrepAbsMove(&Centroid_Y[i], &Axis2));
            IDrv->Transmit(new CStartMove(&Axis2));
            }


                do
                {
                  for (int delay2=0;delay2<3;delay2++) IDrv-
                  >Transmit(OutState1);
                }while(OutState1->RegVal() & 1);
                  // wait for motor 1 stop

                do
                {
                  for (int delay2=0;delay2<3;delay2++) IDrv-
                  >Transmit(OutState2);
                 }while(OutState2->RegVal() & 1);

                printf("both axis move finished\n");
                printf("Now interferometer is hitting the centroid of
```

```
                chip %d\n",chip_index[i]);

                fscanf(trsfmd_data,"%s%s\n",StringDump1,StringDump2);

                fscanf(trsfmd_data,"%s",Data_X);
                Laser_X[i]=(LPCTSTR)Data_X;
                fscanf(trsfmd_data,"%s\n",Data_Y);
                Laser_Y[i]=(LPCTSTR)Data_Y;
                printf("\nMove manual stage to [%s,%s] to excite chip
                %d, \n",Laser_X[i],Laser_Y[i],chip_index[i]);

            /*initialize ==1*/
               if( (stream = fopen( "C:\\temp\\updatestatus",
               "w+t" )) != NULL )
                {
               list[0] = '1';
               fwrite( list, sizeof( char ), 2, stream );
               printf( "Wrote\n");
               fclose( stream );
                }

            fscanf(trsfmd_data,"%s%s\n",StringDump1,StringDump2);

            for (int j=0;j<num_insp_pts;j++)
            {
                fscanf(trsfmd_data,"%s",Data_X);
                Detect_X[i][j]=(LPCTSTR)Data_X;
                fscanf(trsfmd_data,"%s\n",Data_Y);
                Detect_Y[i][j]=(LPCTSTR)Data_Y;
                printf("inspection point %d of chip %d is
[%s,%s]\n",j+1,chip_index[i],Detect_X[i][j],Detect_Y[i][j]);

                //~~~~~~~~~~~~~~~~~~~~~~~~~~~~~~
                printf("press trigger to move to inspection point %d\n",
j+1);

                do
            {
                if( (stream = fopen( "C:\\temp\\updatestatus",
"r+t" )) != NULL )
                {
                    fread( list, sizeof( char ), 2, stream );
                    fclose( stream );
                }
                else
                printf( "File could not be opened\n" );
            }while(list[0] == '0');


                for (int delay2=0;delay2<3;delay2++){
                IDrv->Transmit(new CPrepAbsMove(&Detect_X[i][j],
                 &Axis1));
                IDrv->Transmit(new CStartMove(&Axis1));
                IDrv->Transmit(new CPrepAbsMove(&Detect_Y[i][j],
                 &Axis2));
                IDrv->Transmit(new CStartMove(&Axis2));
                }
```

```
                do
                {
                    for (int delay2=0;delay2<3;delay2++) IDrv-
                         >Transmit(OutState1);
                    cout<<"Out1="<<OutState1->RegVal()<<endl;
                }while(OutState1->RegVal() & 0x1);
                  //wait for motor 1 stop

                do
                {
                    for (int delay2=0;delay2<3;delay2++) IDrv-
                         >Transmit(OutState2);
                    cout<<"Out2="<<OutState2->RegVal()<<endl;
                }while(OutState2->RegVal() & 0x1);

                printf("both axis move finished\n");
                printf("Now interferometer is hitting the inspection
                        point %d\n",j+1);

                if( (stream = fopen( "C:\\temp\\updatestatus",
                      "w+t" )) != NULL )
                {
               list[0] = '0';
               fwrite( list, sizeof( char ), 2, stream );
               printf( "Wrote\n");
               fclose( stream );
                }
                printf("Aquiring data...when finished, press TRIGGER to
                        move to next point.\n");

            }

        }

        fclose(trsfmd_data);
        printf( "The file 'inspectpts.txt' was closed\n" );
        }

    IDrv->Transmit(new CRegReset(&Axis1));
    IDrv->Transmit(new CRegReset(&Axis2));

    printf("\npress enter to terminate the communication to the
             motor:\n");
    getchar();

    IDrv->CloseSerial();
                  //deletes the object for controlling Serial Port
    fclose(outstream);      //closes the stream to the serial port

            // Destroy the array of messages for checking the registers
            // (Also destroys the VelFdbk1,etc.)
    for (inx = 0; inx < regCmnds; ++inx)
        delete RegChkCmnds[inx];

            // Destroy the array of messages for setting the register
```

```
            //(Includes all the CStrings)
    for (inx = 0; inx < numCmnds; ++inx)
                //Destroy the array of messages for startup
        delete StrtCmnds[inx];
                //Destroy the array of messages for setting the
                // register (Includes all the CStrings)
    for (inx = 0; inx < trigCmnds; ++inx)
            //Destroy the array of messages for checking trigger
        delete TrigStatus[inx];
    delete MovingOutMsk1;
    delete MovingOutMsk2;
    return;
}
```

APPENDIX C

ANSYS APDL SCRIPT FOR FINITE ELEMENT MODEL

ANSYS APDL Script for Finite Element Modal Analysis of FB250 Flip Chip

```
!_____________________________________________________________________!
!Modal Analysis of Siemens FC6.3x6.3 48 bumps peripheral array       !
!_____________________________________________________________________!

     FINISH
     /CLEAR,NOSTART
     /prep7
!units are in mm

!_____________________________________________________________________
     incc = 1e-12              !tiny increment for selecting objects

!define element types
     ET,1,SOLID95              !20 node brick
     ET,2,solid45              !8 node brick
     ET,3,solid92              !10 node tetra
     ET,4,plane2               !6 node triangle
!_____________________________________________________________________
!define material properties
     silicon=1
     fr4=2
     solder=3

!define material property:    SILICON
     MP,EX,1,112.4E9           !silicon young's modulus
     MP,PRXY,1,0.28                  !silicon poisson's ratio
     MP,DENS,1,2329                  !silicon density

!define material property:    FR4
     MP,EX,2,22E9                    !fr4 young's modulus
     MP,PRXY,2,0.20                  !fr4 poisson's ratio
     MP,DENS,2,2000                  !fr4 density

!define material property:    SOLDER(Pb/Sn)
     MP,EX,3,32E9                    !solder young's modulus
     MP,PRXY,3,0.38                  !solder poisson's ratio
     MP,DENS,3,8400                  !solder density

!_____________________________________________________________________
!construct model
!_____________________________________________________________________
!define parameters for geometry
!------------------------------
     bump_r = .095e-3                !bump diameter of 190 microns
     ubm_r = .089e-3                 !UBM diameter of 178 microns
     pitch = .4572e-3                !bump pitch
```

```
fc_thk = .600e-3                !flip chip thickness-600~650mircons
fr4_thk = 0.8e-3                !fr4 board thickness-to be verified
stnd_off = .140e-3              !stand off~bump height
die = 6.35e-3                   !die size, 250milx250mils 6.3mm
fr4 = 4*die

bump_x =-2.5146e-3              !firstbump x location
bump_y =-2.9748e-3              !all bumps y location
bump_z = -0.5*stnd_off          !all bumps z location

bump_x2 =2.9748e-3              !firstbump x location
bump_y2 =-2.5146e-3             !all bumps y location

bump_x3 =2.5146e-3              !firstbump x location
bump_y3 =2.9748e-3              !all bumps y location

bump_x4 =-2.9748e-3             !firstbump x location
bump_y4 =2.5146e-3              !all bumps y location



!Define geometry
!---------------
!first, define the bump
     K,1,bump_x,bump_y,bump_z       !center piont of the first bump
     K,2,bump_x,bump_y,bump_z+0.5*stnd_off      !point above first bump
     K,3,bump_x,bump_y,bump_z-0.5*stnd_off      !point below first bump
     K,4,bump_x+bump_r,bump_y,bump_z

     K,5,bump_x+SQRT(bump_r**2-
            (0.5*stnd_off)**2),bump_y,bump_z+0.5*stnd_off
     K,6,bump_x+SQRT(bump_r**2-(0.5*stnd_off)**2),
            bump_y,bump_z-0.5*stnd_off

     L,2,5
     L,2,3
     L,3,6
     LARC,6,5,4
     AL,1,2,3,4                !generate area
     VROTAT,1,,,,,,2,3         !sweep to get bump shape
     VADD,all                  !four quarters add together
     AADD,2,6,10,14                 !adding areas
     AADD,4,8,12,16
     lsel,s,loc,z,-incc,incc        !select line
     LESIZE,all, , ,3, , , , ,1     !assign a line increments to the
     line segment

     lsel,s,loc,z,-incc-stnd_off,incc-stnd_off
     LESIZE,all, , ,3, , , , ,1     !assign a line increment to the
     lines


     lsel,s,line,,4
     lsel,a,line,,6
     lsel,a,line,,11
     lsel,a,line,,16
     LESIZE,all, , ,5, , , , ,1
```

```
                    !assign line division size to ctrl element number


!finished single column here
!----------------------------
     NUMCMP,volu
     VGEN,12,all,,,pitch                    !copy to form 12 columns
     vsel,s,volu,,1
     VGEN,2,all,,,bump_x2-bump_x,bump_y2-bump_y
     VSEL,s,volu,,13
     VGEN,12,all,,,,pitch
     vsel,s,volu,,1
     VGEN,2,all,,,bump_x3-bump_x,bump_y3-bump_y
     VSEL,s,volu,,25
     VGEN,12,all,,,-pitch
     vsel,s,volu,,1
     VGEN,2,all,,,bump_x4-bump_x,bump_y4-bump_y
     VSEL,s,volu,,37
     VGEN,12,all,,,,-pitch
     vdele,all,,,1
     vsel,all
     cm,bumps,volu                          !name bumps
!_____________________________
     asel,s,loc,z,-incc,incc
     aatt,3,,4
     amesh,all
     asel,all                  !area mesh the top surface of 14 bumps
     w/h PLANE2

!---------------------
     blc5,0,0,die,die,fc_thk
     blc5,0,0,bump_x3-bump_x,bump_y4-bump_y2,fc_thk
     vovlap,49,50
     numcmp,volu
     blc5,0,0,die,die,fr4_thk
     blc5,0,0,bump_x3-bump_x,bump_y4-bump_y2,fr4_thk
     blc5,0,0,fr4,fr4,fr4_thk
     vsel,s,volu,,51,53
     vgen,2,all,,,,,-stnd_off-fr4_thk,,,1
     numcmp,volu
     vovlap,51,52,53
     numcmp,volu
     vsel,s,volu,,1,48
     vsel,a,volu,,50
     vsel,a,volu,,52
     vglue,all
     numcmp,volu

     VSEL,s,volu,,1,48
     cm,matbumps,volu
     VATT,3,,2                 !material: solder-3, etype: solid45
     vsweep,all                !mesh all bumps with SOLID45
     aclear,all                !clear the PLANE2 area mesh.


     lsel,s,line,,589,596
     lsel,a,line,,613,620
```

```
     lsel,a,line,,625,632
     lsel,a,line,,601,608
     lsel,a,line,,577,584
     lesize,all,,,10,,,,,1
                  !define line division to ctrl elem numbers.
     lsel,s,line,,597,600
     lsel,a,line,,621,624
     lsel,a,line,,609,612
     lsel,a,line,,633,636
     lsel,a,line,,585,588
     lesize,all,,,3,,,,,1

     VSEL,s,volu,,49
     vsel,a,volu,,52
     cm,matchips,volu
     vatt,1,,3
     vmesh,all                !mesh the underfill with SOLID92

     VSEL,s,volu,,50
     vsel,a,volu,,51
     vsel,a,volu,,53
     cm,matfr4,volu
     vatt,2,,3
     vmesh,all

     vclear,all
     vdele,all

     vsel,all

     NUMCMP,elem

     /color,cm,gree,matfr4          !green color for pcb
     /TRLCY,cm,0.5,matfr4

     /color,cm,red,matbumps         !red for bumps
     /color,cm,cblu,matchips        !cyan blue for chip
     /TRLCY,cm,0.5,matchips
                  !make package transparent to let bumps visible.

     NSEL,s,loc,z,-incc-stnd_off,incc-stnd_off
                  !select the center axis
     D,all,all
     NSEL,all

     FINISH
!_____________________________________________________________________

/SOLU
     ANTYPE,MODAL          ! Choose modal analysis type
     MODOPT,LANB,40        ! Choose Block Lanczos mode extraction
     method,
                               ! extracting 40 modes
     MXPAND,40
     /output,try,txt
     SOLVE
     /out
```

```
     *dim,fary,array,40
     *dim,pary,array,40
     *dim,mnbr,array,40
     *do,moden,1,40,1
      mnbr(moden)=moden
      *get,fary(moden),MODE,moden,FREQ
      *get,pary(moden),MODE,moden,PFACT
     *enddo
     /output,Dorst,txt
     MPLIST,1,3
     /com,~~~~~~~~~~~~~~~ ~~~~~~~~~~~~~~~~~~~~~~~~~~~~~~~~~~~~~~~~~~~~~~~~~~~
     /com,mode     mode frequency      participation factor
     /com,____     _____________       ____________________
     *vwrite,mnbr(1),fary(1),pary(1)
     %3I     %13e     %16e
     /out

     FINISH
/SOLU
     ANTYPE,SPECTR
     SPOPT,SPRS,40,YES
     SED,,,1
     SVTYP,3
     FREQ,.1,800
     SV,,.44,.44
     SOLVE
     FINISH
/SOLU
     ANTYPE,MODAL
     EXPASS,ON
     MXPAND,40,,,YES,0.005
     SOLVE
     FINISH
```

BIBLIOGRAPHY

Automotive Industry Action Group (AIAG) (1993), Measurement System Analysis, 3rd Edition.

Barrentine, Larry, Concepts for R&R Studies, ASQ Quality Press, 1991

Blevins, R. D., Formulas for Natural Frequency and Mode Shape, Krieger, 1995

Blish, R. et al., "Critical Challenges for the International Technology Roadmap (ITRS)", *International SEMATECH white paper*, Rev. 3, 2003.

Capson, David and Eng Sai-Kit; "A tiered-color illumination approach for machine inspection of solder joints", *IEEE trans. On pattern analysis and machine intelligence*, Vol. 10, No.3, May 1988, pp. 387-393

Cielo, P., Nadeau, F. and Lamontagne, M., "Laser generation of convergent acoustic waves for materials inspection", *Ultrasonics*, March, 1985, pp. 55-62

Davies, S. J., Edwards, C., Taylor, G. S. and Palmer, S. B., (1993) "Laser-generated ultrasound: its properties, mechanisms and multifarious applications". *Applied Physics,* Vol. 26, pp. 329 – 348

Dewhurst, R. J. and Shan, Q., (1999) "Optical remote measurement of ultrasound", *Measurement Science and Technology*, Vol. 10, 1999, pp. R139-R168

Dias, R., Goruganthu, R., Goyal, D., Hartfield, C., Hunt, D., McClelland D., Cargo, J., Samuelson, G., Stierman, R., Assembly Analytical Forum Analytical Tool Roadmap White Paper, International SEMATECH, 2004

Dixon, S., Edwards, C. and Palmer, S. B. (1996), "Generation of ultrasound by an expanding plasma", *Journal of Physics D: Applied Physics*, Vol. 29, 1996, pp. 3039-3044

Ewins, D. J., (2000) Modal Testing – Theory, Practice and Application, 2nd Ed. Research Studies Press Ltd.

Ginsberg, Jerry H., (2001) Mechanical and Structural Vibrations: Theory and Applications, John Wiley & Sons, Inc, New York.

Gorman, D. J., (1982) Free Vibration Analysis of Rectangular Plates, Elsevier North Holland, 1982.

Goyal, D., (2000) "X-ray Tomography for Electronic Packages," Proceedings of the 26th International Symposium for Testing and Failure Analysis, 2000, pp. 49

Hane, Kazuhiro and Hattori, Shuzo, (1988) "Photothermoelastic inspection of soldered connections", *Applied Optics*, Volume 27, Issue 19, October 1, 1988, pp.3965-3967

Hayter, A. J., (2002) Probability and Statistics for Engineers and Scientists, 2nd ed., Duxbury Press, pp 657-662.

Howard, T., Erdahl, D., Ume, C., and Galmaski, J., (2002) "Development of an Advanced System for Inspection of Flip Chip and Chip Scale Packaging Interconnects using Laser Ultrasound and Interferometric Techniques", *The International Journal of Microcircuits & Electronic Packaging*, Vol. 25, No. 1, pp.1-14, 2002.

Howard, Turner, "Design of an Advanced System for Inspection of Microelectronic Devices and Their Solder Connections Using Laser-Induced Vibration Techniques", M.S. thesis, Georgia Institute of Technology, 2002

Hutchins, D. A., (1988) "Ultrasonic Generation by Pulsed Lasers", *Physical Acoustics,* Vol. XVIII, 1988, pp. 21-123

JEDEC Standard Test Method A104-B: Temperature Cycling, JEDEC Solid State Technology Association, Arlington, Virginia, July, 2000.

Jing, Hong et al, (1986) "Laser holographic inspection of solder joints on printed circuit board", *Proc. SPIE International Society of Optical Engineers*, Vol. 673, July 1986, pp. 167-169

Khazan, Alexander (1994) Transducers and Their Elements: Design and Application, Prentice Hall, 1994

Keely, C. A., (1989); "Solder joint inspection using laser Doppler vibrometry", *Hewlett-Packard Journal*, October 1989, pp. 81-85

Lau, John and Keely, Catherine, (1989) "Dynamic Characterization of Surface-Mount Component Leads for Solder Joint Inspection", *IEEE Transactions on Components, Hybrids, and Manufacturing Technology*, Vol. 12, No. 4, Dec. 1989, pp. 594-602

Liu, Sheng, Erdahl, Dathan and Ume, I. Charles, (2001) "A Novel Approach for Flip Chip Solder Joint Quality Inspection: Laser Ultrasound and Interferometric System", *IEEE Transactions on Components and Packaging Technologies*, Vol. 24, No. 4, Dec. 2001, pp. 616-624

Liu, Sheng and Ume, I. Charles, (2003) "Digital Signal Processing in a Novel Flip Chip Solder Joint Defects Inspection System", *ASME Journal of Electronic Packaging*, Vol. 125, No. 1, Mar. 2003, pp. 39-43

Liu, Sheng, "System Implementation, Modeling and Defects Pattern Recognition for Flip Chip Solder Joint Inspection Using Laser Techniques", Ph.D. dissertation, Georgia Institute of Technology, 2001

Manolakis, Dimitris, Ingle, Vinay and Kogon, Stephen, (2000), Statistical and Adaptive Signal Processing: Spectral Estimation, Signal Modeling, Adaptive Filtering and Array Processing, International Editions 2000, pp. 195-255

Mark, Richardson, (2005) "Modal Analysis Versus Finite-Element Analysis", *Sound and Vibration*, Sep. 2005

Martin, Perry, (1999) Electronic Failure Analysis Handbook, McGraw-Hill (1999), pp. 13.26-13.28

Monchalin, J. P., (1986a) "Laser ultrasonic generation and optical detection a confocal Fabry-Perot interferometer", *Materials Evaluation*, Vol. 44, September 1986, pp. 1231-1237

Monchalin, J. P., (1986b) "Optical Detection of Ultrasound", *IEEE Transactions on Ultrasonics, Ferroelectrics, and Frequency Control*, Vol. UFFC-33, No. 5, September 1986. pp. 485-499

Monchalin, J. P., Aussel1, J. D., Héon, R., Jen, C. K., Boudreault, A. and Bernier, R., (1989) "Measurement of In-Plane and Out-of-Plane Ultrasonic Displacements by Optical Heterodyne Interferometry", *Journal of Nondestructive Evaluation*, Vol. 8, No. 2. 1989, pp. 121-133

Montgomery, D. C. & Runger, G. C. (1993-1), "Gauge Capability and Designed Experiments. Part I: Basic Methods", *Quality Engineering*, 6(1), pp. 115-135

Montgomery, D. C. & Runger, G. C. (1993-2), "Gauge Capability and Designed Experiments. Part II: Experimental Design Models and Variance Component Estimation", *Quality Engineering*, 6(2), pp. 289-305

Nakagawa, Y., Hara, Y., and Hashimoto, M., (1985) "Automatic visual inspection using digital image processing", *Hitachi Rev.*, vol. 34, no. 1, 1985, pp. 55-60

O'Conchuir, D., McCurdy, J. and Casey, V., "Survey of non-destructive inspection methods for solder joint integrity", *Proceedings of IEEE 1991 National Aerospace and Electronics Conference*, Dayton, OH, 1991, pp. 1268-1275.

Pierce, S. G., Culshaw, B., and Shan, Q., "Laser generation of ultrasound using a modulated continuous wave laser diode" *Applied Physics Letters*, Vol. 72, No. 9, March 1998, pp. 1030-1032

Philp, W. R., Podlesak, M. and Pierce, S. G., "Acoustic and Flexural Excitation of a Floating Structure by a Single Laser Pulse," *Applied Optics* 35, no. 36 (1996): pp. 7051.

Scruby, C. B. and Drain, L. E., (1990) Laser Ultrasonics: Techniques and Applications. Adam Hilger, Bristol.

Seto, W.W., (1971) Acoustics, Mcgraw-Hill, 1971

Shen, Zhonghua, Xu, Baiqiang, Ni, Xiaowu and Lu, Jian, "Numerical Simulation of Laser-Generated Ultrasonic Waves in Layered Plates", *Journal of Physics D: Applied Physics*, Vol. 37, 2004, pp. 2364-2370

Schuster, Arthur, *Terrestrial Magnetism* Vol. 3, 24, 1898.

Slepian, D., "Prolate spherodial wave functions, fourier analysis, and uncertainty - v: The discrete case", *The Bell System Technical Journal*, 57(5), pp. 1371–1430, 1978

Sorazu, B., Thursby, G., Culshaw, B., Dong, F., Pierce, S. G., Yang, Y. and Betz, D., (2003) "Optical Generation and Detection of Ultraround", *Strain*, Vol. 39, 2003, pp 111-114

Thomson, D. J., (1982), "Spectrum estimation and harmonic analysis", *Proc. IEEE*, Vol. 70, No. 9, pp.1055–1096, 1982

Thomson, D. J., (1989) "Multi-window bispectrum estimates", *Proc. IEEE Workshop on Higher-Order Statistics*, Vail, Colorado, pp. 19–23, 1989

Timoshenko, S. and Woinwsky-Krieger, S., Theory of Plates and Shells, McGraw-Hill Book Co., New York, 1959.

Traub, A. C., (1988) "Parts inspection by laser beam heat injection", *NDT International*, Vol. 21, No. 2, April 1988, pp. 63-69

Tsai, P., (1988), "Variable Gauge Repeatability and Reproducibility Study Using the Analysis of Variance Method", *Quality Engineering*, 1(1), pp. 107-115

Wu, Lei, Cheng, Jian-chun and Zhang, Shu-yi, "Mechanisms of Laser-Generated Ultrasound in Plates," *Journal of Physics, D, Applied Physics* 28 (1995): pp. 958

Welch, P.D., "The Use of Fast Fourier Transform for the Estimation of Power Spectra: A Method Based on Time Averaging Over Short, Modified Periodograms", *IEEE Transactions on Audio and Electroacoustics*, Vol. AU-15, Jun. 1967, pp. 70-73

Yang, J. and Ume, C., (1994) "Performance Evaluation of Fiber Array for NDE Application", *Research in Nondestructive Evaluation*, Vol. 5, No. 3, 1994

Zhang, L., Ume, C., Gamalski, J. and Galuschki, K., "Detection of Flip Chip Solder Joint Cracks Using Correlation Coefficient Analysis of Laser Ultrasound Signals," in *IEEE Transactions on Components and Packaing Technologies*, in press, 2005

Zhou, Shiwei, Reynolds, Paul, Krause, Roland, Buma, Takashi, O'Donnell, Matthew and Hossack, John, "Finite-Element Analysis of Material and Parameter Effects in Laser-Based Thermoelastic Ultrasound Generation", *IEEE Transactions on Ultrasonics, Ferroelectrics, and Frequency Control*, Vol. 51, No. 9, September, 2004, pp. 1178-1186